IntechOpen

High Temperature Corrosion

Edited by Zaki Ahmad

HIGH TEMPERATURE CORROSION

Edited by **Zaki Ahmad**

High Temperature Corrosion
http://dx.doi.org/10.5772/61546
Edited by Zaki Ahmad

Contributors

Tomasz Dudziak, Arivazhagan Natarajan, Arivarasu M, Gokulkumar K, Devendranath Ramkumar K, Joanna Małecka, Aleksey Nikiforov, Mahmood Aliofkhazraei, Sneha Samal, Zaki Ahmad

© The Editor(s) and the Author(s) 2016
The moral rights of the and the author(s) have been asserted.
All rights to the book as a whole are reserved by INTECH. The book as a whole (compilation) cannot be reproduced, distributed or used for commercial or non-commercial purposes without INTECH's written permission.
Enquiries concerning the use of the book should be directed to INTECH rights and permissions department (permissions@intechopen.com).
Violations are liable to prosecution under the governing Copyright Law.

Individual chapters of this publication are distributed under the terms of the Creative Commons Attribution 3.0 Unported License which permits commercial use, distribution and reproduction of the individual chapters, provided the original author(s) and source publication are appropriately acknowledged. If so indicated, certain images may not be included under the Creative Commons license. In such cases users will need to obtain permission from the license holder to reproduce the material. More details and guidelines concerning content reuse and adaptation can be foundat http://www.intechopen.com/copyright-policy.html.

Notice

Statements and opinions expressed in the chapters are these of the individual contributors and not necessarily those of the editors or publisher. No responsibility is accepted for the accuracy of information contained in the published chapters. The publisher assumes no responsibility for any damage or injury to persons or property arising out of the use of any materials, instructions, methods or ideas contained in the book.

First published in Croatia, 2016 by INTECH d.o.o.
eBook (PDF) Published by IN TECH d.o.o.
Place and year of publication of eBook (PDF): Rijeka, 2019.
IntechOpen is the global imprint of IN TECH d.o.o.
Printed in Croatia

Legal deposit, Croatia: National and University Library in Zagreb

Additional hard and PDF copies can be obtained from orders@intechopen.com

High Temperature Corrosion
Edited by Zaki Ahmad

p. cm.

Print ISBN 978-953-51-2507-5

Online ISBN 978-953-51-2508-2

eBook (PDF) ISBN 978-953-51-6673-3

Meet the editor

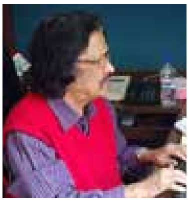

Dr. Zaki Ahmad is a Professor Emeritus of King Fahd University of Petroleum and Minerals, Saudi Arabia, and an adjunct professor at COMSATS Institute of Information Technology, Lahore. He is the fellow of IOM3, UK, and a chartered engineer of the UK Engineering Council. He is a member of the European Federation of Corrosion. He is the recipient of best researcher award by Energy Exchange in 2011. He is the author and editor of six books including the popular text book entitled *Principles of Corrosion Engineering and Corrosion Control* published by Elsevier at international level and over 150 research papers. His projects in nanotechnology, green engineering, and harvesting water from air incorporate human values.

Contents

Preface

I dedicate this chapter to my beloved wife Shams-u-Jehan Begum and my beloved son Intekhab Ahmad whose premature death left me alone in this material world, but their loving spirit inspired me to continue my research work.

It is a common observation that all metal alloys and other materials corrode in harsh environments and oxidize at high temperatures. High-temperature corrosion has unique importance because it affects the equipments and components in aerospace, power generation, metal processing, automotive, and chemical process industry. It assumes special significance in oil and gas industry. The liquid phases, molten metals, and molten salts present crucial challenges to suppress high-temperature corrosion. If high-temperature corrosion could be controlled, millions of dollars and precious resources could be saved. This book is an attempt to introduce readers to the recent developments in corrosion.

Chapter 1 "Introduction to High-Temperature Coatings" introduces readers with the fundamentals of high-temperature coating and the different techniques used. Chapter 2 describes the steam oxidation of several Fe-based materials and shows how these materials can be utilized to minimize high-temperature corrosion. The hot corrosion of weldments is extremely important for the industry. Colossal damage can be done by selection of improper welding techniques and materials for weldments. Efforts are needed to select processes that reduce heat input and appropriate matching composition of filler metal. Appropriate welding materials need to be selected to reduce dendritic and interdendritic segregation and intergranular corrosion. Chapter 3 describes the techniques to lower the risks of damage by weldments. Chapter 4 describes the corrosion oxidation behavior of orthorhombic Ti2AlNb alloy. The coated samples of the alloy showed reduced mass gain compared to uncoated alloy. There is potential for developing such alloys with intermetallic phases and understanding their mechanism. In Chapter 5, there is a huge demand for inexpensive high-temperature alloys. The electrochemical corrosion behavior of stainless steels, high-nickel alloys, tantalum, nickel, titanium, tungsten, molybdenum, and niobium is covered. However, these materials are highly expensive, and efforts need to be made to explore alternate materials. Electrochemical studies are good techniques as shown in chapter ".Electrochemical Studies of Corrosion in Liquid Electrolytes for Energy Conversion Applications at Elevated Temperatures". The role of crystal structure and grain size on the mechanism of high-temperature corrosion is highly important. The combined effect of both needs to be thoroughly understood. The correlation between the two has been well illustrated through a mechanistic approach utilizing SEM, XRD, and other state-of-the-art equipment.

Recent years have witnessed the growth of thermal-sprayed coatings for high-temperature applications and harsh environments such as petroleum, chemical, and pulp and paper industry. as Although sufficient work has been done on APS-sprayed and HVOF-sprayed coatings, very little work has been done on their corrosion resistance in aggressive environments. The chapter on "Mechanism of Corrosion and Erosion Resistance of Plasma-Sprayed Nanostructured Coatings" comprehensively describes the corrosion behavior of plasma-sprayed coatings. I hope that the contents of the book will not only benefit the graduate students but it would also benefit the industry.

I heartily appreciate the assistance provided to me by Mr. Tahir Saif and Ms. Naila Riaz in the various phases of editing the book. I thank the Head of Chemical Engineering Department, COMSATS, Lahore, Pakistan, Prof. Dr. Asad Ullah Khan for supporting and encouraging me. I am grateful to Prof. Dr. Robina Farooq for her inspiration and cooperation. I can never forget KFUPM, Dhahran, Saudi Arabia, where I spent great part of my life and picked up a very good experience, which enables me to keep going in the research and editorial work. I cannot forget the support given by my late wife Shams-u-Jehan Begum and my late son Intekhab Ahmad. I appreciate the support of Dr. Intesar Ahmad, HOD, Electrical Engineering Department, Lahore College for Women University, Lahore, Pakistan, and Mr. Manzar Ahmad, assistant prof. at the University of South Asia, Lahore, Pakistan.

Dr. Zaki Ahmad
COMSATS Institute of Information Technology,
Lahore, Pakistan

Note from the publisher

It is with great sadness and regret that we inform the contributing authors and future readers of this book that the Editor, Prof. Zaki Ahmad, passed away shortly after finishing the book and before having a chance to see its publication.

Prof. Ahmad was InTech's long term collaborator and edited his first book with us in 2011 ("Recent Trends in Processing and Degradation of Aluminium Alloys"). The book "High Temperature Corrosion" was his fourth edited volume. The fruitful collaboration continued until his final days when he was acting as a co-editor on a book "Wastewater Treatment and Resource Recovery".

We would like to acknowledge Dr. Zaki Ahmad's contribution to open access scientific publishing, which he made during 6 years of dedicated work on edited volumes and express our gratitude for his pleasant cooperation with us.

InTech Book Department Team

August, 2016

Chapter 1

Introduction to High-Temperature Coatings

Masoud Shourgeshty, Mahmood Aliofkhazraei and
Mehrdad Mohammad Alipour

Additional information is available at the end of the chapter

http://dx.doi.org/10.5772/64282

Abstract

Coatings for turbine blades possess some attractive properties like oxidation and hot corrosion resistance, maintain their strength, cohesion and etc. High temperature damages divide in three general groups: High temperature corrosion type II (600–850°C), High temperature corrosion type I (750–950°C), Oxidation (950°C and higher). There are three types of high temperature coating: 1- Diffusional coating, 2- Overlay coating, 3- Thermal Barrier coating (TBC). The third type, considered as the overlay coating widely used for critical high temperature conditions like, combustion chamber, rotating blades, etc. The advantages of TBC are: increasing the life time of part, improving the engine efficiency (by increasing TIT (Turbine Inlet Temperature)), decreasing the coolant air flow. TBC coating system contains 4 layer that they totally differs from each other. Four principal segments of TBC layers are: 1- super alloy substrate, 2- aluminum intermediate coating, 3- TGO (Thermally Grown Oxide), 4- ceramic final coating. Some advantages of thermal sprayed coatings are: 1- making thick coating with high velocity, 2- low cost recoating damaged regions, 3- covering a wide variety of materials that can be melt without decomposition, 4- mechanically joint coating particles to the substrate, 5- applicable either manually or automatically.

Keywords: oxidation, coatings, hot corrosion, HVOF, MCrAlY

1. Introduction

1.1. History

Sixty years after the invention of jet engines, flying has become a conventional method of transportation. In the early 1940s, many people were considered jet-powered flight as no more than a “laboratory experiment.” In fact, these doubts were not unfounded because the materials used in parts of the engine could not survive more than a few hundred hours at then relatively modest temperatures. At the end of the 1960s, commercial jets were invented, and the commercial aviation market overtook the military one by the end of the 1980s.

Nowadays, economic and environmental issues have been considered to be incentives for operation of engines at higher temperatures due to improved thermodynamic efficiency and reduced emissions of the pollutants. In its early years, the quest for higher temperatures was dominated by materials and process developments. The apparition of superalloys in the early 1950s, considerable amelioration in casting technologies, and in the 1960s, the cooling system for turbine blades were all major steps forward. Over the past 20–30 years, alloy improvement, directional and single-crystal solidification have contributed significantly, but, arguably, the emphasis has shifted to coating systems which have allowed an increase in gas temperature up to 1100°C.

Coatings in gas turbines serve several purposes, whether in jet engines, land-based power generation turbines, or marine engines. The first requirement to operate turbines at higher temperatures is improved strength. On the other hand, these conditions also mean severe oxidation/corrosion problems. The negative point of this case is that the improvement in mechanical properties of the base alloys was made at the expense of environmental resistance.

Therefore, the first purpose of coatings was to palliate for the poor oxidation resistance of the base alloy (aluminide, Pt-aluminide, and MCrAlY). The second type of coatings applied to high-temperature parts are known as thermal barrier coatings (TBCs) which are ceramic coatings with very low thermal conductivity. Despite being thin, they allow for a drop of 100–300°C between the gas and metal surface temperatures. However, such coatings are oxygen transparent and do not prevent oxidation of the underlying substrate [1].

2. Hot corrosion and oxidation degradation processes

Depending on the temperature, three accelerated degradation processes occur which can be divided into three categories according to increase in temperature: type II hot corrosion, type I hot corrosion, and oxidation (see **Figure 1**).

1. Hot corrosion type II: this type of hot corrosion occurs between 600 and 850ºC. This phenomenon forms sulfates from the substrate at a certain partial pressure for sublimation of sulfur trioxide. The sulfate reaction with alkali metal forms low-melting-point particles that prevent from forming a protective layer.

2. Hot corrosion type I: this type includes the transportation of sulfur from a deposit (sulfate base like Na_2SO_4) through oxide layer into metal substrate with formation of stable oxides. After reaction between a stable sulfide, like Cr, and a moving sulfur through a scale, the base metal sulfides form a disastrous sequence at molten phase because this type of hot corrosion seems to occur at 750–950ºC. Thus, the formation of NiS_2 (molten at 645°C) and Co_xS_y (lowest liquids at 840°C) can lead to serious component degradation. The most suitable materials which can resist type I hot corrosion are $PtAl_2$-(Ni-Pt-Al) coatings

(aluminide coatings modified with platinum) and MCrAlY coatings containing up to 25 wt% Cr and 6 wt% Al.

3. Oxidation: this material loss occurs at 950°C and higher temperature. The rate of oxidation depends on the transportation of cations or anions through the structure of oxide layer and grain boundary. The dissociation pressure of oxide determines the most stable oxide in a set of elements which is lowest for Al and Cr in comparison with Fe, Co, and Ni. If the Cr content of Ni-Cr alloy is more than 10%, a continuous and protective layer (chromia) will form. For cobalt base superalloys to form a continuous oxide layer, Cr content should be at least 25% because of different diffusion behaviors of Cr in Co alloys. To increase the oxidation resistance of chromia at a temperature above 850°C (because it sublimates and becomes volatile oxide "CrO_3"), the addition of aluminum is preferred, especially for severe and critical conditions like gas turbine blades. There is another advantage of addition of aluminum which is shown schematically in **Figure 2**. It shows the slower rate of formation of alumina than chromia at a same temperature. Because of the higher activity of Cr than Al (which causes the oxygen enrichment by Cr rather than Al), the formation of alumina will be reduced in lower Al activity in Cr-Al mixture.

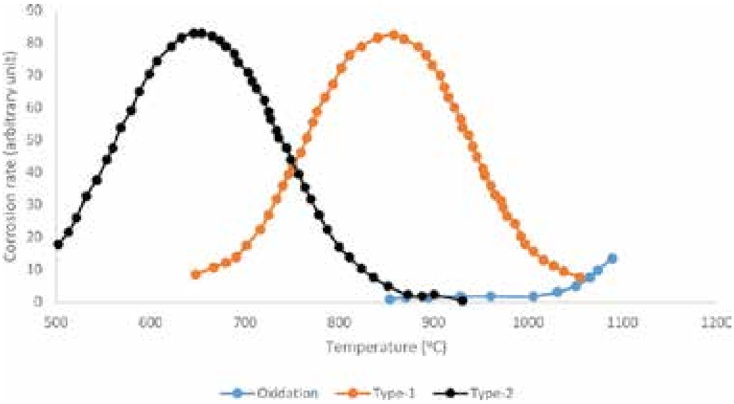

Figure 1. The temperature range for hot corrosion type II, hot corrosion type I, and oxidation.

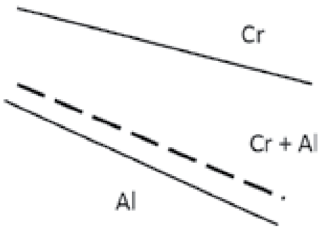

Figure 2. Schematic diagram for the oxidation of the alloy containing Cr, Cr + Al, and Al.

The aluminum and chromium contents referred to above apply to isothermal oxidation conditions. When thermal cycling conditions prevail, oxide scales can spall from the substrate surface due to thermally induced stresses. Under such conditions, the oxidation resistance can be markedly improved by the addition of reactive elements (Y, Hf, and Ce) to alloys and coatings. Researchers have shown that yttrium and rare earth metals segregate to grain boundaries within alumina scales causing a reduction in Al and O transport rates through the oxide and thus reduce oxidation rates. On the other hand, reactive elements combine with sulfur and phosphorus impurities in metallic materials and coatings. Thus, these impurities cannot selectively diffuse to the surface and contaminate the oxide-metallic interface. Therefore, this leads to extremely good adherence of the oxide shell.

Generally, overlay coatings containing 18–22% Cr and 8–12% Al, NiCrAlY's, and NiCoCrAlY's systems perform better under oxidizing conditions (above 900°C) [2] (see **Figure 3**).

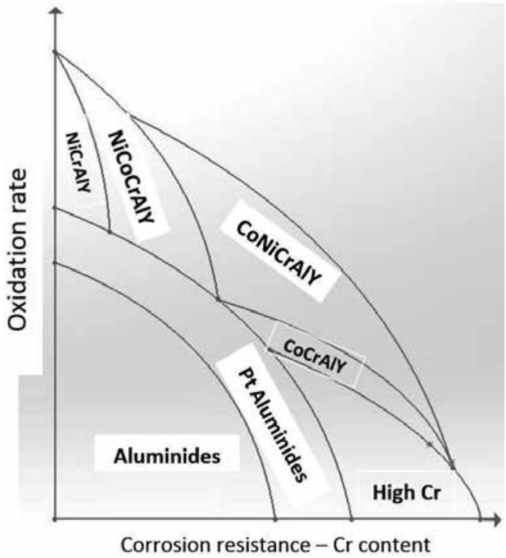

Figure 3. Relative resistance of coating systems against high-temperature oxidation and corrosion.

2.1. Oxidation

When a metal is exposed to oxygen, the reaction occurs when the oxygen pressure is higher than the pressure needed to balance the metal-metal oxide.

$$M + \frac{1}{2}O_2 = MO \tag{1}$$

The values for the oxygen equilibrium pressure are very low at very low temperatures for most metals except precious metals; therefore, in many gas environments, the thermodynamic conditions are favorable for oxide formation. Thus, the oxide shells expand on metals that are exposed to oxygen at high temperatures. When the shells are dense and protective, the oxidation speed is expressed by the following formula according to the weight changes of the sample:

$$\frac{d\left(\frac{\Delta m}{A}\right)}{dt} = \frac{k_p}{\frac{\Delta m}{A}} \tag{2}$$

Δm, A, t, and K_p are indicative of weight change, sample area, time, and parabolic rate constant, respectively. An important feature of this relation is that the rate of oxidation declines with time because the oxide shell (like a barrier) prevents oxidation by separating the reactive gases. If the oxide shell is not protective, it cannot prevent the progress of oxidation and the oxidative rate is expressed by the following formula:

$$\frac{d\left(\frac{\Delta m}{A}\right)}{dt} = K_l \tag{3}$$

K_l is a constant quantity. Oxidation of metals obeys other velocity rules in addition to parabolic (Eq. (2)) and linear (Eq. (3)) laws; however, considering the issue of resistance to oxidation, these two laws are adequate.

As the alloy is exposed to oxygen, oxides of all elements in the alloy will be formed if the oxygen pressure in the gas is higher than the determined equilibrium pressure for each element. Nevertheless, numerous oxide phases usually form during the early stages of the oxidation of alloy. The thermodynamic conditions for oxide formation are controlled by the activity of metallic elements in the alloy, oxygen pressure in the gas, and the tendency of relative affinity of metallic elements for oxygen. As a result of this competition between alloying elements in combination with oxygen, there is a tendency that the alloy is covered with the thermodynamically most stable oxide. These conditions lead to a specific result called selective oxidation of an element in the alloy. The shells formed on the alloy often contain layers with several thermodynamically stable oxides. Oxidation of alloys often has a transient stage in which different oxides form. Then, the process continues with another step in which only the thermodynamically stable phases grow. Kinetic factors play an important role in determining those oxide phases which are able to grow. During the very early stages of oxidation, all thermodynamically stable oxides are formed. By continuing the oxidation process, diffusion phenomena as well as displacement reactions begin, the important part of which is the diffusion of oxygen into the alloy and outward diffusion of elements in the alloy. During the condition that oxygen penetrates faster than metallic elements, the volume fraction of oxide is approximately equal to the volume fraction of the element in the alloy because the element converts to oxide in its place and without any penetration. On the other hand, when the oxygen penetration is slow compared to elements in the alloy, the volume fraction of the oxide can be more than that of the element in the alloy because that element penetrates from the inner areas to the oxidation front. When the volume fraction of the considered oxide reaches a critical value, it is desirable to form a higher oxide in accordance with the lateral growth and expand in the form of a continuous layer on the surface of alloy. In short, expansion of oxides on alloys can be described as a continuous process.

Growth and expansion of the oxide shell related to formation of oxide shells on Ni-Cr-Al alloys is schematically shown in **Figure 4**. In this example, it is assumed that the oxygen pressure is high enough to form all possible oxide phases. In the very early stages of the oxidation process, rapid absorption of oxygen occurs by alloy, and NiO, Cr_2O_3, and α-Al_2O_3 oxides form on the surface of the alloy equal to the spinel phases (in other words, $NiCrAl_2O_4$ and $NiAl_2O_4$). The relative proportions of these phases are determined by the primary composition of the alloy. By continuing the oxidation process, diffusion processes exercise their influences. The nature of these effects depends on the concentration of elements in the alloy and the penetration parameters. Generally, when the concentrations of chromium and aluminum are low, none of the continuous layers of Cr_2O_3 or Al_2O_3 spread, but a dominant continuous shell of NiO can be formed on the subscale area of Cr_2O_3 or Al_2O_3 particles. It is important to emphasize that the duration of the transient oxidation stage, in which selective oxidation process occurs, varies considerably from one alloy to another.

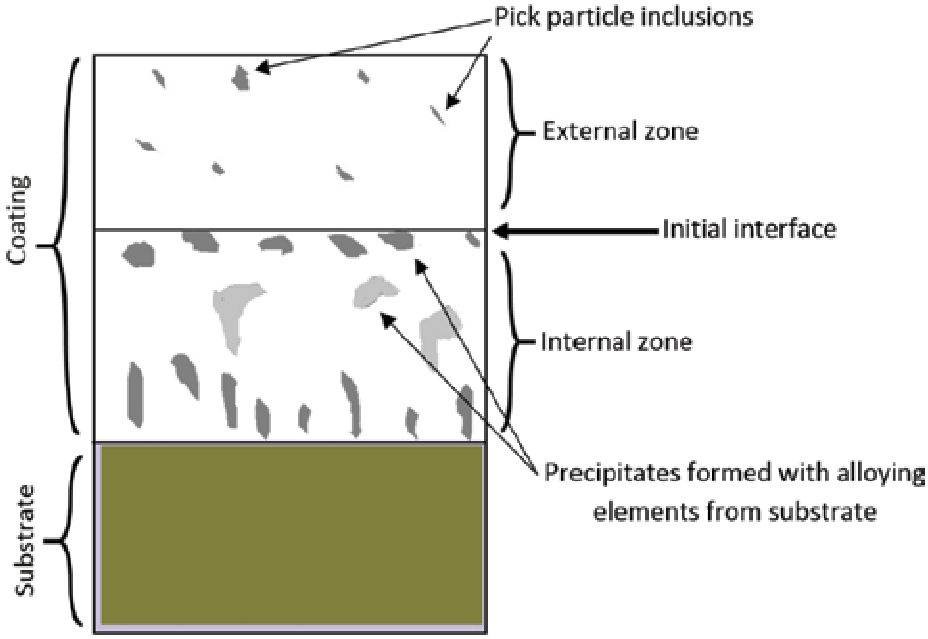

Figure 4. Schematic view of the aluminide coatings obtained from low activity-high temperatures.

The oxide formed in the form of a continuous layer on the alloy during the operation will be eventually damaged. Damage literally occurs when the thermal stresses cause cracks and oxide layer peeling. Then the oxidation process leads to re-formation of the most stable oxide, and then the alloy is gradually discharged from the element which is selectively oxidized and the transient oxidation stage becomes longer as well. Finally, forming stable oxide in the form of a continuous layer is not possible any more due to complete discharge of that element. Thus, the degradation sequence of alloys in oxygen includes expanding the most thermodynamically stable oxides and then oxides become less stable when the alloys are destroyed. The less stable oxides grow gradually in some areas and expand continuously. Therefore, in the case of systems which are resistant to oxidation, selective oxidation is important. Oxides which are thermodynamically stable and considered as effective barriers against oxidation include Cr_2O_3, α-Al_2O_3, and SiO_2. Chromite shells cannot be used at 1000°C because CrO_3 gas is formed and reduces the protection. Silica shells are also converted to gas products (such as SiO at low oxygen pressures). The alumina shells are very effective separators in preventing oxidation and the selective oxidation of aluminum is utilized to make α-Al_2O_3 protective shells widely used in alloys of the coating and in many structural alloys (such as B-1900) in order to improve the oxidation resistance. With continued oxidation, the oxidation rate increases by stabilization of less protective oxides. The length of stability for oxides depends on several factors. An important factor is composition, and coatings have the ability to re-spread more protective oxides for a longer period when compared to structural alloys. Oxidation conditions have also a significant effect on the formation of the protective shell. Higher temperatures and thermal cycles tend to shorten the time of protective oxide re-formation. Adhesion of the oxide separators to the alloys plays an important role in determining the oxidation resistance of alloys. There are several methods for improvement as well as adhesion of an oxide shell, such as addition of elements which react with oxygen, precious metals, and scattering of oxide particles [3].

3. Coatings

According to the production method, two categories of *high-temperature coatings* arise: diffusion coatings and overlay coatings. The most common overlay coatings used at high temperatures are MCrAlY and thermal barrier coatings.

3.1. Diffusion coatings

3.1.1. Chromium-rich coatings

Chromizing results in Cr enrichment of the surface layers. As for aluminizing, chromizing is affected by heating components in a gas rich in a volatile Cr compound (e.g. $CrCl_3$). An important usage of chromizing is in resistance toward type II hot corrosion and it has also been found to be of major benefit in protecting Ni-based alloys from corrosion by sulfatic deposits in chemical plants.

3.1.2. Aluminide coating

Aluminizing is performed by two different processes which differ in terms of the activity of aluminum in the gas phase and temperature of the process. The low activity-high temperature (LAHT) process is a "one-step" process as far as the development of a b-NiAl coating is concerned. The high activity-low temperature (HALT) method gives rise to a δ-Ni_2Al_3 coating which requires subsequent heat operations to convert it to δ-NiAl. The growth mechanisms of coating are different in these two processes. Since in the LAHT process the aluminum activity is insufficient, it cannot be the predominant diffusing species. Accordingly, coatings are formed by the diffusion of nickel from the alloy substrate into the region of the coating. **Figure 5** shows the microstructure of the aluminide coating. The outer area is usually β-NiAl phase which is rich in Al, whereas the internal area is rich in Ni.

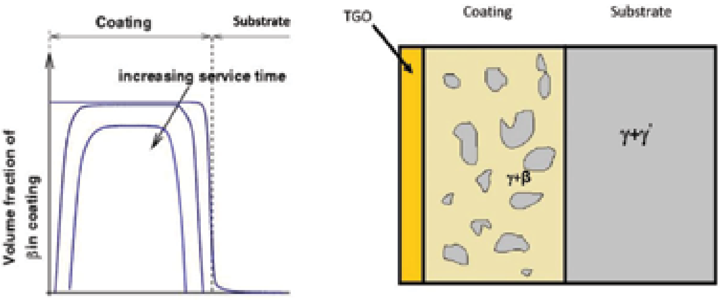

Figure 5. A view of the microstructure of the MCrAlY coating.

In the case of HALT process, the aluminum activity in the gas phase and at the surface of the coating is high enough to provide the inward diffusion of Al into the alloy substrate. The differing growth modes may be of importance when considering coating integrity, since coatings which grow by outward Ni diffusion can trap diluent particles (alumina) in aluminizing packs within them. Selection of the coating process depends upon a number of features, for example, heat treatment specifications for the substrate alloy, nature of available packs, integrity issues, etc. [2].

Unfortunately, aluminide coatings lose their flexibility at temperatures less than 750°C and one of the main problems dealt with in this type of coatings is thermo-mechanical fatigue, since the cyclic strains resulted by temperature gradient in the blades can lead to cracks caused by thermal fatigue.

3.1.3. Platinum-modified aluminide coatings

Since the use of diffusion aluminide coatings is limited at temperatures higher than 1000°C due to the internal diffusion as well as oxidation and accordingly wastage of aluminum from the surface over time, modified aluminide coatings were used.

Platinum-modified nickel aluminide coatings exist in two forms, a two-phase $PtAl_2$-(Ni-Pt-Al) or a single-phase Pt-modified b-NiAl. The method of forming coatings involves an initial deposition of a layer of platinum, typically 5–10 μm thick, by electroplating method. Annealing process is then performed to create diffusion bond between platinum and the substrate, and finally aluminizing leads to formation of the platinum-modified NiAl coating. If the pre-aluminizing heat treatment is performed such that significant platinum diffusion into the surface layers of the substrate occurs, the aluminide formed is of the single-phase variety. If the pre-aluminizing annealing is conducted such that platinum diffusion effects are small, then the bi-phasic $PtAl_2$-(Ni-Pt-Al) forms. Platinum helps the stability of the coating in several ways. First, it provides the surface phase which is rich in aluminum in order to form the continuous alumina oxide shell. Second, it improves the adhesion of the oxide shell formed on the surface of the coating despite thickening and increasing residual stresses. On the other hand, since platinum *is a refractory metal, it* leads to strengthen the outer layer and increases the hot-corrosion resistance of the aluminide layer. One of the main reasons for platinum addition was to try to suppress the diffusion of refractory elements (W, Mo) into the surface layers of aluminide coatings. The most probable beneficial effect of these coatings is to suppress void formation at the coating-alumina scale interface. Accordingly, the scale adhesion as well as oxidation and corrosion resistance improve [2].

In general, these coatings are commonly used at lower temperatures and in corrosive environments. Nowadays, the aluminide and platinum-aluminide coatings are widely used as a bond coat in thermal barrier coating systems. The application of platinum-aluminide coatings as a bond coat was first mentioned in 1993 in the patent of Duderstadt [4].

3.2. Overlay coatings

In the process of research aimed at developing better coatings for protecting superalloys at high temperatures, the issue of coatings independent of the chemical composition of superalloy in the overlay form or with a marginal influence arisen in the late 50th and the result of these researches was to assess the MCrAlY coatings [5].

Diffusion coatings' chemical composition depends on the chemical composition of the superalloy in addition to the foreign elements; in the case of overlay coatings, coatings do not form by reaction with the substrate, but a pre-alloyed material such as powder is utilized so that the chemical composition of this primary material determines the composition of the coating. Although composition of diffusion coatings depends on chemical composition of the substrate, a pre-alloyed material, such as powder, is used to form the overlay coatings, so that the chemical composition of primary material determines the final composition of coatings.

The major advantages of these coatings can be summarized as follows: (1) flexibility in choice of coating composition, (2) increased resistance to high-temperature corrosion and oxidation (compared with diffusion coatings), (3) flexibility in choice of coating thickness, and (4) high ductility compared with other coatings, especially the diffusion coatings.

MCrAlY coatings typically show a two-phase $\beta+\gamma$ microstructure. The presence of γ increases the ductility of the coating thereby improving thermal fatigue resistance. High-temperature exposure of the β-NiAl coatings results in depletion of the Al both to the thermally grown oxide (TGO) and to the substrate by interdiffusion. As the amount of Al decreases, the β phase tends to dissolve. For this reason, it is often described as an aluminum reservoir, and coating life is often measured in terms of depletion of β.

3.2.1. Composition and role of additives

The M of MCrAlY stands for either Ni or Co, or a combination of both. Cr provides hot-corrosion resistance, but the amount that can be added is limited by the effect it is expected to have on the substrate, and the formation of Cr-rich phases in the coating. Al content is typically around 10–12 wt%. Since oxidation life is essentially controlled by the availability of Al, it would be tempting to increase the aluminum content. However, this leads to significant reduction of ductility. MCrAlY typically contains 1 wt% yttrium (Y), which enhances adherence of the oxide layer. It was initially thought that yttrium helped the formation of oxide pegs which helped anchor the oxide layer to the coating. However, it is now believed that the main role of Y is to combine with sulfur and prevent its segregation into the oxide layer. Addition of hafnium (Hf) plays a similar role.

The effect of other additions has also been investigated. Silicon (Si) significantly improves the cyclic oxidation resistance; however, it also decreases the melting point of the coating; 5 wt% is enough to lower the melting temperature to about 1140°C. This element is also effective in the phase stability. For cyclic oxidation at 1000°C, 2.5 wt% is the optimum content. And further additions are detrimental. Addition of rhenium (Re) improves isothermal or cyclic oxidation resistance, and thermal cycle fatigue. Addition of tantalum (Ta) can also increase the oxidation resistance.

Some methods of applying the overlay coatings are given below:

- Thermal spraying techniques: they are divided into some categories such as atmospheric plasma spraying (APS), vacuum plasma spraying (VPS), and high-velocity oxy fuel (HVOF).
- Electron beam-physical vapor deposition (EB-PVD): this method is usually preferred to create high-quality coatings because certain amounts of particles usually oxidize during the thermal spraying and locate in splat interfaces.

The HVOF thermal spraying technique related to the MCrAlY coatings has been considered in recent years. In this method, the applied coatings exhibit higher density and hardness, less porosity, better adhesion strength, and minimum oxidation while much smaller compressive residual stresses are produced because the powder particles acquire a high kinetic energy during the spraying process and the flame temperature is lower [6–8].

The most recent technological advance in overlay coating technology is the development of so-called smart coatings by Nicholls et al. [9]. These coatings attempt to address the problems associated with the differences in temperature over the surface of an airfoil. Temperatures vary from a maximum of the order of 1100°C at the leading and trailing edges to about 650°C at the center of the airfoil surface and near airfoil roots. For this reason, the nature of environmental degradation varies from oxidation through type I hot corrosion to type II hot corrosion. The coating proposed by Nicholls et al. consists of three layers. C layer is applied directly on the substrate, B layer is the middle layer, and the A layer is applied as the surface layer. These multi-layer coatings have been shown to perform better than commercial Pt-modified aluminide coatings or an Al-enriched version of the base coat at 700–800°C. While this technology appears to be a step forward, issues related to coating ductility and additional improvements afforded by cobalt with respect to corrosion resistance are also of additional importance [2].

3.3. Thermal barrier coatings

These coatings, which are overlay coatings, are widely used for those components which are utilized in critical conditions of high temperature such as moving blades and combustion chamber.

The earliest ceramic coating was the coating of calcia-stabilized zirconia utilized for aerospace applications by the National Advisory Committee for Aeronautics (NACA). This coating applied on the exhaust nozzle of the X-15 manned rocket plane in the 1960s is believed to be the first use of TBCs [10].

Thermal barrier coatings become increasingly important for gas turbines and diesel engines. The use of zirconia in thermal barrier coating in Volvo Aero Corporation can be a good example of the rapid growth of this type of coating system. **Figure 6** shows that the consumption of zirconia has increased from 1000 kg in 1986 to 8700 kg in 1998.

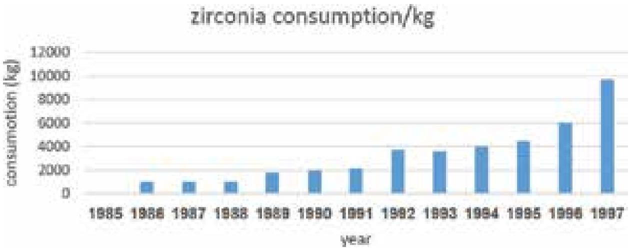

Figure 6. The amount of zirconia in Volvo plant.

TBC benefits include (1) increase in the service life of the component (mostly by decreasing the substrate temperature), (2) increase in the engine efficiency (by increasing the turbine inlet temperatures [TITs]), (3) reduction of the cooling airflow, the benefits of which are related to combustion improvement and engine efficiency. Because instead of cooling the piece, the air can be used to optimize the combustion [11].

The structure of thermal barrier coating consists of four layers—two ceramic layers and two metallic layers—with each layer having completely different physical, thermal, and mechanical properties. The thermal barrier-coated components must withstand the most extreme temperature, temperature cycling, and stress conditions, and they are expected to last thousands of takeoffs and landings in commercial jet engines and up to 30,000 h of operation in industrial gas turbine engines. The combination of the multimaterial nature of the TBC structure and the demanding operating conditions makes TBCs more complex than any other coating system. The TBC systems include four main elements: (1) the superalloy substrate, (2) the bond coat containing aluminum, (3) the thermally grown oxide (TGO), and (4) the ceramic topcoat [12] (see **Figure 7**).

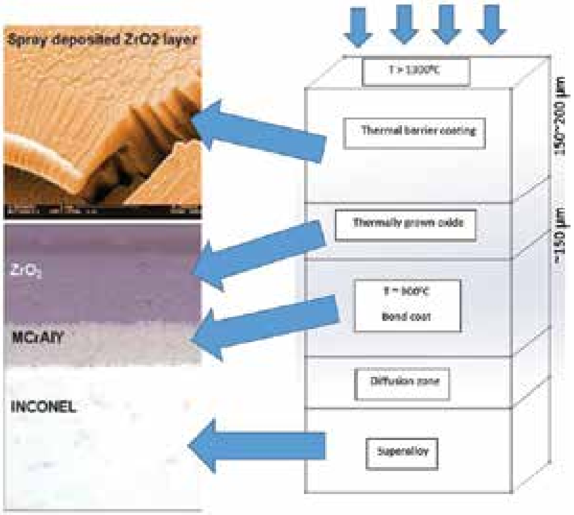

Figure 7. Schematic view of TBC coating system.

3.4. Nano-coatings

In fact, nano-coatings are kinds of thin layers which are in nano dimensions or have substrates in which nanoscale particles have been dispersed and cause special properties.

One of the cases where nanotechnology has been already used widely and effectively is the coating process and thereby production of the nanostructured materials. The performed investigations on the nano-coatings show that in many cases, their properties have significant improvements compared to the conventional coatings. Nano-coatings have a higher coefficient of thermal expansion, hardness, and toughness as well as higher resistance to corrosion, abrasion, and erosion in comparison to the micrometer coatings.

3.5. Types of nano-coatings

Four important groups of nano-coatings include:

1. Nano-grade coatings.
2. Superlattice and multi-layer coatings.
3. Thin-film coatings.
4. Nanocomposite coatings.

4. Conclusion

Different coating methods are used to extend the life of metal parts operating at high temperatures in the face of oxidation as well as hot-corrosion degradations. The efficiency of all types of gas turbine engines is proportional to the turbine inlet temperature. This increase in temperature after improving the structural design, selection of high-strength alloys at high temperatures, and turbine blade cooling technology is provided only using the protective coatings. High-temperature coatings are used in order to improve the resistance to oxidation and hot corrosion of gas turbine components such as combustion chambers and blades. By using these coatings, it is possible to increase the gas inlet temperature and thereby increase the efficiency. Ceramic thermal barrier coating (TBCs) which are often based on yttria-stabilized zirconia (YSZ) can reduce the surface temperature up to 200°C. However, due to noncompliance of the ceramic thermal expansion coefficient with the base metal, these coatings will be damaged. Using bond coats, this problem can be partly avoided. The aluminide bond coats as well as MCrAlY coatings are usually used to extend the life of thermal barrier coatings. One of the newest methods to apply the bond coat is the HVOF technique.

Author details

Masoud Shourgeshty, Mahmood Aliofkhazraei* and Mehrdad Mohammad Alipour

*Address all correspondence to: maliofkh@gmail.com and khazraei@modares.ac.ir

Department of Materials Science, Faculty of Engineering, Tarbiat Modares University, Tehran, Iran

References

[1] F.S. Pettit, G.H. Meier, N. Birks, Introduction to high temperature oxidation if metals, 2nd ed., 2009, Cambridge publication.

[2] Pomeroy, M. Coatings for gas turbine materials and long term stability issues. Materials & Design. 2005;26(3), 223–231.

[3] Nicholls, J., et al Smart overlay coatings—concept and practice Surface and Coatings Technology. 2002;149(2), 236–244.

[4] Pettit, F., Goward, G. Oxidation--Corrosion--Erosion Mechanisms of Environmental Degradation of High-Temperature Materials Coatings for High-Temperature Applications.1983; 1–32.

[5] Schmitt-Thomas, K.G., Hertter, M.Improved oxidation resistance of thermal barrier coatings Surface and Coatings Technology 1999.

[6] Wood, J.H., Goldman, E.H.Protective Coatings (for Superalloy) John Wiley and Sons, Superalloys II--High Temperature Materials for Aerospace and Industrial Power 1987.

[7] Okazaki, M. High-temperature strength of Ni-base superalloy coatings. Science and Technology of Advanced Materials 2001; 2(2), 357–366.

[8] Zhang, Y., et al A comparative study of DS NiCrAlY coating and LPPS NiCrAlY coating. Materials Science and Engineering: A 2003; 360(1), 65–69.

[9] Lugscheider, E., C. Herbst, and L. Zhao High velocity oxy-fuel spraying of a NiCoCrAlY and an intermatallic NiAl-TaCr alloy. Surface and Coatings Technology. 1998;108–109 (1–3).

[10] Zhao, L., Lugscheider, E.,. High velocity oxy-fuel spraying of a NiCoCrAlY and an intermetallic NiAl-TaCr alloy. Surface and Coatings Tecnology. 2002;149 (2–3) 230–235.

[11] Cao, X., R. Vassen, and D. Stoever. Ceramic Materials for Thermal Barrier Coatings. Journal of the European Ceramic Society. 2004; 24(1),1–10.

[12] Wigren, J., pejryd, L.,. Thermall barrier coatings-why, how, when and where to . in Thermal Spray-Meeting the Challenges of the 21st Century, ASM international park. 1998.

[13] Padture, N.P., M. Gell, and E.H. Jordan. Thermal barrier coatings for gas-turbine engine application. Science. 2002, 296(5566). 280–284.

Chapter 2

Steam Oxidation of Fe-Based Materials

T. Dudziak

Additional information is available at the end of the chapter

http://dx.doi.org/10.5772/62935

Abstract

Coal-fired power units are important player in energy production worldwide; however, during combustion, solid fossil fuels produce large amount of CO_2 and contribute to climate change, to inverse this process, higher efficiency of power plants can be achieved through out higher steam parameters (higher T, higher p).

This chapter is related to steam oxidation at high temperatures where important aspects of degradation are discussed.

Steam oxidation in close-loop system using deionised water was used to perform research at high temperatures.

Analyses were performed at temperatures in the range of 600–750°C for 2000 h. Different steels were included during analysis, such as T22, T23, T91, T92, E1250, 316L, 347HFG, Super 304, 309S, 310S, and HR3C. Kinetic data, metal loss data, and microscopic investigations were performed in order to evaluate corrosion degradation of ferritic and austenitic steels.

Keywords: Steam oxidation, high temperature, coal power plants, metal loss, corrosion resistance, SEM, BSE, EDX, XRD

1. Introduction

Development of industry in the beginning of twentieth century is associated with combustion to produce heat and electric energy. The reserves of coal around the globe are massive, according to the US Energy Information Administration (EIA) coal reserves at 948×10^9 tons [1] are estimated; in contrast to gas or oil, coal is distributed more equally around the globe and is far cheaper, therefore more accessible for industry needs.

Although coal is more accessible than other fossil fuels; globally, the coal-burning process is responsible for high level of CO_2 emissions. It is report [2] that coal-fired electric power stations emit, on average, 1000 kg of CO_2 for every megawatt-hour [MWh] generated, which is more than twice the approximate amount of CO_2 released by a natural gas-fired electric plant, 550 kg of CO_2 per megawatt-hour [MWh] generated. Coal-fired power stations are one of the main CO_2 emitters and contributor to climate change. It is predicted that coal (hard coal or lignite) still stands as the main source of energy production in the next 20 years and will be responsible for even higher CO_2 emissions [3]. Moreover, energy production is predicted to grow yearly by 2.2% from 2008 to 2035 [4]. According to the International Energy Agency (IEA) energy statistics, electricity and heat production accounts for 41% of the total CO_2 emissions [5]. Conventional solid fossil fuel power plants contribute significantly to the global CO_2 emissions as discussed in the previous studies. The European Union (EU) has put restricted legislation in place in order to significantly reduce emissions from EU coal-fired power stations to 20% by the year 2020 in reference to the level in 1990 [6]. Recently, the observed significant changes in electric power sector related to reducing CO_2 emissions are strictly associated with groundbreaking development in material science and engineering. Throughout the last decades, tremendous progress has been achieved in the development of steels and technologies associated with energy production. Progress in steels performance for coal-fired power can be illustrated by the following numbers of outlet steam pressure and temperatures [7] leading to CO_2 decrease:

1. 1970s of the twentieth century: T = 538°C/538°C/16.7 MPa (167 bar),
2. 1980s of the twentieth century: T = 540°C/560°C/25.0 MPa (250 bar),
3. 1990s of the twentieth century: T = 560°C/580°C/27.0 MPa (270 bar),
4. Turn of the century twenty to twenty-first: T = 600°C/620°C/29.0 MPa (290 bar) USC,
5. In 2020 of the twenty-first century: T = 70°C/720°C/350 MPa (350 bar) AUSC.

Between 1970 and 2020, the outlet steam temperature increased approximately 150°C, whereas pressure reached as high as 350 bar in 2020 compared to 167 bar in 1970, showing the progress that has been achieved during the last 50–60 years. Among, the listed numbers, ultrasuper critical (USC) and advanced ultrasuper critical (AUSC) present the harshest conditions for structural steels, the steels facing high temperatures and pressures. The materials that were developed over 50–60 years ago are no longer currently suitable for USC and AUSC regimes due to poor corrosion resistance and inadequate high-temperature creep and strength properties. These technologies require austenitic steels and nickel (Ni)-based alloys with superior steam oxidation resistance. **Figure 2** shows creep strength versus temperature dependence for the most commonly used materials in coal-fired power sector.

Figure 1 further illustrates the correlation between efficiency and temperature in coal-fired power stations.

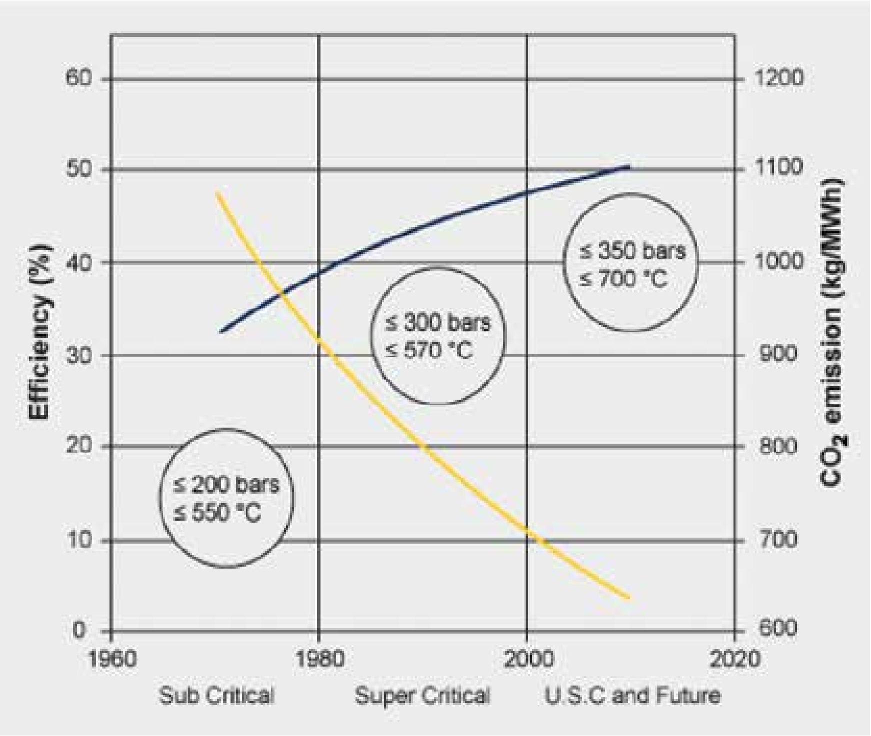

Figure 1. Effect of operating conditions on efficiency and emissions of steam power plants.

Development of materials for the energy sector, in terms of pressures and temperatures in superheaters (SH) and reheaters (RE) sections, is as follows [8]:

1. Ferritic steels: $p < 26$ MPa (260 bar), $T = 545$°C
2. Ferritic martensitic steels: $p = 26$ MPa (260 bar), $T = 545$°C
3. Austenitic steels: $p = 29$ MPa (290 bar), $T = 600$°C
4. Ni-based alloys: $p > 35$ MPa (350 bar), $T > 700$°C

Development of USC- and AUSC-based coal-fired power plants requires high-performance steels and Ni-based superalloys as shown in **Figures 1** and **2**. Reduction in CO_2 emissions from coal-fired power plants can be achieved by increasing the operating temperature (pressure) of water steam systems, which can give an increase in overall plant efficiency (**Figure 1**). Generally, 1% increase in absolute efficiency results in as much as 3% reduction in CO_2 emissions [9]. Hence, an increase in efficiency from 36 % (subcritical power stations) to 50–55% (USC and AUSC) leads to reduction of around 50% CO_2 emissions. Higher temperature means higher efficiency; however, higher corrosion rates occur in a steam atmosphere when ferritic, ferritic-martensitic, or medium Cr–Ni steels are used.

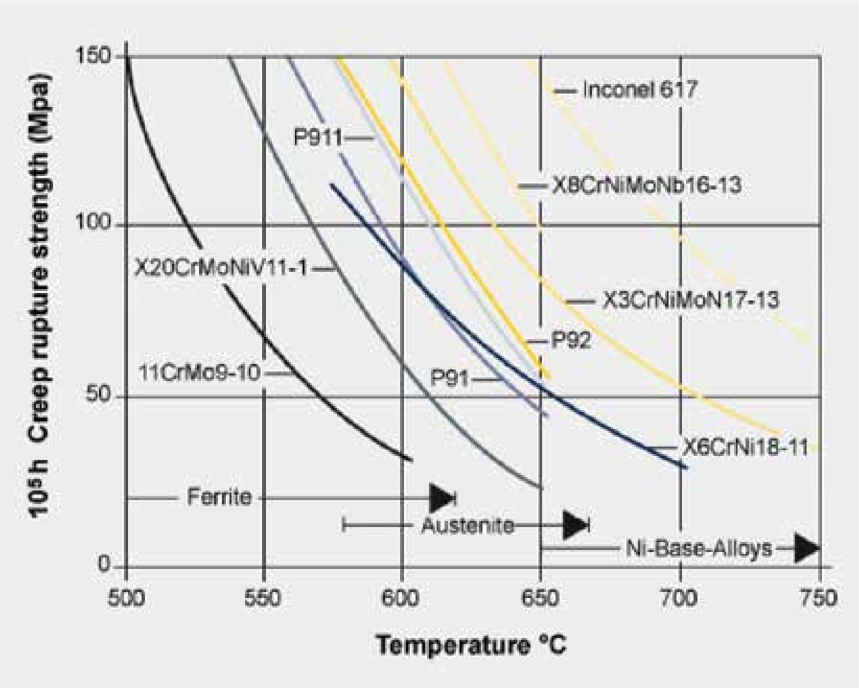

Figure 2. Materials for main steam pipes in power plants.

This chapter shows high-temperature steam corrosion degradation in the simplest way for the reader who wants to understand the fundamentals of corrosion phenomena at high temperatures.

2. Experimental procedure

2.1. Steam oxidation

Steam oxidation test rig, shown in **Figure 3**, was used to perform tests at high temperatures in a close loop [10]. Steam was generated by pumping highly purified deionised water from a reservoir placed underneath the furnace. In the furnace water, steam passes over the test samples and flows into a condenser before the water returns to the reservoir. The water used in the reservoir was double deionised.

The whole system was sealed using stainless steel flanges from both ends. Prior to steam oxidation test, the whole system was purged using oxygen-free nitrogen (OFN). Throughout the samples exposure period, this purge continues through the water reservoir in order to minimise the level of oxygen in the system. Prior to the high-temperature steam exposure, the furnace calibration was performed in order to place the materials in the middle of the hot zone. The calibration process ensured placement of the samples in the furnace at test temperature with an accuracy of ±5°C. Postexposed investigations of the samples covered the following:

macro and microexaminations using digital camera with macrolenses, environmental scanning electron microscope (ESEM) operating in backscatter electron mode (BSE) for better contrast, and a better phase designation. Finally, chemical analyses using energy X-ray-dispersive spectrometry (EDX) was employed to quantity examination of the corroded materials under steam conditions at elevated temperatures.

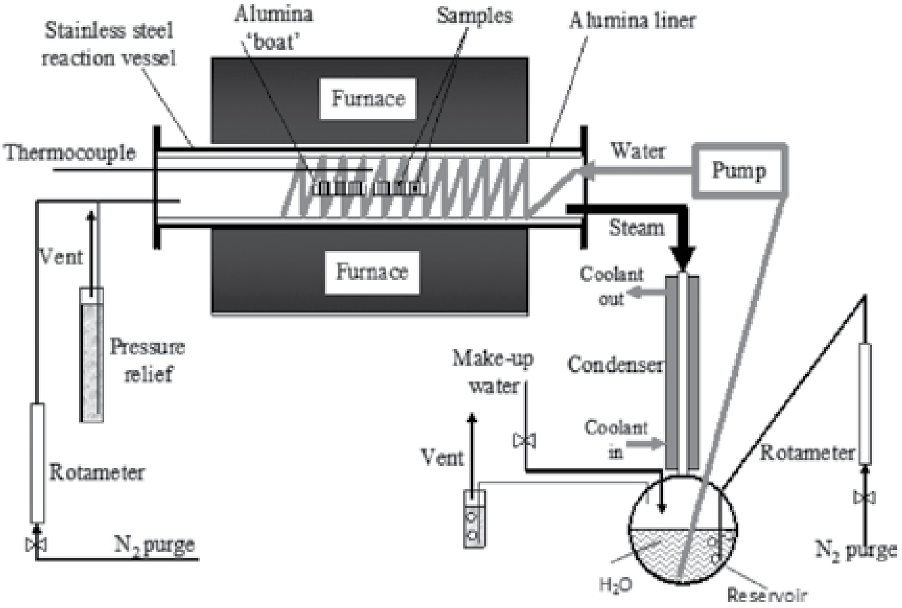

Figure 3. Steam oxidation rig used for the investigations of corrosion resistance in a steam atmosphere [10].

3. Materials

The materials, presented in the chapter, utilise most of the steels used in currently operating coal-fired power plants in Europe. Two main groups of the steels are distinguished as ferritic steels and austenitic steels. Ferritic steels represent the family of steels with adequate strength at high temperature up to 600°C (**Figure 1**), with relatively good corrosion resistance up to 500–550°C. The group possesses high coefficient of thermal conductivity (CTE), 50% higher than that met in more expensive austenitic steels. Furthermore, the ferritic steels show low coefficient of thermal expansion. The ferritic steels may contain high concentration of Cr, with the lack of Ni. The materials are mostly used in cooler areas of superheaters (SH) and reheaters and also in waterwalls in the temperature range where mild steels become too susceptible to creep. In general, the characteristic of ferritic steels can be shown as follows:

- Acceptable tensile strength (120 MPa) at temperatures up to 450°C
- Good creep properties at temperatures up to 550°C for 100,000 under 100 MPa

- Excellent weldability with no requirements for additional post-weld treatment (T22, T23 steels)
- Adequate steam oxidation up to 550°C

The family of ferritic steels can be divided further into several grades:

- GRADE 11 – P11/T11/13CrMo4 4
- GRADE 22 – P22/T22/10CrMo 9 10
- GRADE23 – P23/T23/HCM2S
- GRADE 24- T24/7CrMoVTiB10-10
- 1CrMoV

Austenitic steels are the family of materials with better corrosion-resistant properties with the addition of Ni and Cr to metal matrix. The steels are used in USC and A-USC coal-fired power plants in sections where materials cheaper than Ni-based alloys, with similar properties, are needed. The austenitic steels possess higher creep rapture strength at elevated temperatures than ferritic steels; nevertheless, the steels combine high CTE and poor coefficient of thermal expansion. The family was designed in order to increase the volume-strengthening precipitates fraction by replacing chromium carbides with more stable carbides, simultaneously freeing chromium to enhance corrosion resistance at elevated temperatures. The family of austenitic steels includes the following steels; AISI 302, 304, 321, 347, 316, 309, 310, ASME TP347HFG, Tempaloy A-1, Tempaloy A-3, Super304H, HR6W, NF709, and Esshete 1250 (E1250) The chemical composition of the steels reviewed in the chapter is listed in **Table 1**.

Material	Fe	Cr	C	Si	Mn	P	S	Al	Mo	V	Nb	Nb + Ta	W	Cu	B	Co	N	Ni
15Mo3	Bal.	-	0.16	0.35	0.60	≤0.035	≤0.035	-	0.30	-	-		-	-			-	-
T22	Bal.	2.25	0.10	0.25	0.45	0.0125	0.0125		1.00									
T23	Bal.	2.50	0.06	0.20	0.46	0.014	0.001		0.08	0.25	0.05		1.54		0.0023			0.14
T91	Bal.	8.36	0.10	0.12	0.45	0.003	0.009	0.022	0.90	-	-		-	0.017				
T92	Bal.	8.79	0.11	0.39	0.34	0.015	0.030	0.041	0.91	0.24	0.07		1.87					
E1250	Bal.	15.00	0.10	0.50	6.30	≤0.035	≤0.015	-	9.50	0.30	1.00		-	-	0.0050		-	9.50
316L	Bal.	16.60	≤0.003	0.60	1.80	≤0.040	≤0.030	-	2.10	-	-		-	-	-		-	11.00
347 HFG	Bal.	17.00	0.08	0.75	2.00	0.040	0.030		-	-	-		-	-	-		-	10.00
Super 304H	Bal.	18.40	0.10	0.20	0.80	0.045	0.030							3.00	-		0.1	8.80
HR3C	Bal.	25.00	0.06	0.40	1.20	-	-	-	-	-	0.45		-	-	-		-	20.00
309S	Bal.	23.00	0.08	0.75	2.00	0.045	0.03	-	-	-	-	-	-	-	-	-	-	14.00
310S	Bal.	25.00	0.20	1.50	2.00	0.045	0.03	-	-	-	-	-	-	-	-	-	-	21.00

Table 1. Chemical composition of steels currently in operation in coal-fired power plants.

4. Test results

4.1. Ferritic steels

Ferritic steels, such as 15Mo3, T22 and T23, under steam oxidation, have shown formation of nonprotective scale at temperatures higher than 600°C. The steels show lower values of operating temperature based on 100,000 h average stress rapture strength of 100 MPa than austenitic steels and Ni-based alloys. The formation of non-protective, thick scale is shown in **Figure 4** as an example of the T22 steel exposed at elevated temperatures, and higher temperature of the exposure as required was selected in order to present more clearly mechanism of ferritic steel degradation in a steam atmosphere.

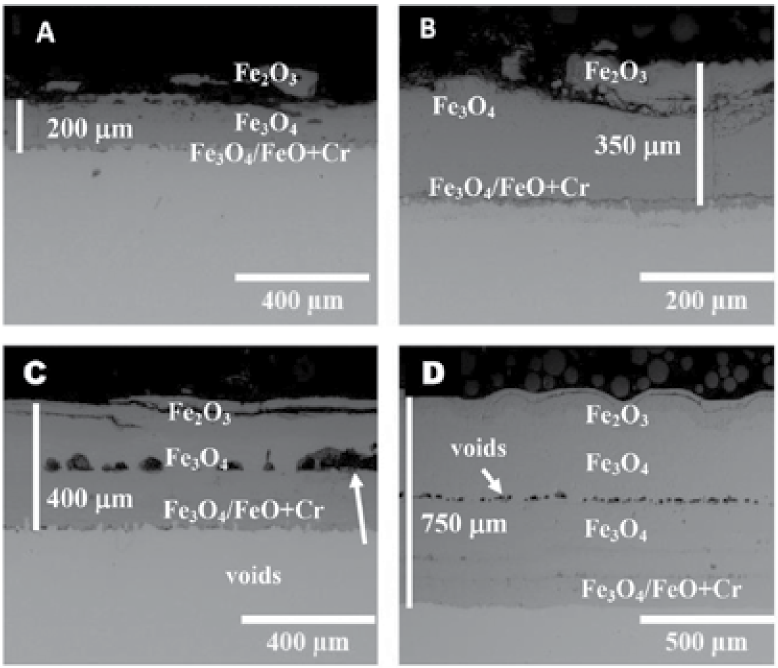

Figure 4. Cross-sectional image of T22 steel exposed in water steam at temperature: (A) 600°C, (B) 650°C, (C) 675°C, and (D) 700°C for 500 h (unpublished work, part of the project).

The T22 steel with ~2.25 wt% Cr under steam oxidation shows the formation of three oxides at high temperature [11]. The presented results indicate the formation of thick oxide scales consisting Fe_2O_3 (hematite), Fe_3O_4, (magnetite), and FeO (wustite). The formation of all three oxides is expected under steam oxidation conditions. Under 1 bar pressure, the oxygen partial pressure from the equilibrium dissociation of steam is high enough (two orders of magnitude higher) than the dissociation oxygen partial pressure required for Fe_2O_3 oxide [12]. Hence, development of thick scale is more than expected on steels belonging to ferritic family with GRADES 11, 22, 23, and 24. The Cr reservoir in such steels was not concentrated enough to form thin protective scale. Ferritic steels with low concentration of Cr at temperatures above 580°C are covered predominantly with thick scales containing three types of oxides. Below 570–580°C formation of FeO is was not possible since the oxide is unstable. Hence, the steels exposed in steam environment below 580°C present much thinner oxide scale consisting Fe_2O_3 and Fe_3O_4 with diffused concentration of other elements such as Mn, S, and Cr. The total concentration of these elements rarely exceed 7 wt%. Voids were observed only at 675 and 725°C T22 steels, suggesting the highest rate of diffusion in both directions at these temperatures. The voids appear to be located at the original steam—substrate interface, suggesting two different mechanism of oxidise scale formations, the mechanism consider outward and inward diffusion of iron and oxygen ions, respectively. Some authors postulate that oxide scale on low ferritic steels grows by the outward diffusion of Fe [13], because Fe diffusion coefficient in iron oxides is much higher than that of oxygen [14]. Some authors, postulated, inward diffusion of oxygen, due to accelerate diffusion of oxygen throughout the grain boundaries [15]. The mechanism of voids formation has different variety that depends on author and scientific approach; in this chapter, the mechanism of void formation can be formulated in the following way: consider the diffusion couple between A (Fe_3O_4+Fe_2O_3 top layer) and B (Fe_3O_4+FeO+Cr bottom layer) in **Figure 4C** and **4D**, respectively. Both of these layers constitutes with different phases, showing different chemical potential, different ion flux, diffusion and number of defects giving different diffusion fluxes J. Since the diffusion fluxes are different, there will be a net flow, causing the couple to shift bodily. This can only occur if diffusion is by a vacancy mechanism between two layers (A and B). It should be noted that voids are formed at the original steam—substrate surface interface. Quadakkers et al. [16] showed that the voids formation can be observed on the ferritic oxide scale after long-term exposures that can be unevenly distributed or can coalesce to form a crack or a gap at the interface between the inner and outer layer. The formation of pores in the oxide scale may create significant consequences for mechanical and thermal properties. The low-alloyed ferritic steels developed thick oxide, originated from the phase structure and defects number within the crystallographic structure of the individual oxide. At temperatures above 570°C, FeO phase become stable under steam oxidising conditions; hence, oxide scale possesses three layers at temperatures above 570°C. For better clarity, and better understanding, **Figure 5** shows iron oxide phase stability at high temperatures [17].

The stability of FeO depends on two main factors, namely temperature and Cr concentration. The presence of FeO, in the oxide scale, dramatically accelerates thickness of the scale since the phase has higher Fe_3O_4 number of interstitial defects (support iron ion diffusion). Iron vacancies in FeO are responsible for the defects [18]; however, in Fe_3O_4, the main defects are localised in iron sublattice, neutral iron interstitials at low oxygen activity, and neutral iron vacancies at high oxygen activity. In Fe_2O_3, majority of the defects can be found in the oxygen sublattice than in iron sublattice. Generally, ferritic steels form multilayered scale [19], where predominantly Fe_3O_4 and FeO forms together with a thin layer of Fe_2O_3 can be observed. In steels with low Cr content, a thin layer enriched in Cr can be observed, some authors suggest formation of iron chromium spinel $FeCr_2O_4$ [20]. The findings are rather questionable since the concentration of Cr in the steels reaches 2–3 wt%, whereas development of iron-chromium spinel $FeCr_2O_4$ requires much higher concentration of Cr in bulk steel. Chemically, $FeCr_2O_4$

spinel should contains around 46 w% Cr, 25 wt% Fe, and 29 wt% O. The low-alloyed steels, due to low concentration of Cr in bulk steel, are unable to deliver through outward diffusion, showing that high concentration of Cr need for $FeCr_2O_4$ spinel development. In the case of low-alloyed steels, Cr-enrichment layer was formed with poor corrosion resistance. Formation of spinel as suggested by [11] should significantly decrease corrosion degradation because $FeCr_2O_4$ spinel possesses much lower number of defects, hence higher corrosion resistance than Fe_3O_4 and FeO phases. Similar to T22, the T23 steel with the addition of W, V, and Nb was introduced to achieve enhanced creep behaviour at higher temperatures [21] compared to T22 steel. In contrast to Lepingle et al. [22], it was found by T. Dudziak et al. [23] that the T23 steel showed a better corrosion resistance than that offered by the T22 steel. A slightly better corrosion resistance of the T23 in comparison with T22 can be related to W addition, when added, W through the chemical reaction with C, forms WC carbide:

$$W + C \rightarrow WC \tag{1}$$

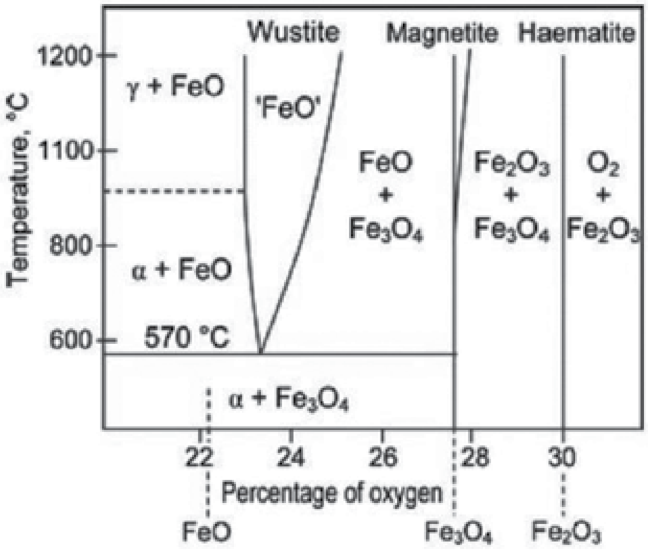

Figure 5. Iron-oxygen phase diagram [17].

Thus, due to the higher activity of Cr in T23, more Cr diffuses to the interface where enriched Cr layer or Fe_2CrO_4 spinel can form. However formation of $FeCr_2O_4$ spinel is rather unlikely to occur.

In contrast, in low-alloyed steels such as T22, Cr directly reacts with C to form carbides such as Cr_3C_2, Cr_7C_3 and $Cr_{23}C_6$ [24]. Hence, lower concentration of Cr in the bulk material, and lower activity of Cr, thus lower quantity of Cr diffuses to the surface, as a result thicker, with poor corrosion resistance oxide scale is forming. The comparison of T22 and T23 steels in terms of metal loss is shown in further part of this chapter. However, the results showed that T23 steel has a better corrosion resistance and lower metal loss at elevated temperatures. **Figure 4** shows scanning electron microscope (SEM) images in backscatter electron (BSE) mode of T22 and T23 steels exposed for 500 h at elevated temperatures. The images shown in **Figure 6** indicate distinct differences in thickness of the formed oxide scale.

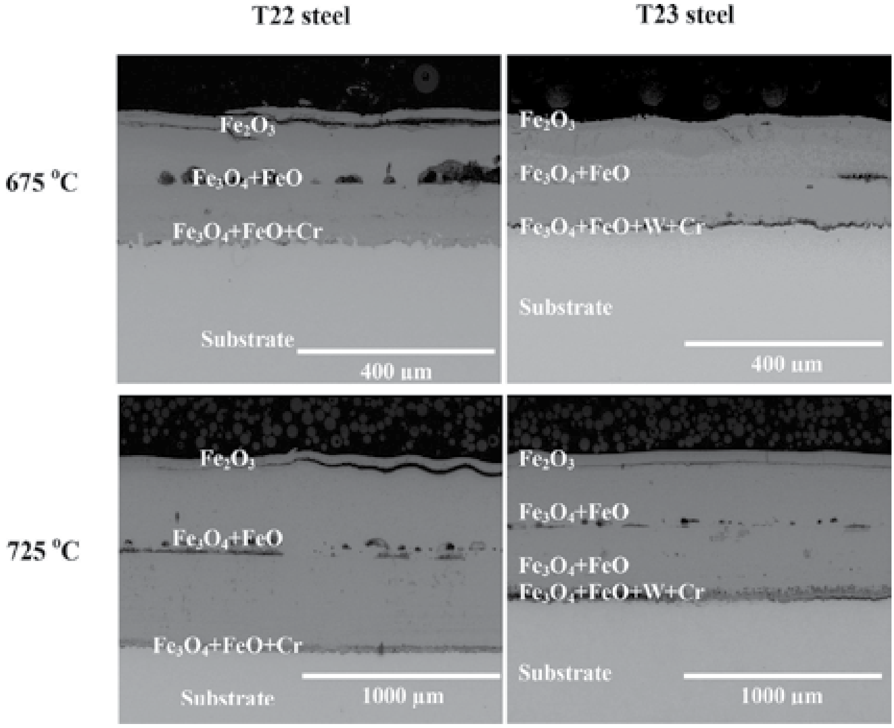

Figure 6. Comparison of oxide scale thickness between T22 and T23 ferritic steels exposed at 675°C and 725°C for 500 h.

4.2. Ferritic-martensitic steels

The steels with higher concentration of Cr in a matrix under high-temperature exposure in steam showed a better corrosion resistance. Similar to T23 in T92 steel, addition of W was introduced in order to enhance creep behaviour of T92 in relation to T91.

Because of a slightly higher concentration of Cr in ferrite matrix, the oxide morphologies in both steels are different compared to the low-alloyed steels. In general, the scale consists of different layers than that observed in the T22 and T23. Because T91 ferritic-martensitic steel showed a better corrosion resistance than that offered by T92 steel; in this chapter, the author mainly focuses on the T91 steel. Both steels were exposed at elevated temperatures:

1. T91 steel at $T = 700$, 750, and 800°C
2. T92 steel at $T = 600$, 650, 700, and finally 750°C.

In the T91 steel, the top part of the oxide scale was occupied mostly by Fe_3O_4 not by Fe_2O_3, some patches of Fe_2O_3 were observed, the inner layer consists thick band of Fe_3O_4 and the most inner layer consisted $(Fe,Cr)_3O_4$ spinel rich in Cr up to 11%. In terms of T92, the inner scale consisted $(Fe,Cr)_3O_4$ spinel with similar concentration of Cr as in the T91 steel. However, the presence of W at the oxide scale—the substrate interface was observed with concentration of W (varied from 2–5 wt%).

The findings in the T91 and T92 steels in relation to Cr content at the interface, the oxide scale —the substrate are in contradiction with the proposed values by Viswanathan et al. [25].

The author [25] proposed that steels with 9% Cr content should develop an enriched layer with as high as 45 wt% Cr at the oxide scale the substrate interface. However, in both 9 wt% Cr steels exposed at a steam atmosphere, concentration of Cr at the interface reached only about 13 wt% Cr.

The steel with 9 wt% Cr were exposed at temperatures higher than 570°C similar to the low-alloyed steels; therefore, high-temperature promoted development of FeO layer. On one hand, the formation of FeO is possible only at temperatures higher than 570°C, and upon the FeO phase, cooling may undergo eutectoid reaction forming mixture of Fe_3O_4 and Fe [26]. On the other hand, when the cooling process is high enough, FeO may be found at temperatures below 570°C. In addition to these, FeO may undergo oxidation to form Fe_3O_4 when oxidation is preceded under continuous cooling process.

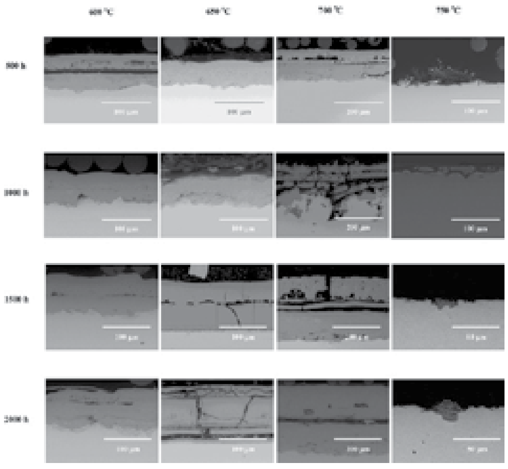

Figure 7. Cross-section images of ferritic martensitic T91 steel exposed in temperature range 600–750°C for 2000 h in a steam atmosphere.

Because diffusion of iron in FeO is extremely high, much higher than in Fe_3O_4, diffusion of oxygen and iron in Fe_2O_3 is extremely slow [27]. As a result, FeO possessed 90–95% of the total thickness of the oxide scale. However, this is a general remark, the percentage ratio can vary due to different external conditions; temperature, pressure etc. At higher temperature, above 570°C but below 650°C, the thickness of Fe_2O_3 and Fe_3O_4 layers increases. However, FeO is still the major contributor in the oxide scale thickness. As mentioned, previously, FeO is unstable at temperatures below 570°C and starts to decompose.

In this study, formation of relatively thick Fe_3O_4 at temperatures 600–700°C was observed in T91, the results are shown in **Figure 7**. At higher temperature, the steels T91 and T92 show similar behaviour, where thin oxide scale developed after 500 and 1000 h of exposure, while after further exposure nodules formation were observed. The highest temperature of exposure show the development of nodules that possess two layered structure. The formation of nodules can be shown according to **Figure 8**. In the first stage of exposure in the steam oxidation atmosphere with high partial pressure of O, the steel with 9 wt% Cr develops thin protective $(Fe,Cr)_3O_4$ spinel scale. Since the concentration of Cr is limited to the formation of $(Fe,Cr)_3O_4$ spinel scale, no more Cr could outwardly diffuse from the metal matrix to sustain protective scale. In the same time, high activity of Fe ions, formed diffusion of Fe to the surface throughout spinel layer, showing the formation of nodule consisted high concentration of Fe. The formation of nodule is related to high flux of Fe ions that diffuses from the matrix and formed magnetite layer on the $(Fe,Cr)_3O_4$ spinel scale, as shown below. It was found that the amount of Fe_2O_3 on the surface was decreasing with increasing temperature; at 600°C, more Fe_2O_3 was found than at 750°C. Thus, the formation of Fe_3O_4 is more favourable at higher temperatures. These findings have been confirmed by Dudziak et al. [28].

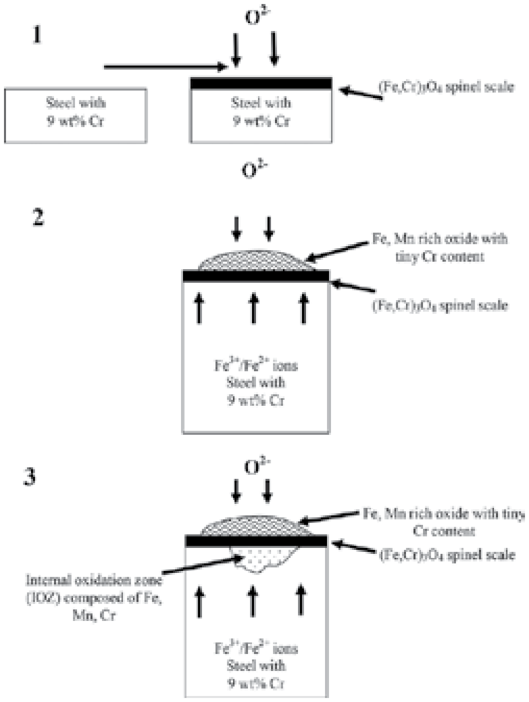

Figure 8. Development of nodule in 9 wt% Cr steel under the steam oxidation conditions.

The corrosion of 9 wt% Cr steels in a steam atmosphere obeys the formation of two-layered nodule, the nodule consists high concentration of Mn and Fe; 18 and 47 wt%, respectively, O content reaches 32 wt%, with Cr concentration equivalent to 3 wt%. The internal oxidation zone (IOZ), underneath the formed nodule, was observed after 1000 h exposure at 750°C. The IOZ consists of the mixture of Cr, Mn, and Fe oxides with variety of concentration.

It is believed that due to addition of W to the metal matrix, similar to T23 and T22, more free Cr can diffuse outwardly to the surface of the exposed material which indicates a higher Cr activity. This is due to the formation of WC (tungsten carbide) phase instead of Cr_3C_2, Cr_7C_3 and $Cr_{23}C_6$ phases. The higher Cr activity has a consequence in the formation of more protective $(Fe,Cr)_3O_4$ spinel scale, which is likely to occur in T92 compared to T91 steel. Metal loss data for T91 and T92 steels are shown in the last section of this chapter.

4.3. Austenitic steels

This subchapter provides information regarding austenitic steels with Cr concentration higher than 10 wt% Cr in the metal matrix. The steels (with 12 and 16 wt% Cr) in the matrix were tested in the same conditions as the low-alloyed and 9 wt% Cr steels. **Figure 9** shows cross section images in BSE mode for E1250 and 316L steels. The E1250 steel showed development thin, protective but extremely brittle oxide scale. Under the steam oxidation conditions, the scale showed lack of adherence at the peak of concave geometry. The behaviour is related to tensile and shrink stresses upon heating and cooling from high temperature to room temperature. Furthermore, delamination and poor adherence is related to the formation of a very thin oxide scale. A thin oxide scale with lack of plasticity and lack of relaxation energy could not consume stresses released upon heat treatment. Finally, delimitation of the oxide scale was found on the surface with the highest inclination angle. It can be concluded that exfoliation of the formed oxide scale can be invoked by different coefficient of thermal expansion (CTE), while CTE depends directly from chemical composition and microstructure.

The brittleness of the formed oxide increases with time of exposure and temperature; in contrast to E1250 steel, the 316L with 16 wt% Cr indicated the formation of a thin, protective and adherent oxide scale under the steam oxidation conditions at 700–800°C. The E1250 steel showed formation of a thick scale at 800°C, indicating limited usability of the steel in a steam atmosphere. Such behaviour indicates that concentration of 12 wt% Cr is suitable for conditions where steam temperature reaches lower values below the range 750–800°C. Above this temperature, acceleration in thickness of the oxide is observed.

The presented results, in **Figure 9**, clearly demonstrates, that 16 wt% Cr steel has shown significantly better corrosion resistance in steam environment at temperature as high as 800°C. The scale consisted a single oxide layer; however, a thick layer varies with composition; the top part of the oxide scale consist 7 wt% Cr, 5 wt% Mn, 4.5 wt% Ni, and 57 wt% Fe, respectively. The bottom part of the oxide scale was rich in Cr with 14 wt%, and relatively low content of Mn (3 wt%), high Ni concentration (20 wt%), and rich Fe content equivalent to 43 wt%.

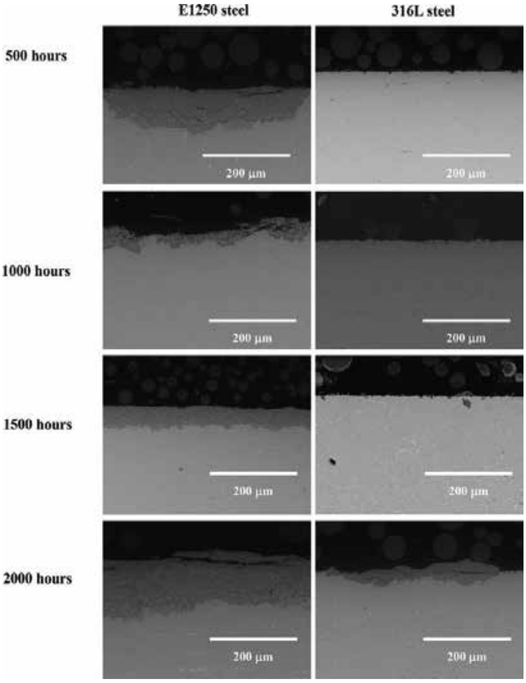

Figure 9. Cross-sectioned images performed via SEM in BSE mode of two austenitic steels with 12 wt% Cr E1250 and 16 wt% Cr 316L steels exposed at 800°C for 2000 h in a steam atmosphere.

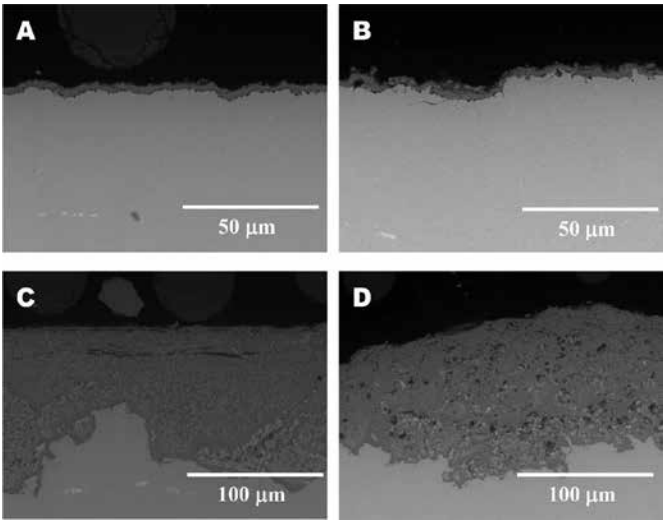

Figure 10. Cross-sectioned images performed via SEM in BSE mode of two austenitic steels with (A, C) 17 wt% Cr and (B, D) 18 wt% Cr steel exposed at 800°C for 2000 h in a steam atmosphere.

Alternatively, the steel with 16 wt% Cr manifests the formation of a thin, protective oxide scale rich in Cr (36 wt% Cr, 30 wt% Fe, 6 wt% Ni, and 2 wt% Mo) suggesting the formation of $(Fe,Cr)_3O_4$ spinel with the incorporation of additional elements. However, long exposure of 16 wt% Cr steel at high temperature indicated the likelihood of the formation of nodules. The nodules with double-layered structure were found; the external part of nodule consisted high concentration of Fe (60 wt%), relatively low Cr and Ni content (9 and 4 wt%). Internal part of nodule consisted much higher Cr concentration (20 wt%) and higher Ni content (20 wt%). Nevertheless, nodules were distributed randomly in 16 wt% Cr steel compared with 12 wt% Cr steel showing a better corrosion resistance.

The cross-sectioned microstructures of 17 wt% Cr (TP347HFG) and 18 wt% Cr (Super 304) are shown in **Figure 10**. In comparison to E1250 and 316L austenitic steels showed better performance in a steam atmosphere. The steels were exposed in the same conditions using the same test rig presented in **Figure 3**. The steels with 17 and 18 wt% Cr were exposed only at 800°C. The steels showed similar behaviour in steam conditions; however, better corrosion resistance than the materials with lower Cr content.

The oxide scale formed on the exposed materials showed thickness in the range of 2–5 μm, and the scale of 347HFG consists of high levels of Cr, Fe, and oxygen with concentration of 19, 47, and 25, respectively, indicating formation of Fe-Cr spinel. Concentration of Ni in the top part of the oxide scale showed value close to 6 wt%. Relatively high concentration of Ni found in the top layer suggests the formation of porous oxide scale under the steam oxidation conditions. Saunders et al. [29] reported that steels exposed in a steam atmosphere in general, promotes the formation of a more porous scale. This is related to an increase in cation diffusion and consequent vacancy condensation, thereby developing a porous structure. Enriched layer of Cr was found in the oxide scale—the substrate interface where concentration reached 33 wt %, with a tiny amount of Mn (2.9 wt%) and Ni (6.4 wt%). In comparison, the steel with 18 wt % showed rich in Cr oxide scale with concentration of 33 wt%, 30 wt% Fe, 3.3 wt% Ni, and 2.2 wt% Cu. Copper addition stabilise austenite structure, hence, improve outward Cr diffusion, presenting the formation of enriched Cr oxide scale in comparison to 347HFG steel. Both steels formed the oxide scale with good adherence, spallation was observed under the steam oxidation conditions.

Highly alloyed steels, such as 309S, 310S, HR3C, are used in coal-fired power plant industry for the hottest sections of superheaters (SH) and reheaters (RH). The steels were tested under scientific grant funded from the National Science Centre in Poland. Grant number: 2014/13/D/ST8/03256, entitled:

> *Development mechanism of thermodynamically stable, thin and protective oxide scales formation at high temperatures in pure water steam on the material based on Fe and Ni structures with high chromium content.*

The steels with Cr content higher than 20 wt% Cr were exposed for 2000 h at 800°C. The steels HR3C, 309S, 310S were tested in the same the steam oxidation rig, presented in **Figure 3**. The steam oxidation tests were performed for 2000 h in the rig presented in **Figure 3**, kinetic data were obtained via standard weight method, and kinetic results are shown in **Figure 11**.

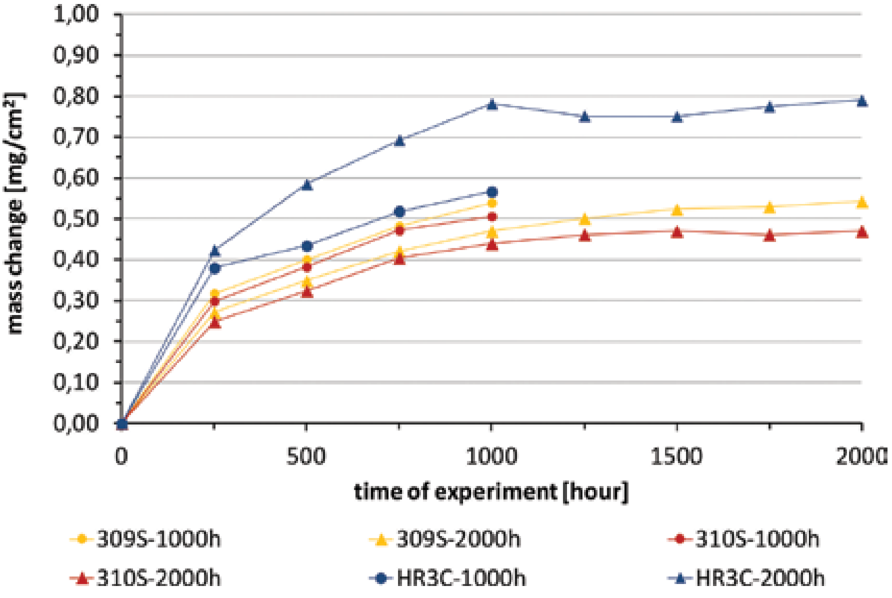

Figure 11. Kinetic data for 309S, 310S, and HR3C steels exposed to the steam oxidation regime at 800°C for 2000 h.

The steels showed a relatively low mass gain at 800°C. All the exposed materials showed similar mass change with difference of 0.05 mg/cm^2 after 2000 h of exposure, suggesting the same mechanism of corrosion behaviour. The highest mass gain was achieved for HR3C and the lowest for 310S steel even if the difference was not significant. The surface microstructures of highly alloyed steels exposed to steam conditions are shown in **Figure 12**. Chemically, 310S steel shows development of the oxide rich in Mn, Cr, and O with composition of 45, 22, 30 wt %, respectively, and some areas of the 310S steel surface was enriched in Mn with concentration of 50 and 40 wt%.

In general, in the steel 309S, developed morphology with high content of Mn, Cr, and Si oxide, some areas are enriched with Mn, O, and Fe with composition of 38, 19, 32 wt%, respectively. Therefore, both steels 310S and 309S developed similar morphologies under the steam oxidation, no cracks, spallation and other sign of corrosion degradation on the surface was observed, suggesting high adhesion of the oxide scale to the metallic substrate.

The HR3C showed similar surface structure as 309S and 310S, where rich in Cr, Mn and O phase developed, presenting appropriate corrosion performance at elevated temperature. The results shown here are in contrast with other findings that reports the minimum content of Cr promoting the formation of stable Cr_2O_3 in steam requires 20–25 wt%., Wasilewski, Robb, Giggins, and Pettit [30, 31]. On the other, the study performed by Birks and Rickret [32] suggests that if Cr reaches 10 wt%, then spinel $(Cr,Me)_3O_4$ should develop containing some quantity of Fe, Mn, Mo (alloying elements), the authors suggested that for the formation of thin, adherent, protective Cr_2O_3 20 wt% Cr is requires 20 wt% or more.

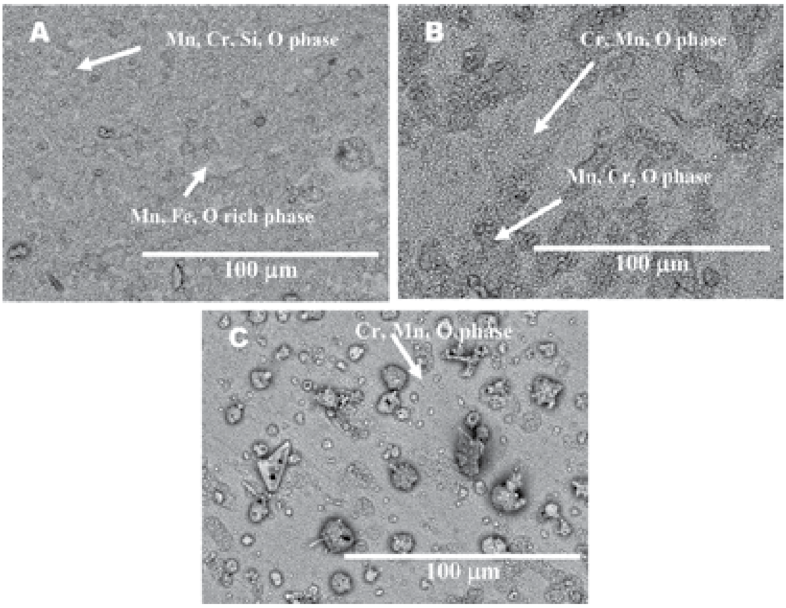

Figure 12. Surface morphologies of: (A) 309S, (B) 310S, (C) HR3C after exposure at 800°C for 2000 h in a steam atmosphere.

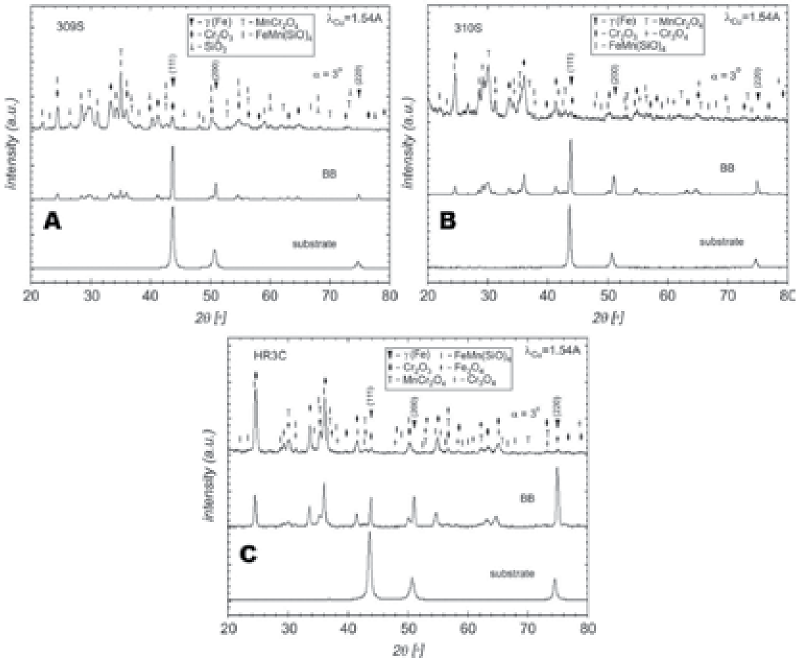

Figure 13. XRD pattern of (A) 309S, (B) 310S, (C) HR3C after exposure at 800°C for 2000 h in a steam atmosphere.

The current study shows that in a steam atmosphere, concentration of 23–25 wt% Cr is unable to promote the formation of pure Cr_2O_3, whenever highly alloyed steel is exposed at high temperatures, the formed oxide scale (Cr_2O_3) contain alloying elements, diffused from the bulk steel. Hence, it is impossible to develop Cr_2O_3 exclusively when the steel contains 20 wt% or even more Cr. The study shows that under 800°C, element activity, chemical potential, diffusion coefficient of Mn, Fe, Si are high enough to contribute in the scale formation; therefore, always some quantity of alloying elements will be observed, and hence the formation of exclusively pure Cr_2O_3 should be treated more as myth than the real finding.

In order to confirm the findings, **Figure 13A–C** shows XRD patterns for highly alloyed steels under the steam oxidation conditions.

5. Metal loss of steels in steam atmosphere

Following the steam oxidation exposures at high temperatures, the exposed samples were cold mounted to protect the potentially delicate oxide scale. The polished cross sections were measured using an image analyser to generate accurate measurements of the amount of metal remaining after the steam oxidation tests. **Figure 14** shows a schematic on the x-y stage for the analysis.

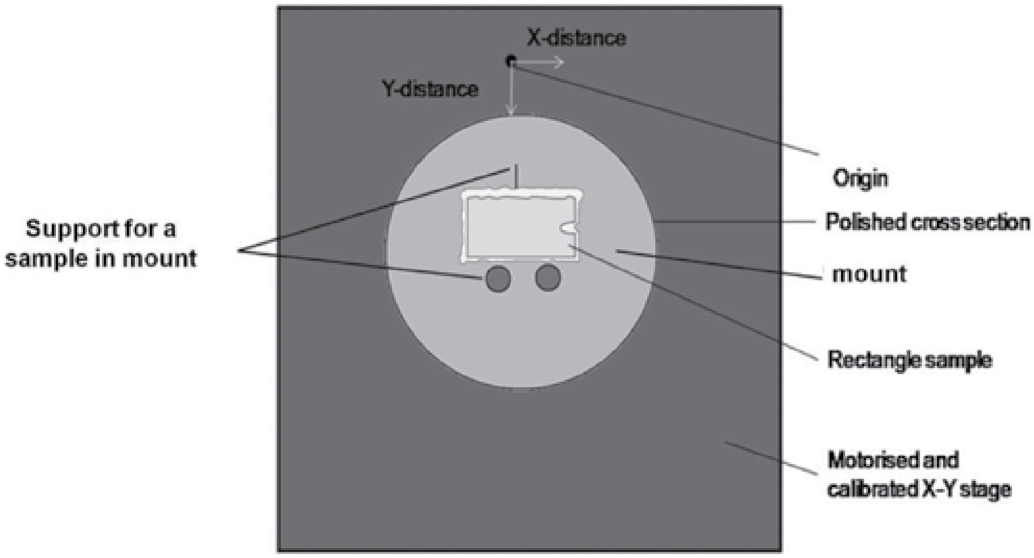

Figure 14. Schematic of a rectangular samples cross-section on the digital image analyser stage.

The best results of metal loss analyses were assessed when ~55 or more points around the sample was captured. The images were recorded during measurement and stitched together. The obvious metal losses in each of these images were pinpointed. **Figure 15** demonstrates the function of image analyser (e.g., at point B the x value = $b2$ and the y value = $a2$).

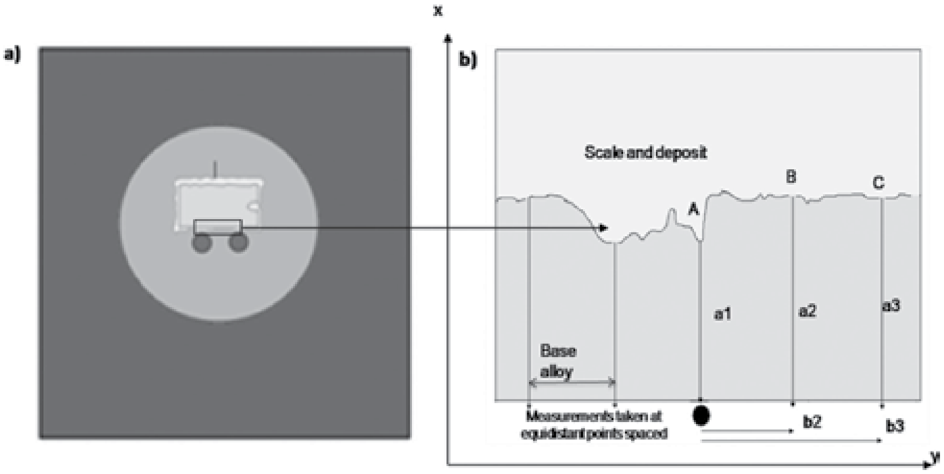

Figure 15. Illustration of function of image analyser (a) stage and sample; (b) determining metal loss from the images recorded.

Figure 16A–D compares metal loss between ferritic steels with low Cr content, whereas metal loss data for ferritic martensitic, and mid alloyed steels exposed to the steam oxidation environment is shown in **Figure 17** compares metal loss between ferritic, ferritic martensitic, and highly alloyed steels exposed to the steam oxidation environment. It was found that the steel with W addition presented lower metal loss compared to the T22. Therefore, it is confirmed that addition of small quantity of W improves high-temperature corrosion resistance. Metal loss of ferritic-martensitic steel reveals reverse situation, the steel with W addition shown a slightly higher metal loss than that offered by T91 steel. However, these findings are in good agreement with the published data [10]. The steel with 12 wt% Cr showed much higher metal loss than that observed in 16 wt% Cr steel, whereas a lower loss was observed in the low-alloyed steels and ferritic martensitic steels under the steam oxidation conditions. Furthermore, the steel with 12 wt% showed a higher spread in terms of metal loss calculations; the lowest metal loss data was achieved at 700 and 750°C for 2000 h of exposure where metal loss reached 80 μm. At the highest temperature, the metal loss value doubled. The steel with 16 wt% Cr showed as little as 15-μm value of metal loss in temperature range 700–800°C after 2000 h of exposure. The steel with 16 wt% Cr (316L) indicated much better corrosion resistance in a steam atmosphere than that offered by E1250 steel (12 wt% Cr). The calculated values of the metal loss, showed narrower data set as shown in the 12 wt% Cr steel. The behaviour suggests much better corrosion resistance at an elevated temperature. Furthermore, the majority of the metal loss results are accumulated in blue region indicating via thin blue stripe in **Figure 16D**. The calculations for 12 wt% Cr steel were not performed for 500–1500 h at 700 and 750°C, respectively, due to metal loss lower than 5 μm in terms of cumulative probability [%]. The values lower than 5 μm are hard to evaluate furthermore such calculations are cursed with high error probability. Similarly, metal loss calculations for 347HFG, 309S, 310S, and HR3C were not estimated due to the metal loss value lower than 5 μm.

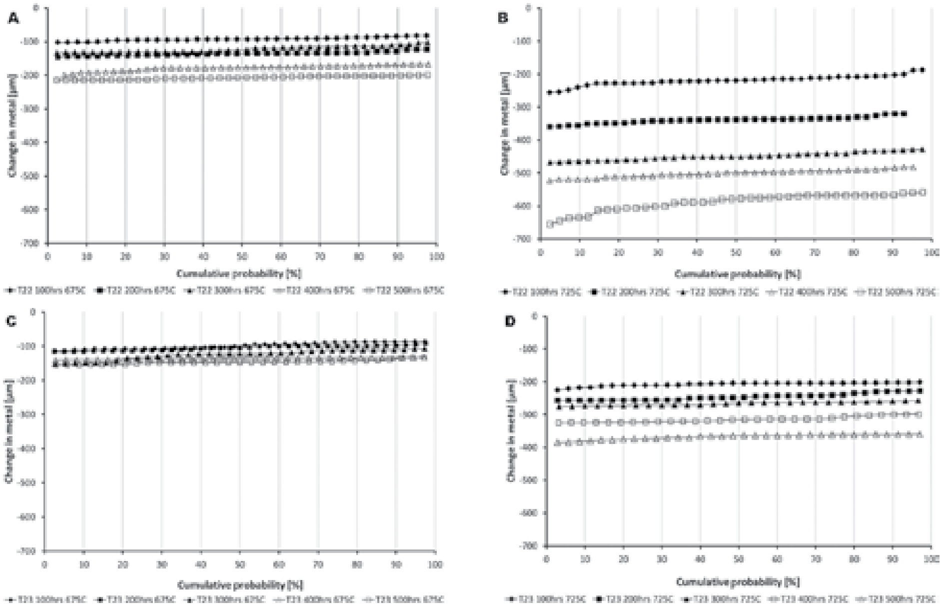

Figure 16. Metal versus metal loss data of T22 (A, B) and T23 ferritic steel (C and D) after exposure at 675 and 725°C in a steam atmosphere.

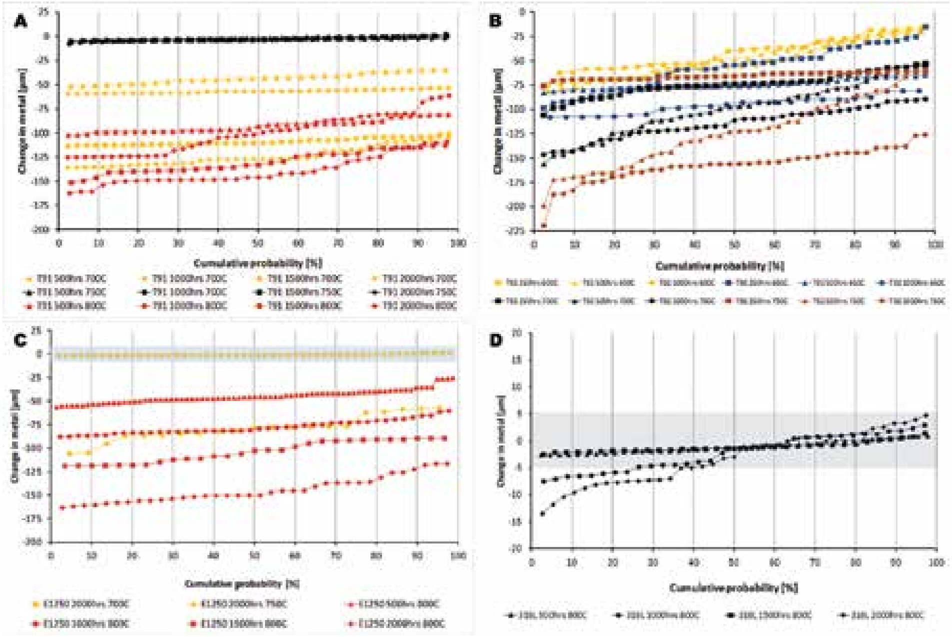

Figure 17. Metal loss data (A) T91, (B) T92, (C) E1250, and (D) 316L steels at elevated temperatures exposed in a steam atmosphere.

6. Conclusions

The aim of this chapter was to present the latest results of the steam oxidation work performed in unique close-loop system under high temperatures. In this study, nine steels with different chemical compositions were exposed. The steels represent ferritic, ferritic-martensitic, and austenitic grades. The tests were carried out in close loop and the steam oxidation system at different temperatures ranging 600–800°C. Based on the results, the following conclusions are drawn and it can be concluded that ferritic steels such as T22 and T23 form thick oxide scales, indicating the formation of all three Fe-based oxides at temperatures above 570°C. The oxide scales above 650°C show voids formation between two Fe_2O_3 and Fe_3O_4 layers in ferritic materials; however, addition of small portion of W (up to 3 wt%) to T23 steel delivers enhancement in corrosion and resistance in pure a steam atmosphere compared to T22 steel. Calculated metal loss for ferritic steel reached almost 650 μm at 725°C. Nevertheless, the formed oxide scale show good adherence to the substrate, and lack spallation was observed. The steel with 9 wt % Cr T91, T92 in comparison to T22, T23 steels showed a slightly better corrosion resistance as expected. However, at 750°C, "bell shape" temperature dependence in ferritic martensitic steels was found. Finally, addition of small portion of W to 9 wt% Cr steel showed adverse effect than that found in 3 wt% Cr steel (T22). The steel with 12 wt% Cr (E1250) showed formation of flaky, poor adherent scale, and the scale spallation was observed mainly for concave geometry; however, much lower mass gain was observed than that found in ferritic steels. The steel with higher content of Cr (16 wt% Cr, 316L steel) showed better corrosion resistance than that offered by 12 wt% Cr steel; however, at 800°C, test for 2000 h of exposure accelerated degradation was observed due to rich Fe nodule formation. The steels with 17 and 18 wt% Cr showed again better corrosion resistance than that offered by 12 and 16 wt% Cr steel; lower number of nodules and chromium-rich oxide was found on the surface in 18 wt% Cr steel. In comparison to ferritic steels, metal loss calculation in austenitic steels showed that only steel with 12 wt% Cr indicates more than 5 μm metal loss, whereas other materials showed metal loss lesser than 5 μm, even after 2000 h of exposure. High-alloyed steels, such as HR3C, (25 wt% Cr) 310S, 309S (>22 wt% Cr), showed the formation of protective scales and Cr_2O_3, Cr_3O_4, $MnCr_2O_4$ phases, and lack of spallation occurred.

Author details

T. Dudziak

Address all correspondence to: tomasz.dudziak@iod.krakow.pl

Foundry Research Institute, Centre for High Temperature Studies, Zakopiańska, Kraków, Poland

References

[1] EIA International Energy Statistics. Coal: Recoverable Reserves, (2012)

[2] How much carbon dioxide is produced when different fuels are burned? US EIA

[3] S. J. Davis, R. H. Socolow, Commitment accounting of CO2 emissions, Environmental Research Letters, 9 (8), (2014)

[4] Annual Energy Outlook 2010 with Projections to 2035, Department of Energy DOE/ EIA-0383 (2010)

[5] International Energy Agency (IEA), Energy Efficiency Indicators for Public Electricity Production from Fossil Fuels, IEA Information paper (2008)

[6] I. Traynor and D. Gow, EU promises 20% reduction in carbon emissions by 2020, The Guardian Newspaper (2007)

[7] T. U. Kern, K. Weighthardt, H. Kirchner, Material and design solutions for advanced steam power plants Proceedings of the Fourth International Conference on Advances in Materials Technology for Fossil Power Plants. Hilton Head Island, USA (2004)

[8] I. Wright, R. Dooley, A review of the oxidation behaviour of structural alloys in steam, Oak Ridge National Laboratory, Institute of Materials, Minerals and Mining and ASM International, Published by Maney for the Institute and ASM International (2010)

[9] J. Henry, G. Zhou, T. Ward, Lessons from the past: materials-related issues in an ultra-supercritical boiler at Eddystone plant, Materials at High Temperatures, 24 (2007), 249-258

[10] M. Lukaszewicz, N. J. Simms, T. Dudziak, J. R. Nicholls, Effect of steam flow rate and sample orientation on steam oxidation of ferritic and austenitic steels at 650 and 700°C, Oxidation of Metals, 79(5-6), (2013), 473-483

[11] T. Dudziak, High temperature performance of materials for the energy sector exposed to water steam, Transactions of Foundry Research Institute, 54(3), (2014), 43-58.

[12] Program on Technology Innovation: Oxide Growth and Exfoliation on Alloys Exposed to Steam, Electric Power Research Institute (EPRI), Final Report, (2007)

[13] G. Granaud, R. A. Rapp, Thickness of the oxide layers formed during the oxidation of iron. Oxidation of Metals. 1977; 11:193-198

[14] Reddy KPR, Cooper AR. Oxygen diffusion in MgO and a-Fe2O3. Journal of the American Ceramic Society. 66, (1983);664-666

[15] W. Wegener, G. Borchardt, Analysis of oxygen-18 tracer profiles in two-stage oxidation experiments (I): predominant oxygen diffusion in the growing scale. Oxidation of Metals, 36, (1991), 339-357

[16] W. Quadakkers, Mechanisms of steam oxidation in high strength martensitic steels, International Journal of Pressure Vessels and Piping. 84 (2007), 75

[17] Jei-Pil Wangc, Dong-Won Lee, Jung-Yeul Yun, Shun-Myung Shina, In-Soo Kim, Study on the Reduction of Forging Oxide Scale using Hydrogen, Journal of Korean Powder Metallurgy Institute 20(3), (2012), 174-179

[18] Y. Limoge, J. L. Bocquet, Self diffusion and point defects in iron oxides: FeO, Fe3O4, a-Fe2O3, Defects and Diffusion Forum, 194-199, (2001), 1051-1056

[19] S. R. Paterson, R. S. Moser and T. W. Rettig, "Interaction of Iron Based Materials with Water and Steam - Oxidation of Boiler Tubing", 1992 Paper 8.

[20] A Fry, S Osgerby, M Wright, Oxidation of Alloys in Steam Environments - A Review, National Physical Laboratory, (NPL) Report NPL Materials Centre (2002)

[21] K. Rodak, A. Hernas, A. Kielbus, Characteristics of new low-alloy steel T23 for power industry, 10th Jubilee International Scientific Conference, Achievements in Mechanical and Materials Engineering, Conference Proceedings, 483-486

[22] V. Lepingle, G. Louis, D. Petelot, B. Lefebvre and J.C. Vaillant, "High Temperature Corrosion Behaviour of Some Boiler Steels in Pure Water Vapour." High Temperature Corrosion and Protection of Materials 5, Materials Science Forum, 369-372, Trans Tech Publications, Switzerland, (2001), 239-246

[23] T. Dudziak, S. Grobauer, N. Simms, U. Krupp, M. Lukaszewicz, Metal loss of steam-oxidized alloys after exposures at 675°C and 725°C for 500 hours, High Temperature Materials and Processes, (2015), 1-16

[24] J. Ellis,M. Haw, Chromium Carbides, Materials World 5 (11):1(1997), 36

[25] R. Viswanathan, J. Server, R. Viswanathan, J. Server, Boiler materials for USC coal power plants-streamside oxidation, Journal of Materials Engineering and Performance, (2006), 15, 225-274.

[26] R. Chen, W. Yuen, Oxide-scale structures formed on commercial hot rolled steel strip and their formation mechanisms, Oxidation of Metals, 56, (2001), 89-118.

[27] F. Gesmundo, F. Viani, The formation of multilayer scales in the parabolic oxidation of pure metals: II Temperature and pressure dependence of the different rate constants, Corrosion Science, (1978), 18, 231-243.

[28] T. Dudziak, M. Lukaszewicz, N. Simms, J. Nicholls, Analysis of high temperature steam oxidation of superheater steels used in coal fired boilers, Oxidation of Metals, (2015), 1-17, DOI 10.1007/s11085-015-9593-9.

[29] S.R.J. Saunders 1, M. Monteiro, F. Rizzo, The oxidation behaviour of metals and alloys at high temperatures in atmospheres containing water vapour: A review Progress in Materials Science 53 (2008) 775-837

[30] G. E. Wasielewski, R. A. Rapp, High Temperature Oxidation, in "The Superalloys", edited by C.S. Sims and W. Hagel, John Wiley & Sons, Inc., (1972), 287-317.

[31] G. S. Giggins, F. S. Pettit, Oxidation of Ni-Cr-Al alloys between 1000 and 1200 oC, Journal Electrochemical Society, 118, (1971), 1782.

[32] N. Birks, H. Rickert, Development of scales in oxidation conditions in 30, 60, 80 wt% Cr Ni-Cr alloys, Journal of the Institute of Metals, 91, (1962-1963), 308.

Hot Corrosion of Weldments

M. Arivarasu, K. Gokulkumar,
K. Devendranath Ramkumar and N. Arivazhagan

Additional information is available at the end of the chapter

http://dx.doi.org/10.5772/63997

Abstract

Hot corrosion of the weldment is the result of the reaction between oxidation and sulfidation, which affects welded joints exposed to combustion gases containing sulfate coal ash at high temperature. It is also demonstrated that welding processes, weld consumables, temperature of exposure, and mixture of salt environment are important factors in hot corrosion of the weldment.

Hot corrosion is the main failure mode of welded components in the hot sections of gas turbines, boilers, metallurgical furnaces, and petrochemical installations. In this regard, the cyclic heating and cooling can mainly influence the corrosion behavior due to possible thermal stress on the weldment and their corrosion products. Hence, the maximum service temperatures of welded joints are decreased when exposed to hot corrosion environments.

Keywords: molten salt, air oxidation, weldment corrosion, dissimilar weldments, cyclic corrosion

1. Introduction

Joints of similar or dissimilar metals are used widely in various industrial applications owing to both technical and economic benefits. The production of high-quality welds with a high degree of consistency is achievable for the application in ambient conditions. However, the complexity arose while joining dissimilar metals, including the solidification cracking, microfissuring, and liquation cracking at the weld zone and heat-affected zone (HAZ) due to the differences in the coefficient of thermal expansion and chemical composition. Although there are numerous applications in which similar/dissimilar welds are employed, the current discussion on this chapter is limited to high-temperature corrosion in power generation/high-temperature turbine environments.

Most of the failure analyses have shown that failure was experienced in the weld zone since it is generally inferior to its counterpart. The composition, morphology, and the secondary precipitates in the weldment undergo undesirable transformations in the aggressive high-temperature environments. Most of the research on high-temperature corrosion has been directed toward the correlation of the in-service failures of the weld joints to the microstructural degradation caused during welding. However, in recent years, systematic investigations in the laboratory setup report influence of welding processes, welding consumables, and different environments on hot corrosion behavior of weldments at the elevated temperatures.

Hot corrosion of the weldment is the result of reaction between oxidation and sulfidation which affects welded joints exposed to combustion gases containing sulfate coal ash at high temperature [1, 2]. It is also demonstrated that welding processes, weld consumables, temperature of exposure, and mixture of salt environment are important factors in hot corrosion of the weldment.

Failure of welded components in the hot sections of gas turbines, boilers, metallurgical furnaces, and petrochemical installations primarily occur due to hot corrosion [3, 4]. In this regard, the cyclic heating and cooling can have a huge influence on the corrosion behavior due to possible thermal stress on the weldment and their corrosion products. Hence, when exposed to aggressive corrosion environments, it is preferred that the maximum service temperatures of welded joints are decreased.

The deposition of K_2SO_4, Na_2SO_4, V_2O_5, NaCl, and KCl in many components in power plants is potentially harmful with regard to hot corrosion since these salts are the primary constituents of hot corrosion. Further, the deposition of chloride-rich salts on these components is considered detrimental, causing accelerated corrosion in the weld joints [5–9]. Internal oxidation/localized selective leaching in the weldment can particularly deteriorate the creep and fatigue lives of alloys due to phenomenon such as crack initiation at the grain boundaries.

In general, the service temperatures range between 400 and 650°C in typical superheater tubes, and the salt deposition converts to its molten phases. Nielsen et al. [8] have reported that the highest service temperature of weld joints was below 600°C. It is cost-effective, and hence it is necessary to improve the corrosion resistance of the weld by means of different welding techniques and filler wires for the future power plants.

The effect of hot corrosion becomes more aggressive at 600°C, due to the formation of low-melting alkali sulfates, which are eutectic mixtures, resulting in high sulfidation tendencies [10–15]. This tendency decreases when the operating temperatures are higher than 800°C, due to the reduced stability of the sulfate compounds at these temperatures [16–19].

In general, hot corrosion of the welded joints is more severe, due to the various metallurgical changes during the welding process and also due to the existence of a potential gradient along the weldment. These changes, although, will not have any deteriorating effect on the structural applications. However, there will be a huge impact on the corrosion resistance behavior of welded joints, which mandates the evaluation of such components for their corrosion properties. In addition to the metallurgical effects, temperature of service and salt environment plays an important role in the corrosion resistance of the welded joints.

2. Effect of welding process

The amount of heat generated and their heat-transfer efficiency to the material to be welded were found to be different for various welding processes. The heat input supplied to the materials plays an important role in altering the metallurgical structures. More the heat input, wider the heat-affected zone (HAZ) and phase changes in the weld zone. The higher the welding speed, higher will be the temperature gradient, and hence less time for metallurgical changes. Similarly, current pulsing reduces the heat input during welding. In pulsed current welding processes, heat is supplied to the material only during the peak ON time, and during the peak OFF time, a meager amount of power is supplied just to maintain the arc, but not to extinguish. This results in sufficient time for the weldment to cool intermittently, thereby facilitating nucleation resulting in refined grains.

The effects of welding processes, the exposed environments, and temperature on weld corrosion behavior were investigated by Arivazhagan et al. [20, 21]. The authors studied the cyclic hot corrosion behavior of dissimilar weldments of AISI 4140 and AISI 304 made by friction welding (FRW), gas tungsten arc welding (GTAW), and electron beam welding (EBW). Studies were carried out with and without the salt mixtures of Na_2SO_4 + V_2O_5 (60%), Na_2SO_4 + NaCl (50%), K_2SO_4 + NaCl (60%), and Na_2SO_4 (40%) + K_2SO_4 (40%) + NaCl (10%) + KCl (10%) in the temperature range from 500 to 900°C under cyclic conditions. The typical macrograph of hot corroded dissimilar weldment in the molten salt environment is represented in **Figure 1**. The weight loss during each cycle is measured to evaluate the corrosion rate and kinetics.

Figure 1. Macrographs of FSW (a), EBW (b), and GTA (c) welded AISI 4140 and AISI 304 subjected to molten salt environment at 600°C.

The kinetics of hot corrosion with molten salt mixtures shows higher growth rate of scale formation, which is much more severe under hot corrosion than with simple air oxidation. Although hot corrosion of the weldments is found to be in an accelerated manner in the molten salts, the salt composition plays an important role. In all the environments, the scales formed on the weldment were found to be oxides of Fe, Cr, and Ni and observed to be fragile and had a tendency for spalling. The reason for the same could be attributed to the below-mentioned factors:

- **(a)** Coefficient of thermal expansion differs for each base metal, weld, and the scale, which generates the stress.
- **(b)** Stresses are generated during cooling, which may affect the adhesion property of the scale.
- **(c)** Severe strain is developed due to the precipitation of oxides from the liquid phase and interdiffusion of intermediate layers of these oxides.
- **(d)** Formation of scale within the growing scale as a result of two-way flow of the corrosive elements. Example: reactants, such as oxygen, diffuse to the inner region, while the diffusion of chromium from base metal is outward.

The study accounts for the influence of different welding processes, environments, and temperatures on the corrosion behavior of the dissimilar weldments (**Figure 2**).

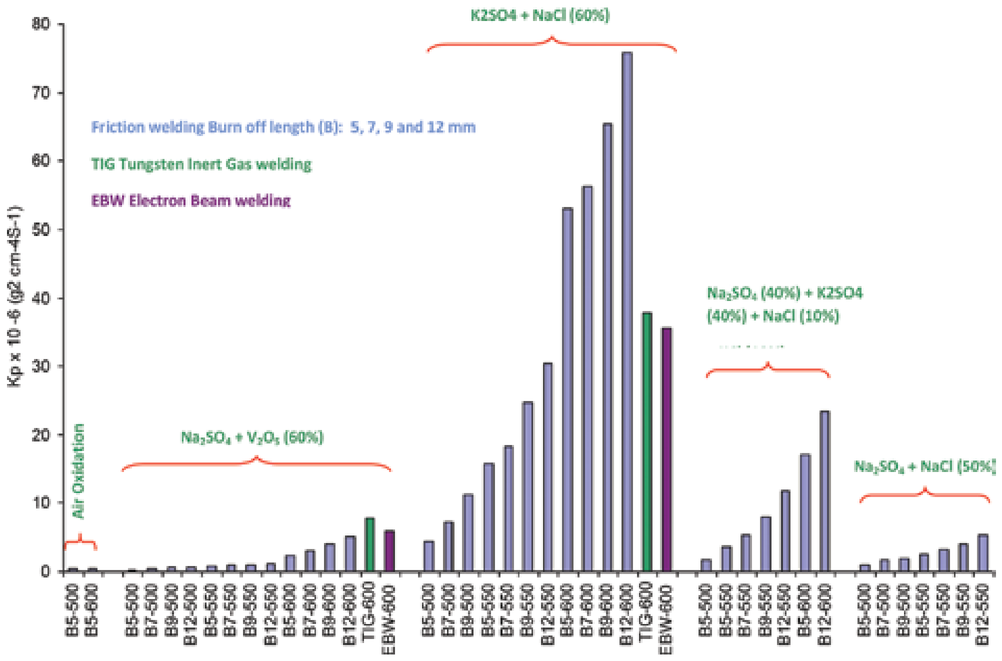

Figure 2. Bar charts showing parabolic rate constant K_p [$10^{-6}(g^2/cm^4/s^1)$] for dissimilar weldment subjected to cyclic oxidation in air and at molten salt environment for 50 cycles.

Irrespective of the temperature of testing or the salt composition, the oxidation rates and the overall weight gains for the investigated dissimilar weldments could be arranged in the following order, namely GTAW > EBW > FRW.

Further, the weld zone of dissimilar joints made by GTAW and EBW is more prone to corrosion due to the heterogeneous microstructure as compared to FRW. This phenomenon is the result of the continuous spalling of the scale from the weld zone due to the damage occurring in the protective oxide layer, which provides path for the corrosive gases to reach the base material and thus allows significant grain boundary corrosion [22, 23].

From the bar charts, it can be inferred that the friction-welded dissimilar metals have shown low corrosion resistance against the given molten salt environments as compared to that against the air under cyclic conditions. The maximum weight gain in Na_2SO_4 + V_2O_5 (60%) environment at 600°C is 50 times higher than that of the one exposed to air under cyclic conditions, whereas, it is of 190 times in the environment of K_2SO_4 + NaCl (60%). In the case of Na_2SO_4 (40%) + K_2SO_4 (40%) + NaCl (10%) + KCl (10%), the weight gain is around 100 times as compared to the weldment exposed to air, whereas it is around 50 times in the environment of Na_2SO_4 + NaCl (50%). XRD diffractograms and EDS analysis have indicated the phases formed identical to those formed during oxidation in molten salt in almost all the corroded samples. At 700 and 900°C, higher corrosion rates were observed due to the rapid reaction of molten salt when the friction-welded dissimilar weldments are exposed to the Na_2SO_4 + V_2O_5 (60%) environment.

The weight gain after 50 cycles of hot corrosion studies in all the environments could be arranged in the following order:

K_2SO_4 + NaCl (60%) > Na_2SO_4 (40%) + K_2SO_4 (40%) + NaCl (10%) + KCl (10%) > Na_2SO_4 + V_2O_5 (60%) > Na2SO4 + NaCl (50%) > Air

The weight gain of weldment made by EBW and GTAW exposed to Na_2SO_4 + V_2O_5 (60%) is around 1.5 times higher than that of the weight gain of weldment made by FRW. The weight gain of weldment made by FRW exposed to K_2SO_4 + NaCl (60%) is around 1.2 times higher than that of the weight gain of the weldment made by EBW and GTAW. It shows that the environment of K_2SO_4 + NaCl (60%) is more aggressive for the weldment made by FRW as compared to the one made by EBW and TIG. Also, from the investigation, it was observed that the weight gain for the weldment made by EBW and TIG, exposed to K_2SO_4 + NaCl (60%), is around two times higher than that of the weldment exposed to Na_2SO_4 + V_2O_5 (60%).

From the overall analysis of exposed samples in the three environments of study, the of scales formed on the weldments are identified as oxides of iron and chromium by X-ray diffract grams and is confirmed by the EDS analysis. From the EDS data, the scale on the weld zone of EBW and GTAW weldments contains higher amount of Cr_2O_3 and NiO, which is also higher as compared to that of friction weldment when exposed under K_2SO_4 + NaCl (60%) at 600°C. It can be inferred from this that EBW and GTAW weldments have provided maximum resistance to corrosion as compared to the friction weldment in the above-said environment. This may be attributed to the fast formation of a continuous chromia scale on the weld zone due to the easy diffusion of Cr and Ni toward the weld zone from the sides of alloy 304. The EDS elemental analysis for most of the cases indicated the higher content of Fe_2O_3 and Cr_2O_3 on the scale over weldment, which may be due to the enrichment of this zone with Fe and Cr (**Figure 3**).

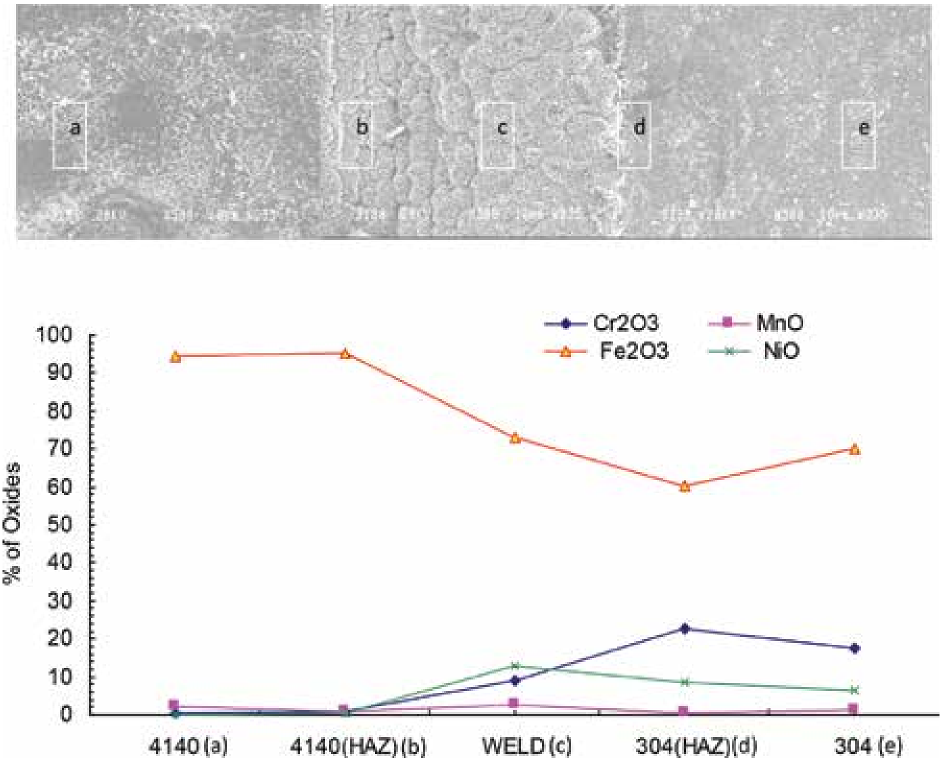

Figure 3. SEM/EDAX graph shows the friction weldment exposed at 600°C under molten salt environment after 50 cycles.

Arivarasu et al. [24] investigated the hot corrosion behavior of low-alloy steel AISI 4340 and austenitic stainless steel AISI 304L. Dissimilar weldment joined by continuous current gas tungsten arc welding (CCGTAW) and pulsed current (PCGTAW) gas tungsten arc welding (GTAW) techniques, using filler metals ER309L, ERNiCr-3, and also in autogenous process, was investigated.

In this study, the oxychlorination of these joints at 600°C in eutectic mixture of K_2SO_4 + 60% NaCl molten salt environment was investigated. In the weld and in the interfaces employing samples welded with pulsed current, the reaction of molten salt was higher than that of the CCGTAW process. Two reasons could be attributed to this behavior: first, the microstructure showed fragmented delta ferrites (**Figure 4**) at numerous locations of the weld zone in the pulsed mode, resulting in the formation of micro-electrochemical cells, which act as sites for corrosion initiation, leading to higher corrosion rate. Second, the ferrite content in the pulsed current is higher than that in the continuous current mode, as represented in **Table 1**. At temperatures around 600°C, ferrite will decompose into σ-phase precipitates + austenite. This σ-phase results in the removal of Cr from the solid solution, resulting in the deterioration of the corrosion resistance of the austenitic stainless steel, which is in accordance with the literature [25–27].

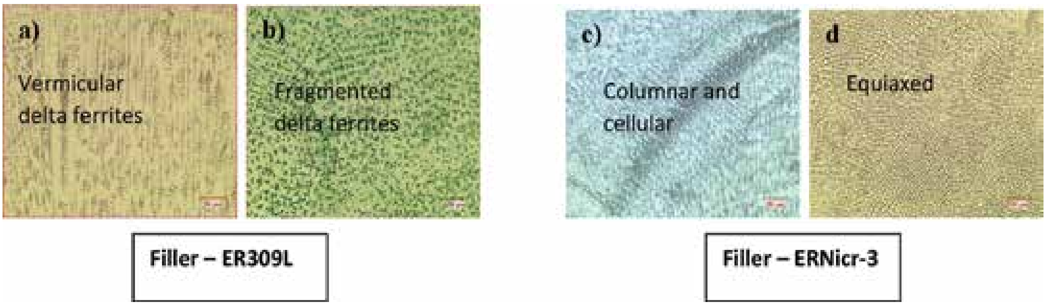

Figure 4. Microstructural variations in (a) CCGTA–ER309L, (b) PCGTA–ER309L, (c) CCGTA–ERNiCr-3, and (d) PCGTA–ERNiCr-3.

	Process	CCGTAW	PCGTAW
1	CAP	2.8	4.2
2	Root	0.65	2.6

Table 1. Average ferrite analysis in the weld zone of ER309L.

Thermogravimetric plots (**Figure 5a**) show that higher weight gain of 6.65 mg/cm^2 (217%) is observed in dissimilar joint fabricated by PCGTA welding processes as compared to the CCGTAW processes, in which is 1.71 mg/cm^2. Also, the corrosion rate K_p for the continuous current technique (0.133×10^{-7} g^2/cm^4/s) is less than that of the pulsed current technique (1.74×10^{-7} g^2/cm^4/s), which signifies that the corrosion resistance of CCGTAW is better than that of the PCGTA technique. The cumulative weight gain (**Figure 5b**) of CCGTAW process when employing ERNiCr-3 filler is 6.07 mg/cm^2 (91%) higher than that of the PCGTA process (1.71 mg/cm^2), suggesting that pulsed current mode is better corrosion-resistant than the continuous mode. The corrosion rate for CCGAW is 2.68 times higher than that of the PCGTA–ERNiCr-3 weldments (**Figure 5c**). The presence of fine equiaxed grains (**Figure 4c**, **d**) obtained by employing the pulsed current mode, when compared to the columnar dendrites in the continuous current mode, is attributed to the higher corrosion resistance of the pulsed mode [28, 29]. It was also reported that the fine-grained equiaxed microstructural solidification would improve the corrosion resistance than a coarse-grained microstructure.

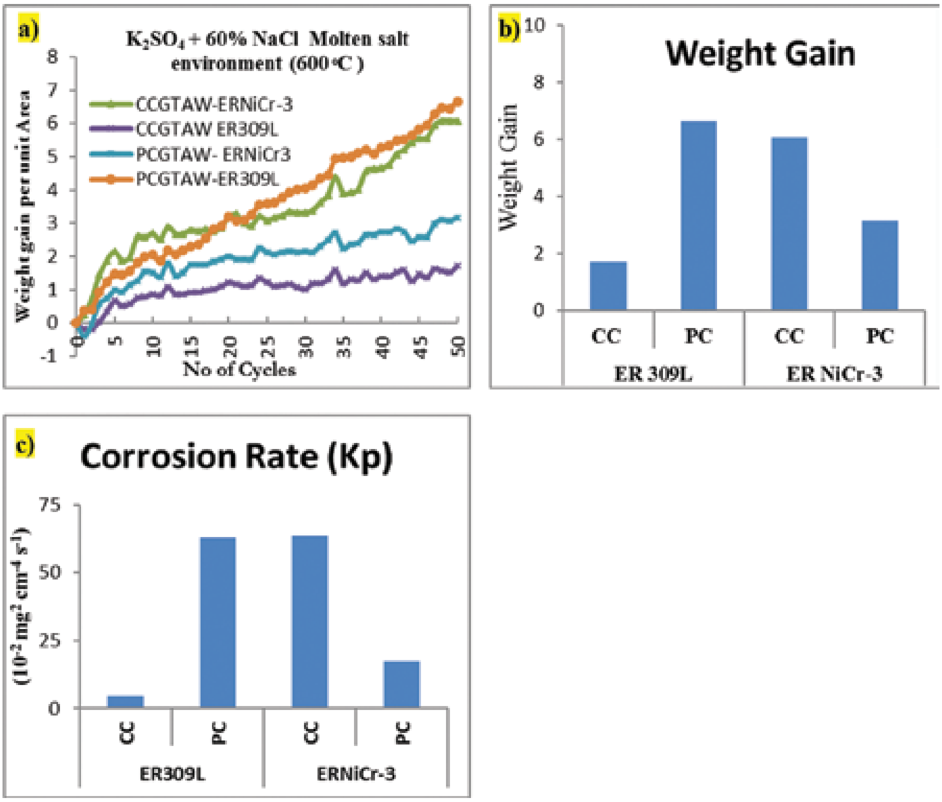

Figure 5. Analysis of hot corroded dissimilar AISI 4340 and AISI 304, showing (a) thermogravimentric, (b) chart weight gain, and (c) corrosion rate.

3. Effect of filler wire

One of the most important issues in the case of weld joints is the selection of proper filler materials. If the selection of filler wire is not appropriate, some weld defects such as fusion zone segregation, secondary phase formation, and dilutions deteriorate the corrosion behavior of the weld drastically. Furthermore, if the filler metal has lesser corrosion resistance than the parent metals, it would result in preferential corrosion attack on the weld metal. In general, overalloyed filler metals are used in the weldments to compensate for the loss of alloying elements by the welding fume and to protect the local area where there is less composition due to the segregation in the welds. A few parameters for the criteria of selection of filler metals include chemical composition, nearer corrosion potential in the galvanic series with respect to base metals, and additional alloying elements which improve corrosion resistance (e.g., addition of Ti/Ni in ER309L to eliminate chromium carbide precipitation, which subsequentially eliminates grain boundary corrosion/sensitization in elevated temperatures).

A matching filler wire gives a homogeneous nucleation/microstructure at the weld fusion zone, whereas an overmatching filler gives a heterogeneous nucleation/microstructure at various zones, leading to localized galvanized corrosion due to differences in the electrochemical potentials. The composition difference between the filler and base metal also influences the elemental migration during welding process. It is one of the major concerns, which affects the corrosion behavior of a weldment. Selection of filler metal and its dilution with the base metal also play a major role in the weldment's corrosion behavior, when exposed to the aggressive environments.

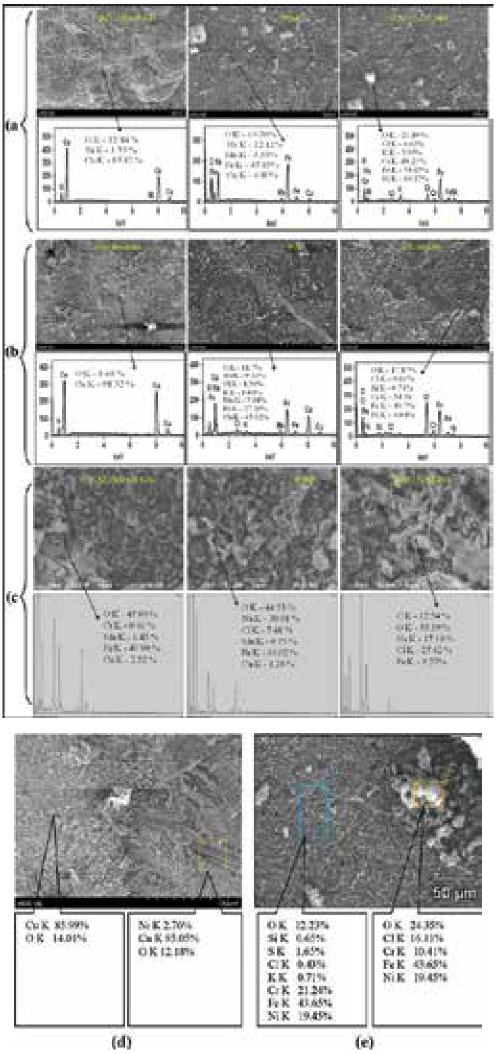

Figure 6. SEM/EDAX analysis of hot corroded GTA-welded dissimilar Monel 400 and AISI 304 (composite region) employing (a) E309L, (b) ENiCu-7, and (c) ENiCrFe-3 filler wires; (d) parent metal—Monel 400 and (e) parent metal—AISI 304 subjected to the molten salt environment of K_2SO_4 + 60% NaCl at 600°C.

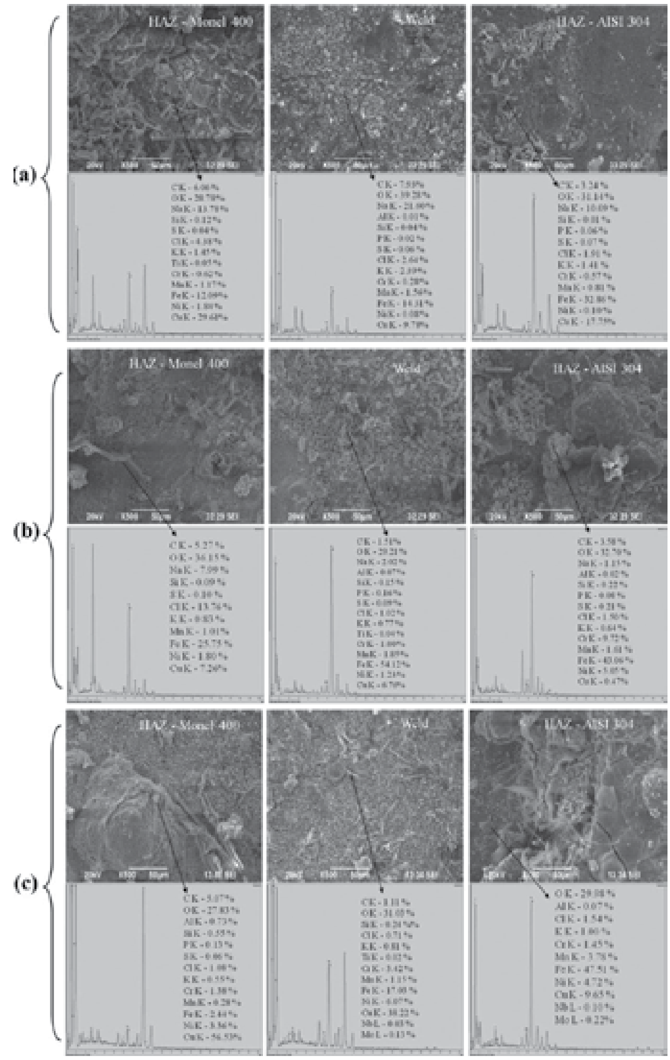

Figure 7. SEM/EDAX analysis of hot corroded PCGTA-welded dissimilar Monel 400 and AISI 304 (composite region) employing (a) E309L, (b) ENiCu-7, and (c) ENiCrFe-3 filler wires subjected to the molten sat environment of K_2SO_4 + 60% NaCl.

Devendranath et al. [30, 31] studied the effects of various filler wires (E309L, ENiCu-7, and ERNiCrFe-3) on the hot corrosion behavior of Monel 400 and AISI 304 dissimilar weldment subjected to cyclic air oxidation and a K_2SO_4 + NaCl (60%) molten salt environment at 600°C. The author investigated the dilution of different filler metals with base metals and the influence on weldment corrosion in the different environments. The authors reported that Fe and Cr are not completely soluble in the Ni–Cu alloy. The authors witnessed the formation of Fe-rich phases in the weld of Cu–Ni alloy and steel, which causes localized galvanic corrosion in the weld fusion zone [30]. Further, the author concluded that ENiCu-7 weld is found to be less reactive, as the enrichment of Ni in the weld zone improved the corrosion properties primarily resulting from the nickel oxide which makes the molten salt less active (**Figures 6** and **7**). The formation of chlorides of Fe and Cr was witnessed in both CCGTA and PCGTA ENiCrFe-3 weldments. These metallic chlorides are highly volatile, leaving behind pits and voids in the subsurface of the metal. In molten salt environments, especially in the chromium-depleted regions, the corrosion morphologies show large amounts of subscale attack. Chromium chloride ($CrCl_3$) converts into oxide at very low oxygen pressure, iron chloride at significantly higher oxygen pressure, and a much higher oxygen partial pressure is needed to convert nickel chloride into NiO, especially at low temperatures. This means that evaporating chromium chlorides are oxidized closer to the metal surface than iron and nickel chlorides. Active oxidation, involving transport of metal chlorides in the liquid salt phase, destroys the normally protective Cr_2O_3 scale. In an environment with NaCl deposits, adding aluminum to the alloy to generate a protective Al_2O_3 scale should be able to increase the high-temperature corrosion resistance in a chloride environment.

Gokulkumar et al. [32] investigated the corrosion products of continuous current gas tungsten arc (CCGTA) and pulsed current gas tungsten arc (PCGTA) welded dissimilar Inconel 625 and AISI 316 L using ERNiCrMo-3, ER2209, and ERNiCr-3 filler metals subjected to cyclic hot corrosion in air and K_2SO_4 + NaCl (60%) molten salt environment at 650°C.

The author has well established that the salt mixture of K_2SO_4 and NaCl concentrate on the protective layer and partially diffuse through the porous scale. It was observed that the corrosive elements, such as Na, K, and Cl, liquefied the protective oxide scale at 650°C, and hence protection of the weldment is deteriorated. It is due to the formation of corrosive species, such as chlorides and sulfides, and these products are not fully protective in nature.

It is also concluded that the weldments exposed to the mixture of K_2SO_4 and NaCl were prone to a more aggressive attack in terms of corrosion than that of air oxidation.

The weld fusion zone produced by super-alloy fillers such as ERNiCrMo-3 and ERNiCr-3 contains higher Cr and Ni content; therefore, on the basis of standard free energy of Ni and Cr, it is possible to form Cr-rich oxide scale on its surface at 650°C, which provides an adequate protectiveness.

ERNiCrMo-3 weldment was found to have higher corrosion resistance as compared to other filler wires. This could be due to the formation of a protective oxide layer containing Ni, Cr, and Mo, which is more intact and more adhesive in nature. But, in the case of ER2209 weldment, the scale had more pores, poor adhesion, and a spalling nature. The corrosive environment had penetrated deeply into the weld and the weld interface.

It is also inferred that the corrosion rate of the weldments was influenced not only directly by the synthetic fused salt chemistry but also by the relative amount of corrosion-resistant elements such as Cr, Ni, and Mo. It is also clearly recorded that the weldment produced by employing Ni-rich austenitic fillers containing substantial amounts of Ni, Cr, and Mo demonstrated higher corrosion resistance than the stainless steel filler wire (**Figure 8**).

From the investigation, among the welding processes, the welds produced by PCGTA welding technique by using ERNiCrMo-3 filler wire have shown better corrosion resistance than other

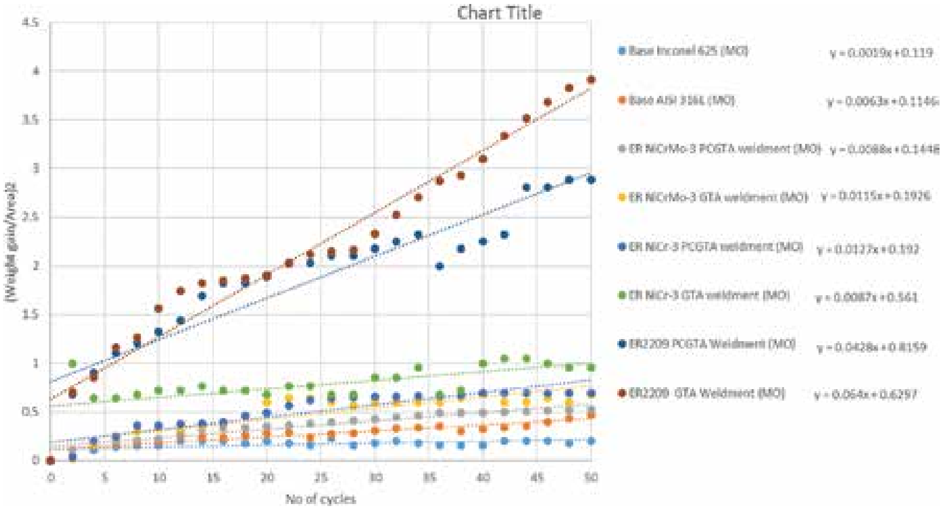

Figure 8. Thermogravimetric graph (weight gain/area)^2 of GTA and PCGTA weldment employing ERNiCrMo-3, ER2209, and ERNiCr-3 filler metals as well as base metals subjected to hot corrosion in the mixture of K_2SO_4 + NaC1 (60%) environment at 650°C.

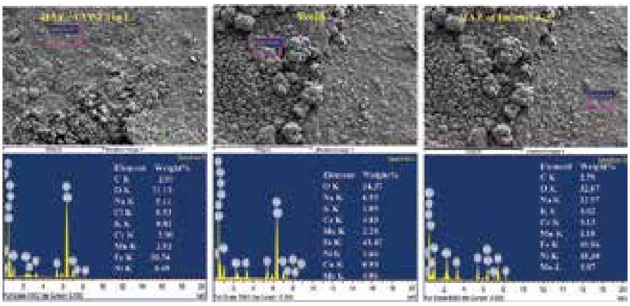

Figure 9. SEM/EDAX analysis of molten salt hot corroded dissimilar Inconel 625 and AISI 316 L weldment employing ER2209 filler metal.

filler wires. This can be inferred from the corrosion products determined by combining the SEM/EDS and the XRD that the scale contains Cr_2O_3 and Ni–Cr, Ni–Cr–Mo spinel oxides due to diffusion-controlled reaction. It is also observed from the investigation, among the filler wires, that the weldments produced by ERNiCr-3 and ERNiCrMo-3 fillers have shown higher resistance than ER2209 weldment (**Figure 9**).

Arivarasu et al. [24] investigated the effect of filler wires such as ER309L and ERNiCr-3 on hot corrosion behavior of low-alloy steel AISI 4340 and dissimilar weldment of austenitic stainless steel AISI 304L by employing CCGTAW and PCGTAW processes.

In the case of employing ER309L filler, the continuous current has better corrosion resistance than the pulsed current. The filler forms a considerable amount of ferrites for improved metallurgical aspects in terms of avoiding microfissuring during welding and has resulted in fragmented ferrites in the case of pulsed current than the vermicular ferrite in the continuous current technique.

Also, filler wire ERNiCr-3, which is an overmatching (nickel based) filler, employed to attain a better mechanical property has resulted in higher weight gain and corrosion rate than the ER309L filler employed in the continuous current mode. This is because it introduces additional zones of varying chemical composition, leading to increased electrochemical activity in the higher temperature than the one with ER309L filler, which has compatible composition with one of the base material E309L.

As per the literature, pulsed current is supposed to produce fine-grained structures, irrespective of the fillers employed and shall lead to better mechanical properties. But, from the experimental results stated above, it is evident that in terms of corrosion behavior, there shall not be a set thumb rule, and it is based on the compositional and microstructural variations that form during different processes. This shows that the filler metal and the process individually have the ability to alter the corrosion resistance of a weldment at higher temperature.

4. Recommendations

One of the key successes to improve weld corrosion resistance is the selection of suitable welding processes with reduced heat input and appropriate/matching composition of filler metal, resulting in fewer variations in the microstructures. The hot corrosion behavior of the weld could be improved by choosing welding techniques with lower heat input by employing high-alloy filler wire. Selecting appropriate welding consumables could reduce the dendritic and interdendritic segregations, which reduce the localized galvanic effects in turn to improve the corrosion behavior of the weld. A heat treatment can be an effective way to improve the corrosion resistance of the weld by avoiding residual stress, segregation, localized galvanic cell, and unwanted negative phases. Adopting an interpass heat treatment during welding could avoid the hydrogen cracking of the welded components in the service environment.

Finally, it is highly impossible to eliminate the high-temperature corrosion. However, this could be minimized by selecting suitable welding techniques, processes, parameters, and weld consumables.

Author details

M. Arivarasu, K. Gokulkumar, K. Devendranath Ramkumar and N. Arivazhagan*

*Address all correspondence to: narivazhagan@vit.ac.in

School of Mechanical Engineering, VIT University, Vellore, Tamil Nadu, India

References

[1] Lai, G.Y.: High-Temperature Corrosion of Engineering Alloys. Metals Park: American Society for Metals. 1990; 231 p.

[2] Shinata, Y., F. Takahashi and K. Hashiura: NaCl-induced hot corrosion of stainless steels. Mater Sci Eng. 1987;87:399–405. DOI:10.1016/0025-5416(87)90404-6

[3] Natesan, K.: High temperature corrosion in power generating systems. Internal Report, Argonne National Labs, IL, USA, 2002. http://www.ipd.anl.gov/anlpubs/2002/05/43234 [Accessed: 2016-04-07].

[4] Chawla, V.: Hot corrosion & erosion problems in coal based power plants in India and possible solutions–a review. J Miner Mater Charact Eng. 2011;10:367–375. DOI:10.4236/jmmce.2011.104027

[5] Saidur, R., E.A. Abdelaziz, A. Demirbas, M.S. Hossain and S. Mekhilef: A review on biomass as a fuel for boilers. Renew Sustain Energy. 2011;15:2262–2289. DOI:10.1016/j.rser.2011.02.015

[6] Yin, C., L.A. Rosendahl and S.K. Ker: Grate-firing of biomass for heat and power production. Prog Energy Combust Sci. 2008;34:725–754. DOI:10.1016/j.pecs.2008.05.002

[7] Demirbas, A.: Potential applications of renewable energy sources, biomass combustion problems in boiler power systems and combustion related environmental issues. Prog Energy Combust Sci. 2005;31:171–192. DOI:10.1016/j.pecs.2005.02.002

[8] Nielsen, H.P., F.J. Frandsen, K.D. Johansen and L.L. Baxter: The implication of chlorine-associated corrosion on the operation of biomass-fired boilers. Prog Energy Combust Sci. 2000;26:283–298. DOI:10.1016/S0360-1285(00)00003-4

[9] Michelsen, H.P., F. Frandsen, K.D. Johansen and O.H. Larsen: Deposition and high temperature corrosion in a 10 MW straw fired boiler. Fuel Process Technol. 1998;54:95–108. DOI:10.1016/S0378-3820(97)00062-3

[10] Pettit, F.: Hot corrosion of metals and alloys. Oxid Met. 2011;76:1–21. DOI:10.1007/s11085-011-9254-6

[11] Luthra, K.L. and D.A. Shores: Mechanism of Na_2SO_4 induced corrosion at 600–900°C. J Electrochem Soc. 1980;127:2202–2210. DOI:10.1149/1.2129375

[12] Lillerud, K.P. and P. Kofstad: Sulfate-induced hot corrosion of nickel. Oxid Met. 1984;21:233–270. DOI: 10.1007/BF00656835

[13] Kung, S.C.: Prediction of corrosion rate for alloys exposed to reducing/sulfidizing combustion gases. Mater Perform. 1997;36:36–40. NACE-97136.

[14] R.A. Rapp, Hot Corrosion by Fused Salts, In Encyclopedia of Materials: Science and Technology (Second Edition), edited by K.H. Jürgen Buschow, Robert W. Cahn, Merton C. Flemings, Bernhard Ilschner, Edward J. Kramer, Subhash Mahajan and Patrick

Veyssière, Elsevier, Oxford, 2001, Pages 3834-3835, ISBN 9780080431529, http://dx.doi.org/10.1016/B0-08-043152-6/00682-3. (http://www.sciencedirect.com/science/article/pii/B0080431526006823)

[15] Khanna, A.S.: Introduction to High Temperature Oxidation and Corrosion. Materials Park, OH: ASM International. 2002; pp 285–286.

[16] Hwan, B.S. and B.D. Lee: High temperature SO_2-gas corrosion of Ni–Cr–Co base superalloy between 800 and 1000°C. Defect Diffusion Forum. 2011;312:451–454.

[17] Zhao, S., X. Xie, G.D. Smith and S.J. Patel: The corrosion of Inconel alloy 740 in simulated environments for pulverized coal-fired boiler. Mater Chem. Phys. 2005;2:275–281. DOI: 10.1016/j.matchemphys.2004.04.006

[18] Kusabiraki, K., M. Morita, X.P. Guo and H. Anada: Hot corrosion of the Ni–20%Cr alloy and waspaloy immersed in Na_2SO_4. J Iron Steel Inst Jpn. 2007;93:498–505. DOI:10.1016/j.matchemphys.2004.04.006

[19] Lu, L.Y., T.J. Pan and Y. Niu: Oxidizing–sulfidizing corrosion of Ni–xCr–10 Al alloys at 700–800°C. Acta Metall Sin. 2011;47:1026–1031.

[20] Arivazhagan, N.: High Temperature Corrosion Studies on Welded Dissimilar Metals. PhD Thesis, IIT Roorkee, India, 2007.

[21] Arivazhagan, N., S. Narayanan, S. Surendra, P. Satya and G.M. Reddy: High temperature corrosion studies on friction welded low alloy steel and stainless steel in air and molten salt environment at 650°C. Mater Des. 2012;34:459–468. DOI:10.1016/j.matdes.2011.08.034

[22] Danyluk, S. and J.Y. Park: Corrosion and grain boundary penetration in type 316 stainless steel exposed to a coal gasification environment. Corrosion. 1979;35:575–576. DOI:10.5006/0010-9312-35.12.575

[23] Wang, D.: Corrosion behavior of chromized and/or aluminized 21/4cr-1mo steel in medium-btu coal gasifier environments. Surf Coat Technol. 1988;36:49–60. DOI: 10.1016/0257-8972(88)90135-1

[24] Arivarasu, M. Investigations on the Dissimilar Welds of AISI 4340 Low Alloy Steel and AISI 304l Austenitic Stainless Steel. PhD Thesis, VIT University, India, 2015.

[25] Karlsson, S., J. Pettersson, L.G. Johansson and J.E. Svensson: Alkali induced high temperature corrosion of stainless steel: The influence of NaCl, KCl and $CaCl_{2.}$ Oxid Met. 2012;78:83–102. DOI:10.1007/s11085-012-9293-7

[26] Guo, G.: The Corrosion and Mechanisms of Fe, Cr, Ni and Their Oxides in Molten Salts of NaCl and KCl. M.S. Thesis, Dalian University of Technology, Dalian, CN, 2005.

[27] Kim, J.K., Y.H. Kim, J.S. Lee and K.Y. Kim: Effect of chromium content on intergranular corrosion and precipitation of Ti-stabilized ferritic stainless steels. Corros Sci. 2010;52:1847–1852. DOI:10.1016/j.corsci.2010.01.037

[28] Ralston, K.D. and N. Birbilis: Effect of grain size on corrosion: A review. Corrosion. 2010;66:075005–075013.

[29] Haugsrud, R.: On the high-temperature oxidation of nickel. Corros Sci. 2003;45:211–235. DOI:10.1016/S0010-938X(02)00085-9

[30] Devendranath Ramkumar, K., N. Arivazhagan and S. Narayanan: Effect of filler materials on the performance of gas tungsten arc welded AISI 304 and Monel 400. Mater Des. 2012;40:70–79. DOI:10.1016/j.matdes.2012.03.024

[31] Devendranath Ramkumar, K., N. Arivazhagan, S. Narayanan and I. Debidutta Mishra: Hot corrosion behavior of monel 400 and AISI 304 dissimilar weldments exposed in the molten salt environment containing Na_2SO_4 + 60% V_2O_5 at 600°C. Mater Res. 2014;17:1273–1284. DOI:10.1590/1516-1439.274314

[32] Gokulkumar, K. Effect of Filler Metals on the Structure – Property Relationships and High Temperature Corrosion Studies on Dissimilar Joints of Inconel 625 and AISI 316L. PhD Thesis, VIT University, India, 2016.

Oxidation Behavior of Orthorhombic Ti_2AlNb Alloy

Joanna Małecka

Additional information is available at the end of the chapter

http://dx.doi.org/10.5772/63998

Abstract

The results of investigation on the oxidation behavior of orthorhombic Ti_2AlNb alloy with Al_2O_3 and AlCrN coating are presented. Oxidation was carried out in static air atmosphere at 700 and 800°C and in 9% O_2+0.2% HCl+0.08% SO_2+N_2 atmosphere at a temperature of 700–750°C. Investigation of the material structure of the specimen and chemical composition of oxidation products was performed. The surfaces were characterized using SEM (scanning electron microscopy) techniques. It was determined that the alloy shows a sufficient high-temperature corrosion resistance only at 700°C. At both temperatures, the coated samples exhibited reduced mass gain compared to uncoated alloy. At 700°C rather insignificant differences were observed; however, at the temperature of 800°C, the deposited coatings strongly limit the mass gain of the test material.

Keywords: orthorhombic alloys, SEM, high temperature corrosion, oxidation, coatings

1. Introduction

1960s of the twentieth century mark the increased development of research on the mechanisms and kinetics of oxidation of metals and alloys. The theoretical generalizations presented back then provided a lot of valuable information that is relevant today and are of great importance for further development of the theory of corrosion. In principle, every solid undergoes corrosion processes in various degrees, and with the progress of technical development, a number of problems arose in the use of metallic materials at high temperature and their resistance to oxidation. A complete removal of corrosion damage during the construction of materials is not possible; however, the amount of losses can be limited by the selection of suitable material. The observed trend in recent years is the increasing use of materials characterized by very attractive performance properties, and intermetallic phase TiAl alloys perfectly fit this trend.

The fundamentals behind industrial fabrication of titanium and its alloys are their unique physical and mechanical properties as compared with other construction materials. However, the development of technology creates the need to raise the requirements for engineering materials while ensuring competitiveness at the global level including all industries and is inextricably linked with the need to use materials that are characterized by improved mechanical properties, lower density, and greater resistance to high temperatures.

In recent years, a new group of advanced engineering materials has been formulated, featuring good practical properties, such as greater resistance to high-temperature oxidation in comparison to conventional titanium alloys [1–3], namely titanium alloys based on intermetallic phases. This group of materials, which was researched in the 1950s of the twentieth century, included alloys based on $Ti_3Al(\alpha_2)$ phase, alloys based on $TiAl(\gamma)$ and those based on $TiAl_3$ [3] which show high brittleness. The stimulus for research was the need to produce light and rugged materials for aviation and space industry, and they were supposed to replace titanium alloys and nickel-based alloys used in the construction of jet engines [2,4]. However, titanium alloys based on $TiAl(\gamma)$ have been used as construction materials. They are used in modern plane engines, featuring better efficiency, power saving and lesser emission of exhaust fumes. It should be underlined that new concepts of the development of intermetallics-based titanium alloys are continuously created. Toward the end of the 1980s of the twentieth century, a molecule of $Ti_2AlNb(O)$ [5–9] was introduced into the phase composition of titanium alloys, which caused a rise in their density, but at the same time improved other properties—among others—its plasticity. These materials are still at the research stage and are not yet produced commercially; however, it seems that wide application prospects are open for them and they may become an interesting offer for the modern industry as an alternative for the materials currently in use.

Great research effort [10–14] is put into improving their technological properties, increasing their ductility and resistance to oxidation, which is still the main obstacle for their application, especially in elements designed to have a working life. Alloy heat resistance depends primarily on the protective properties of the scale that forms during the course of oxidation. However, under high temperature, the formed scale is insufficient protection for the substrate material, resulting in its complete or partial destruction within a short period of time. The extension of lifetime of the material can be achieved by coating its surface with a special layer of protective nature. The coating and the substrate protected by it must be treated as a whole in operating conditions; therefore, the selection of the coating material should incorporate a number of specific requirements, and the primary factor should be the rate of diffusion exchange that occurs at high temperatures between the substrate material and the coating [15]. In order to meet the protective role and to be stable, the deposited coating must have properties compatible with the substrate material. Most importantly, these materials must have similar coefficients of thermal expansion to prevent cracking and peeling of the coating during temperature changes. In most cases, good protection of the material is desired for a long time, but in some cases operating time of the element is limited by other parameters as it is, for example in rocket engines, etc.

It should be noted that not only temperature but also the chemical composition of the corrosive environment has a great impact on oxidation rate. Structural elements working in high temperatures are often subjected not only to hot air action but, first and foremost, to aggressive environment containing sulfur compounds. Current research results show that even little quantities of sulfur compounds lead to a considerable, almost catastrophic increase in the rate of oxidation of titanium alloys based on intermetallic phases, and the resistance of titanium alloys to this type of corrosion is still insufficient.

2. Experimental procedures

The tests were performed on $Ti_2AlNb(O)$-based alloy. The chemical composition of the analyzed material is shown in **Table 1**.

Material			% at		
	Al	**Nb**	**Mo**	**V**	**Ti**
$Ti_2AlNb(O)$	25	12.5	6.01	0.48	balance

Table 1. Chemical composition of the material.

Two protective coatings were generated on the surface of the test material:

- Al_2O_3 deposited by sol-gel method,
- AlCrN deposited by physical vapor deposition.

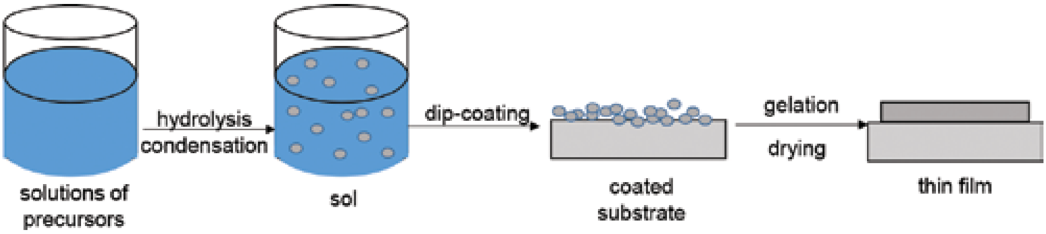

Figure 1. Stages of the dip-coating process.

The sol-gel technology is a gradual process of synthesizing ceramics, glasses or composites, which consists of preparing the sol (solution), formation of sol-gel and removing the solvent [16]. The stages of the process are presented in **Figure 1**. The first step of sol-gel method is mixing the precursor in the solvent, keeping the appropriate molar ratio of reagents. The next reaction is condensation (gelation), but its separation from the hydrolysis is only symbolic as both reactions occur almost simultaneously. Condensation means joining the products of hydrolysis. The last stage is gel maturation which covers continuous changes of its structure and properties. During maturation, polycondensation is continued and the simultaneous formation of gel increases its stiffness through thickening of intermolecular contractions and reduces porosity and specific surface. Maturation causes the strength of the gel to increase. It is important for the gel to be sufficiently strong to prevent cracking at the next stage of preparation [16,17]. Structural transformations during maturation are of key importance for the drying of the gel, which is a critical stage for the final effects of synthesis. During the drying process, liquids, i.e. alcohol and water, are removed from the network of pores. It is accompanied by capillary pressure, which is responsible for generating high stresses in the gel structure. If the pores are small (<20 nm), forming capillary stresses may cause abrupt cracking of gel. The value of capillary pressure is proportionate to the interfacial surface of gel, therefore the higher the reduction of that surface during maturation, the lower the pressure and the stresses during drying. Following maturation, the gel network is stiffer and harder which contributes to better resistance against stresses and cracks during drying. Coating stabilization may be carried out by two methods, chemically and thermally, either method aims at the same target which is the removal of hydroxy groups from the surface of the gel pores. Both forms of stabilization are associated with large structural changes in the surface. Thermal stabilization of gel would require dehydration of the two forms of water. The first of these is physically adsorbed water within the gel pores. The second form consists of hydroxyl groups associated with the gel surface, which is chemically adsorbed water. During thermal stabilization as the temperature increases, the following phenomena successively occur:

>170°C—removal of the physically adsorbed water,

<400°C—reversible dehydration, irreversible decay of organic residues,

>400°C—irreversible dehydration,

700–1300°C—closing the pores, creating non-porous material.

The time of thermal stabilization should be selected in such a way that the stresses in the structure of the gel are as small as possible. Correct performance of this process results in stable gel products.

In order to deposit Al_2O_3 coating by sol-gel method, the immersion method by "dip-coater" was applied. The scheme of the station is presented in **Figure 2**. After mixing the precursor in the solvent, gelation (condensation) of the substrates occurred and the gel matured with subsequent thermal stabilization. Synthesis of Al_2O_3 coating was carried out in the following conditions:

- the rate of immersion and resurfacing—34mm/min,
- the temperature of stabilizing the coating—800°C.

Figure 2. The scheme dip-coating process.

Multiple variations and modifications of PVD (Physical Vapour Deposition) methods are currently known that allow distinct improvement and increased operating properties of materials. These methods use a variety of physical phenomena such as vacuum cathode sputtering or evaporation of metals or metal alloys with Pa pressure reduced down from 10 to 10^{-5}. **Figure 3** shows a diagram of the elementary processes taking place during the deposition of coatings by PVD. The process of fabricating PVD coating consists of several steps, which may occur with various intensities or may be absent; sometimes they may also be amplified physically or chemically [18]:

- producing vapors of metals and alloys,
- electrical ionization of the supplied gases and metal vapors,
- crystallization of metal or metal compound from the plasma,
- condensation of plasma elements.

For the application of coatings, AlCrN target aluminum-chromium (Chromium Aluminum (AlCr) Alloy Sputtering Targets) was applied with a diameter of 100 mm, and the distance of samples from the target was 150 mm. The solid state coating material underwent vaporizing as a result of heat or ion bombardment. At the same time, nitrogen was introduced, acting as reactive gas. This resulted in the formation of a compound with the metal vapor and depositing a substrate in the form of a thin film with high adhesion. In the process, the substrates rotated at a constant speed around a few axes to obtain a uniform coating thickness. Schematic diagram of depositing the coatings by means of PVD is shown in **Figure 4**.

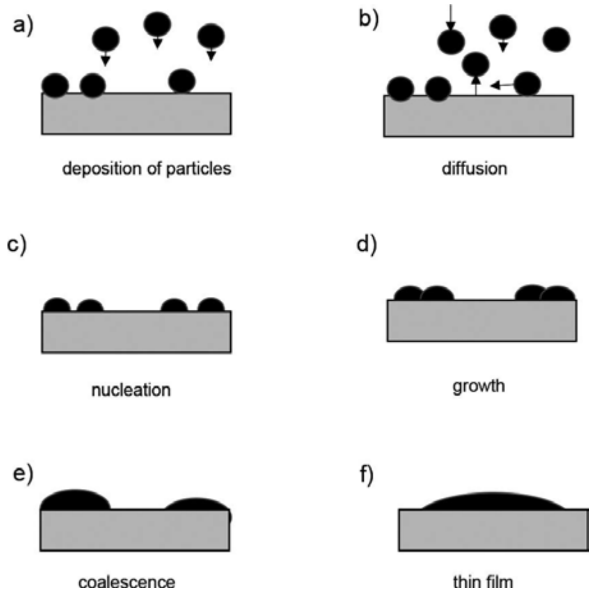

Figure 3. Elementary processes taking place during the deposition of coatings by PV.

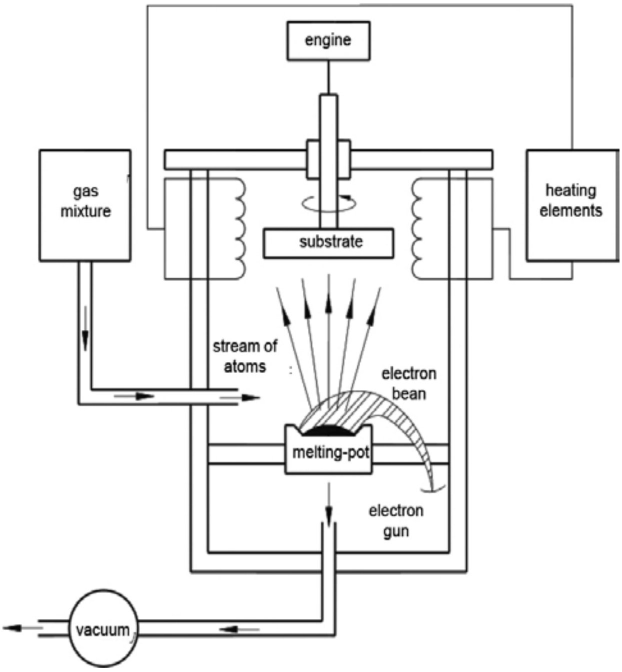

Figure 4. Schematic diagram of depositing the coatings by means of PVD.

The research on high-temperature oxidation was carried out at the station shown in **Figure 5**, using two types of atmospheres:

- hot air at a temperature of 700–800°C,
- atmosphere of 9% O_2+0.2% HCl+0.08% SO_2+N_2 at a temperature of 700–750°C.

The samples were heated up in the desired atmosphere with the furnace, then annealed at a given temperature, and subsequently cooled down to the room temperature. The gravimetric method was selected as a method of measuring the reaction speed; control of weight change was performed on an RADWAG precision scale with an accuracy 10^{-4} g. Trials were repeated three times and the presented test results are averaged.

Microstructural analyses were carried out by scanning electron microscopy, using a ZEISS SUPRA 35 and Hitachi S–4200 microscope equipped with EDS (energy dispersive spectroscopy) chemical composition analysis system and JSM35 JEOL microscope equipped with WDS (wavelength dispersive spectroscopy) system for analysis of the chemical composition. For research purposes, secondary electron (SE) and back-scattered electron (BSE) emissions were used. The etching of samples for structural tests was carried out using a reagent of the following chemical composition: 30ml $C_3H_6O_3$ + 15ml HNO_3 + 5ml HF. The methodology was applied for microstructural tests of both the initial-state samples and post-oxidation samples.

Figure 5. Research station.

X-ray studies of the analyzed materials were performed in X’Pert PRO PANalytical machine using filtered radiation of a lamp with a cobalt anode. X-ray phase analysis of tested materials was carried out in a Bragg-Brentano using Xcelerator strip detector and the solid angle geometry of the incidence of the primary beam (**Figure 6**) using a parallel beam collimator before the proportional detector.

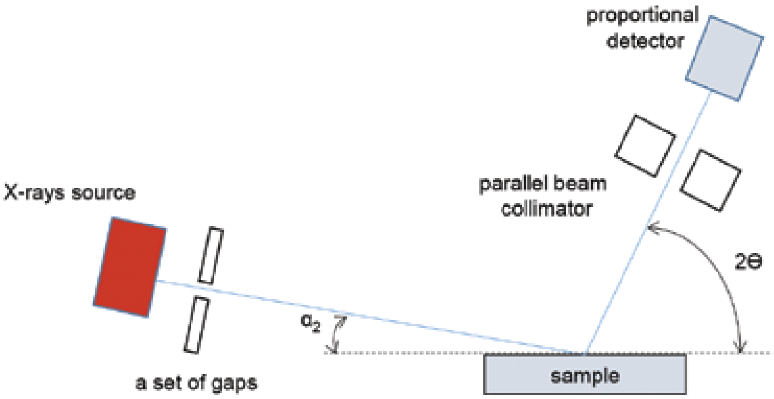

Figure 6. Goniometer arrangement for diffraction image recording in grazing incidence geometry [19].

3. Results and discussion

The microstructure of orthorhombic titanium aluminides may vary widely depending on processing methods and subsequent heat treatments [20]. The classification of orthorhombic alloys allows distinguishing typical microstructures: (a) equiaxed, (b) bimodal, (c) lamellar, and (d) lamellar with coarse secondary O laths and thick grain-boundary α_2 phase. The structure of the test alloys is presented in **Figure 7** and the type can be established as lamellar. It is a typical microstructure generated as a result of beta heat treatment of the material. The XRD (X-ray diffraction patterns) plots are shown in **Figure 8**.

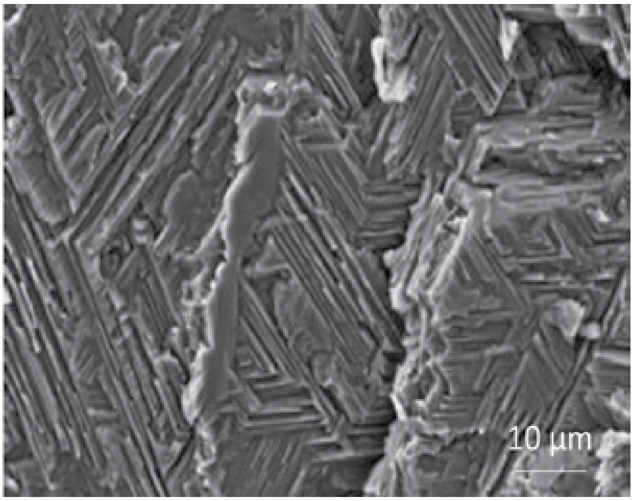

Figure 7. Microstructure of Ti-25Al-12.5Nb-6.01Mo-0.48V alloy.

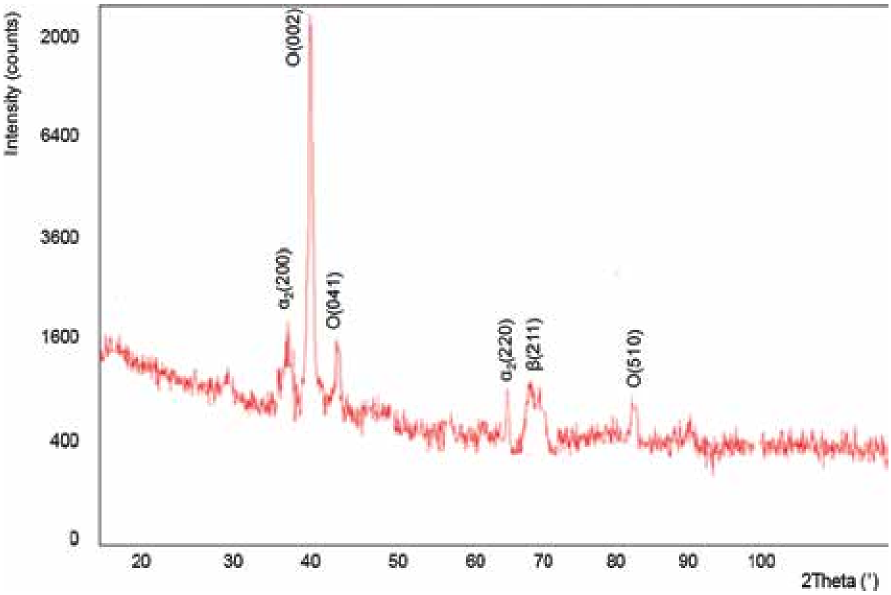

Figure 8. X-ray diffraction patterns acquired in Bragg-Brentano geometry of Ti-25Al-12.5Nb-6.01Mo-0.48V alloy.

The applied method of X-ray qualitative phase analysis performed for the deposited coatings, carried out in Bragg-Brentano geometry, confirms the presence of the respective phases in the material of the coating and substrate (**Figures 9** and **10**).

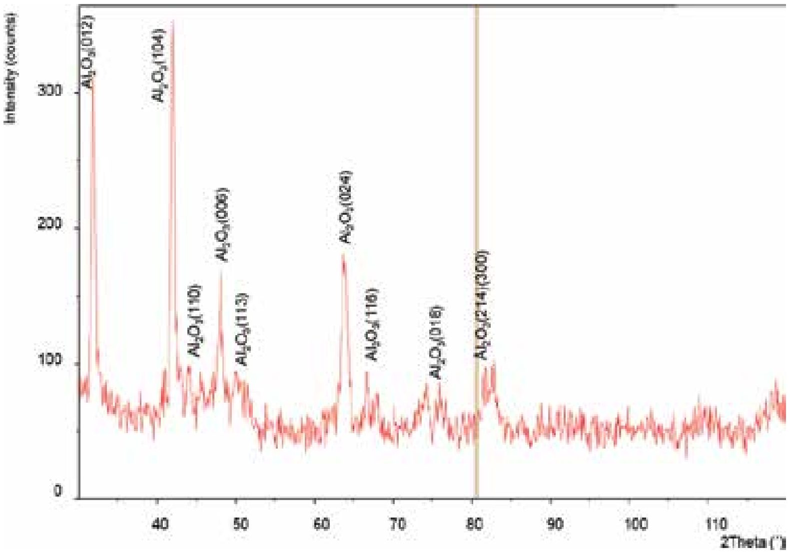

Figure 9. X-rays diffraction patterns acquired in Bragg-Brentano geometry of Al_2O_3 coatings obtained in sol-gel method.

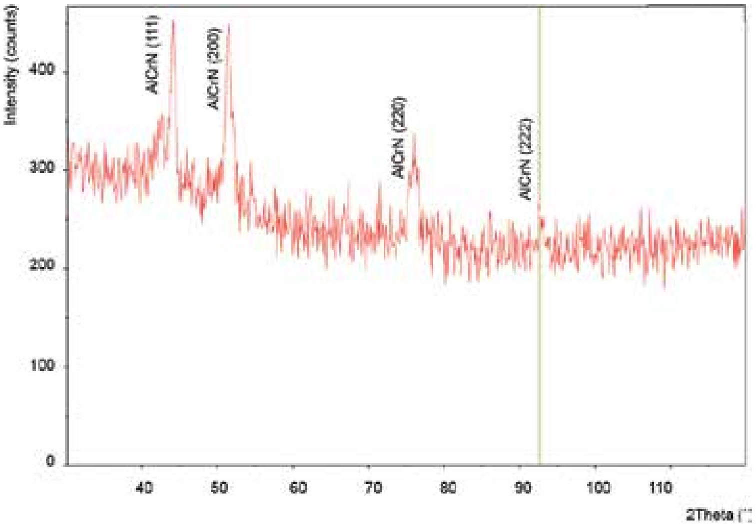

Figure 10. X-ray diffraction patterns acquired in Bragg-Brentano geometry of AlCrN coatings obtained in sol-gel method.

The course of isothermal oxidation kinetics of the alloy Ti-25Al-12.5Nb-6.01Mo-048V in the initial state and with coatings $Al_2O_3$and AlCrN deposited in air is presented in **Figure 11**. Oxidation at 700 and 800°C for 500 hours only causes mass gain, which, however, increases significantly at 800°C. The oxidation products formed exhibited adhesion to the metallic substrate for the entire duration of the test and after it. The course of the oxidation in air at 700°C exhibits rather linear course of the kinetics of oxidation, which means a continuous oxidation during exposure to high temperature, whereas during the oxidation at a temperature of 800°C, there was a change in the course of oxidation toward a course close to the parabolic. The difference in mass gain of the alloy samples oxidized at 700°C is practically insignificant, and already at 800°C significant differences were observed with definite advantage to the applied coatings. At a temperature of 700°C, the increase in mass gain occurs only at the initial period (lasting about 100 hours), and then the process slows down with mass gains on a comparable level. Samples with the coating of AlCrN show superior mass gain after oxidation in air at 700°C as compared to the alloy without coating, only up to 50th hour of oxidation and then smaller mass gains are visible. As a result, after 500 hours of isothermal oxidation, mass gains for each of the applied cases do not exceed 0.2 mg/cm^2. Oxidation in air at 800°C is characterized by decidedly larger variations; the oxide layer increases progressively, the mass gain is gradual, and therefore, it equals to approximately 1.1 mg/cm^2 for an uncoated alloy after 500 hours of oxidation. For the applied coating up to about 50th hour of oxidation, mass gains are comparable, but the differences become apparent only with elongation of exposure time. Thus, the reduction of the process rate can be determined in favor of the alloy coated with Al_2O_3, and AlCrN: a significant reduction in alloy oxidation process was observed for the coating with AlCrN, and the coating here acts as an effective protection against oxidation.

Apart from reducing the rate of oxidation, the scales' adhesion to the metallic substrate is also of great importance. Despite the fact that during the tests and immediately after their completion the scale formed on the coated and uncoated alloy showed good adhesion to metallic substrates, under the influence of dynamic strain loads, products near the fracture line of the uncoated alloy partially chipped already after the oxidation at a temperature of 700°C (**Figure 12**). Such chipping was not observed for coated specimens.

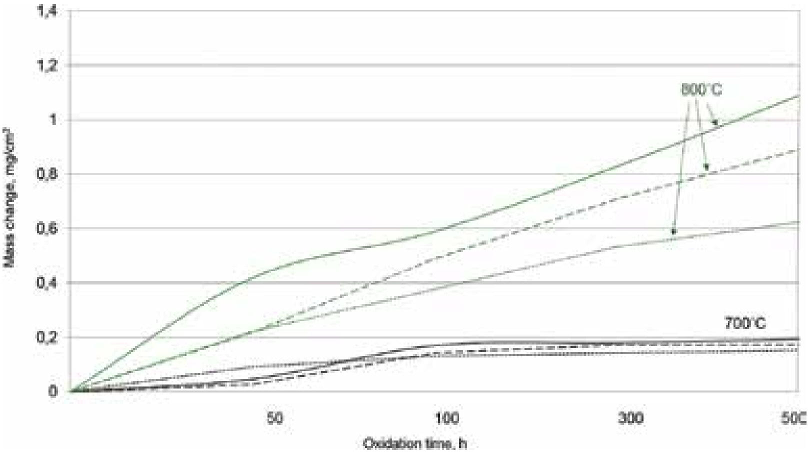

Figure 11. The mass change of Ti-25Al-12.5Nb-6.01Mo-0.48V alloy oxidized isothermally in air at 700 and 800°C (continuous curves—uncoated alloy; dashed curves—Al_2O_3-coated alloy; doted curves—AlCrN-coated alloy).

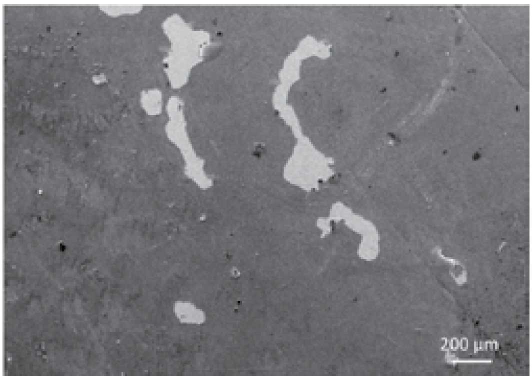

Figure 12. Fragmentary products chipped observed after oxidation in air at 700°C.

From survey of the kinetic curves during oxidation of the alloy in an atmosphere containing 9% O_2 + 0.2% HCl + 0.08% SO_2 + N_2 (**Figure 13**), it follows that already at a temperature of 700°C, and the mass gain is almost two-fold compared to the oxidation in air at the same temperature. The oxidation at 750°C displays a faster course of oxidation and increasing mass gain; however, for the uncoated alloy after 300 hours of oxidation at this temperature, a rapid increase in the rate of oxidation is observed. The influence of coatings on the course of oxidation cannot be omitted here: both coatings promote gradual decrease of mass gain. The coated samples of the alloy have similar course up to 300th hour of oxidation, then a visible halt in the oxidation rate can be noticed as well as the decrease in mass gain. Both coatings contribute to limiting the process. In oxidation trials, the material destruction process includes the formation of oxides in heating cycles, chipping during cooling and holding in room temperature, and the total thickness of the resulting oxide layer is dependent on time and temperature of the oxidizing atmosphere. Diffusion processes activate along with the temperature rise and oxidation time.

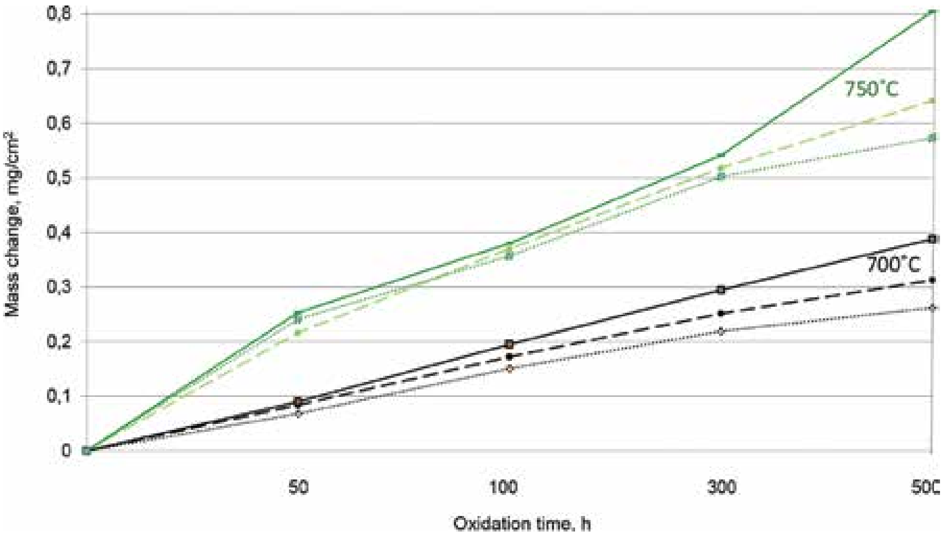

Figure 13. The mass change of Ti-25Al-12.5Nb-6.01Mo-0.48V alloy oxidized isothermally in 9% O_2+ 0.2% HCl + 0.08% SO_2+ N_2 at 700 and 800°C (continuous curves—uncoated alloy; dashed curves—Al_2O_3-coated alloy; doted curves—AlCrN-coated alloy).

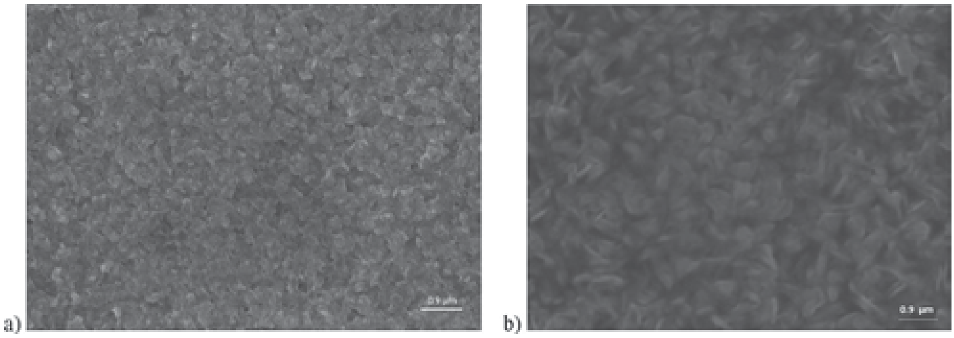

Figure 14. The surface Ti-25Al-12.5Nb-6.01Mo-0.48V after 100 (a) and 500 (b) hours of isothermal oxidation in air at 700°C.

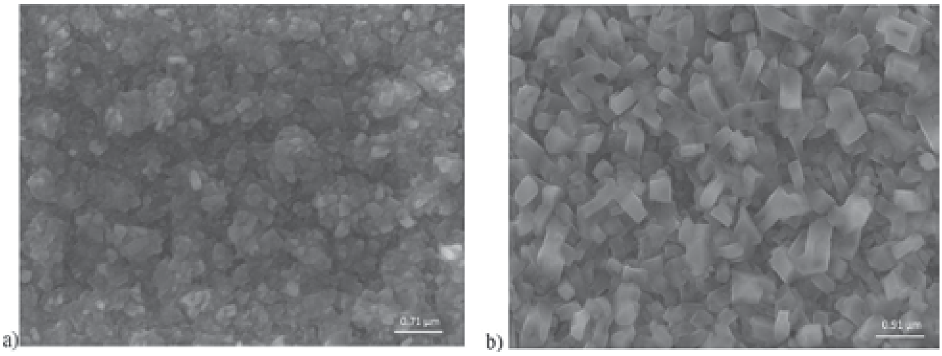

Figure 15. The surface Ti-25Al-12.5Nb-6.01Mo-0.48V after 100 (a) and 500 (b) hours of isothermal oxidation in air at 800°C.

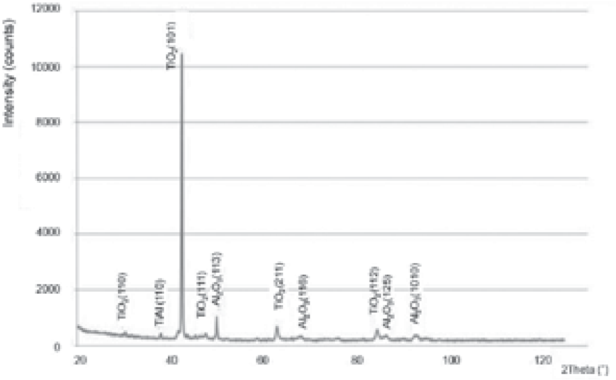

Figure 16. X-ray diffraction patterns acquired in Bragg-Brentano geometry of surface according to **Figure 14**.

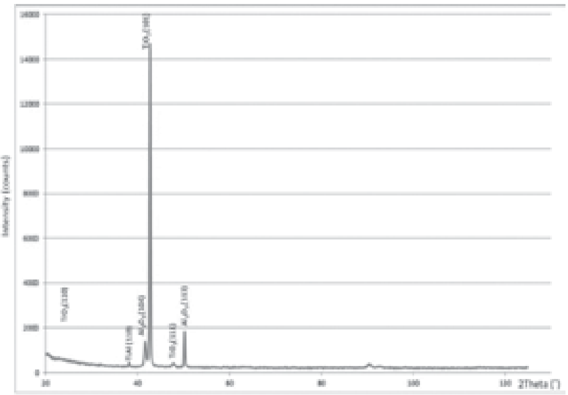

Figure 17. X-ray diffraction patterns acquired in Bragg-Brentano geometry of surface according to **Figure 15**.

Observations using SEM highlighted that the surface of the scale has a specific structure. After oxidation in air at 700°C, it is quite an irregular structure in the form of specific eruptions (**Figure 14**) loosely growing over the next sublayer, with a lamellar morphology typical of aluminum oxide. Increasing the temperature to 800°C results in the formation of the outer layer with a different morphology. The surface is formed from eruptions with the structure of irregular columnar crystallites grown in different directions (**Figure 15**). In the time interval between 50 and 100 hours, they have very small size and irregular construction. Observation of the outer surface of the products carried out after a longer time of oxidation (300–500 h) reveals that columnar rutile crystallites formed as a result of simultaneous processes of surface diffusion and out-core diffusion of titanium ions have a much larger size. These crystallites at the surface are located at different angles to each other and in relation to the surface from which they grow. The results of XRD of the surface layer (**Figures 16** and **17**) show the peaks of TiO_2; however, several Al_2O_3 phases also occur in the region of the outer oxidized layer, resulting in the formation of morphologically soft and porous oxides on the surface.

The areas of the scale's cross-section formed on the analyzed alloy are shown in **Figures 18** and **19**. The results of chemical analysis performed by the WDS in the respective characteristic regions are provided in **Tables 2** and **3**.

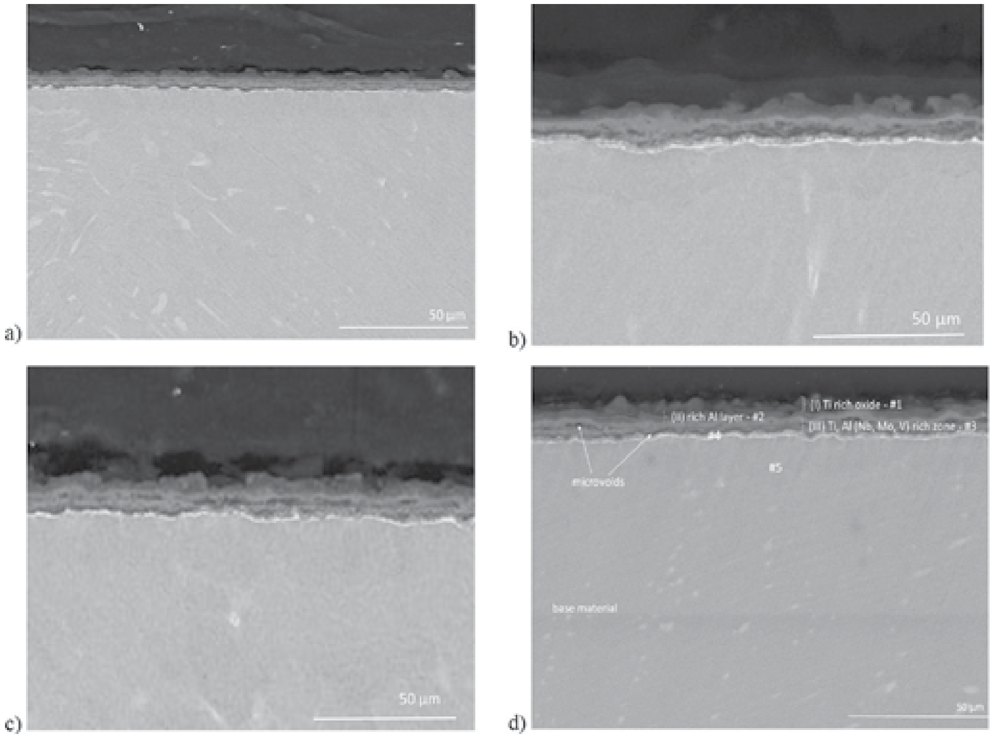

Figure 18. Cross-section of the scale formed on Ti-25Al-12.5Nb-6.01Mo-0.48V after 50 (a); 100 (b); 300 (c); 500 (d) hours of isothermal oxidation in air at 700°C.

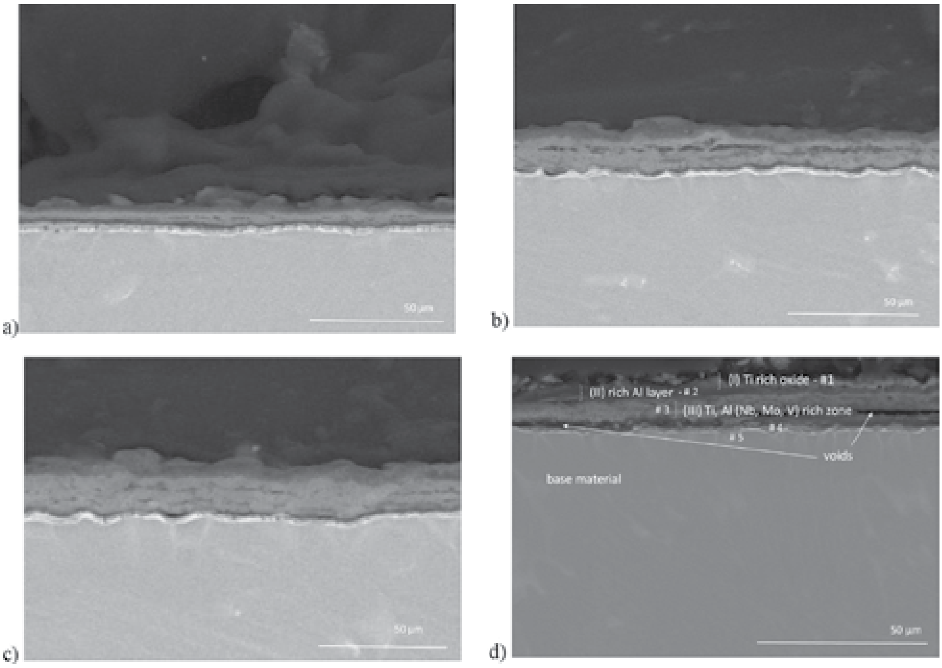

Figure 19. Cross-section of the scale formed on Ti-25Al-12.5Nb-6.01Mo-0.48V after 50 (a); 100 (b); 300 (c); 500 (d) hours of isothermal oxidation in air at 800°C.

	NO	Al	Nb	Ti	Mo	V	
#1	0.00	54.40	12.46	5.35	27.79	–	–
#2	0.00	53.95	31.24	0.36	13.27	0.61	0.47
#3	0.00	51.58	19.72	2.37	25.48	0.85	–
#4	14.24	18.46	18.73	10.93	35.47	1.81	0.36
#5	3.70	7.63	25.27	11.07	48.94	2.97	0.42

Table 2. WDS-analysis (at.%) of locations labeled in **Figure 18d**.

	N	O	Al	Nb	Ti	Mo	V
#1	0.00	59.49	11.84	4.85	23.82	–	–
#2	0.00	55.62	37.27	0.72	5.83	0.56	–
#3	0.00	54.98	21.00	1.98	20.87	0.80	0.37
#4	16.60	19.00	20.82	8.91	33.35	1.20	0.12
#5	2.44	11.79	26.96	10.98	44.44	3.01	0.38

Table 3. WDS-analysis (at.%) of locations labeled in **Figure 19d**.

Basically, the scale formed showed the concentration of fine pores and a layered structure made of alternate layers. This is due to the fact that Ti has been selectively oxidized to TiO_2, under which the elements Nb and Al were relatively enriched. Then the oxygen diffusing through a layer rich in TiO_2 reacted with Nb and Al, which allowed for the formation of a layer most likely enriched in $AlNbO_4$. Under the layer rich in $AlNbO_4$, Ti is enriched again. Therefore, a multilayer scale is formed consisting of alternating layers rich in TiO_2 and $AlNbO_4$. It was observed that oxygen and nitrogen were present in the interface between the oxide scale and the metallic substrate, and subsurface embrittlement caused by formation of the nitride layer and the penetration of air/nitrogen was evident (microvoids).

The analyzed alloy is characterized by the formation of a scale as the reaction product and the formation of the diffusion area of interstitial elements in the metallic substrate. Oxide layers formed during annealing consist of a few characteristic sublayers, however, with a similar structure and chemical composition. External sublayer (I) existing at the phase boundary with an oxidant (air) consists predominantly of rutile accumulations also containing Al oxides. Middle sublayer (II) forms a band extending parallel to the oxidized surface and characterized by the fact that BSE observation gives gray-graphite contrast, which is not heterogeneous. This band has a lot of Al_2O_3 but little TiO_2. The fact that these oxides come separately causes the non-uniformity of contrast. Aluminum cations which diffuse out-core (slower than Ti) form Al_2O_3 with the oxygen. A protective layer will be formed in the reaction products only when it exclusively contains Al_2O_3. The Al_2O_3 layer formed is heterogeneous and not compact. Its content also includes TiO_2 rutile, however, in lesser amount. The presence of even a small amount of TiO_2 in the sublayer rich in Al_2O_3 enables a two-way diffusion, thus resulting in the growth of the product on the outer surface and at the interface product-metallic substrate. The inner sublayer (III) contains comparable amounts of Al_2O_3 and TiO_2. Moreover, it contains oxides of alloying elements included in the composition of the analyzed alloy. Microvoids occur between this sublayer and the metallic substrate. As the temperature rises, the number of microvoids rises, as well as their size and their tendency to join is observed. The structure of this phase boundary determines the possibility of scale buckling during cooling. Thus, Nb, Mo, and V co-create oxides in virtually any sublayer. It can be noticed that in the region of product-substrate micropores' boundary is actively developing. Thus, out-core diffusion of metal ions is accompanied by the increase in concentration of vacancies at the interface between the substrate-product, until a break in cohesion occurs in nano-regions and then micro-regions. Compressive stresses generated upon oxidation and cooling the sample down to the room temperature cause the buckling of the layer and its removal from the substrate. Diffusion processes taking place on the flat interface cause the coalescence of vacancies, the formation of microvoids, and their joining into bands. Due to the fact that the decohesion of oxide fragments from the substrate requires high shear stresses at the interface, the "weakening" of phase boundary by the microvoids promotes the process of buckling. Buckling, in turn, induces a tensile stress and micro-cracks in the layer separated from the surface, consequently causing cracking, crushing, and chipping of scale fragments. Phase separation at the interface of the scale/metal substrate occurs as a result of the tensile stresses generated in direction tangential to the interface of the scale/metal substrate and compressive stresses in the transverse direction to the border of the phases. As a result of the impact of both types of stresses, a local separation of the scales from the surface of the substrate material occurs. The result is the formation of discontinuities in scale adhesion to the metal substrate. This can cause increased susceptibility to detachment of the scale during oxidation.

In the initial period of scale growth, poor tensile stresses formed on the alloy oxidized at 700°C in a direction tangential to the interface oxide/metal substrate and compressive stresses in a direction transverse to the interfacial oxide/metal substrate. At the same time, small voids began to form in the region of the interface of scale/substrate. The increase of oxidation temperature (up to 800°C) leads to increased stresses and expansion of discontinuity at the interface of oxide/metal substrate. After 500 hours of oxidation, voids widened creating small cracks in the scale, which decreases protective properties of the scale.

The result of the oxidation of the alloy Ti-25Al-12.5Nb-6Mo-0.48V in the atmosphere of 9% O_2 + 0.2% HCl + 0.08% SO_2+N_2 is the formation of reaction products characterized by completely different morphology than that observed in previous studies. Oxidation in such conditions causes the formation of specific eruptions on the outer surface, under which another sublayer is revealed (**Figures 20** and **21**).

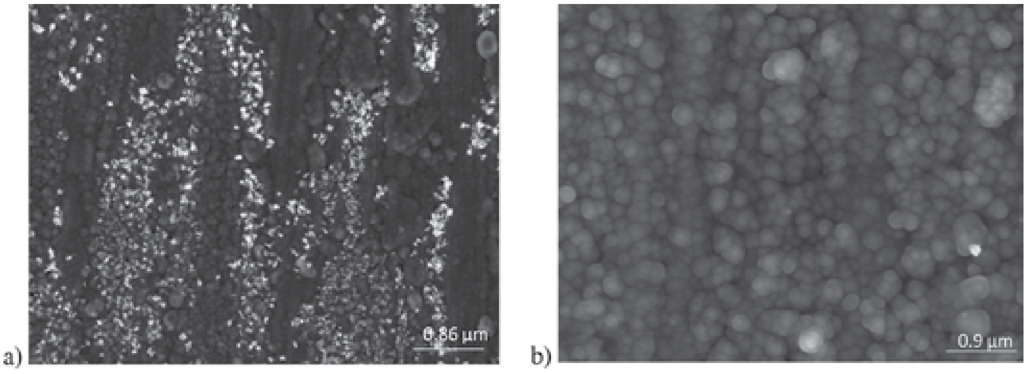

Figure 20. The surface Ti-25Al-12.5Nb-6.01Mo-0.48V after 100 (a) and 500 (b) hours of isothermal oxidation in 9% O_2+ 0.2% HCl + 0.08% SO_2+ N_2 atmosphere at 700°C.

Analysis of the chemical composition of the outer surface of the scale (**Figure 22**) proved that the forming outer layer is composed mainly of the mixture of oxides Al and Ti. Nb and traces of S were observed on the oxidized surface. Metallographic examination showed that the forming oxides grow with increasing temperature and time of the process. Temperature rise of the process causes the formation of scale with distinct whisker-like morphology of oxides (**Figure 21**) which effectively hinders protection of the alloy against the impact of corrosive environment in the next stages of the test. In consequence, after 500 hours of oxidation at a temperature of 750°C, the surface is covered with columnar eruptions irregularly arranged relative to each other (**Figure 21d**).

The examination of cross-sectional metallographic specimens after experiment in the atmosphere of 9% O_2+ 0.2% HCl + 0.08% SO_2+ N_2 allowed revealing the multi-layered nature of the scale (**Figure 23**) with distinct separation of borders between the sublayers. The sequence of products and their morphology is essentially not different from the products obtained during the oxidation in air.

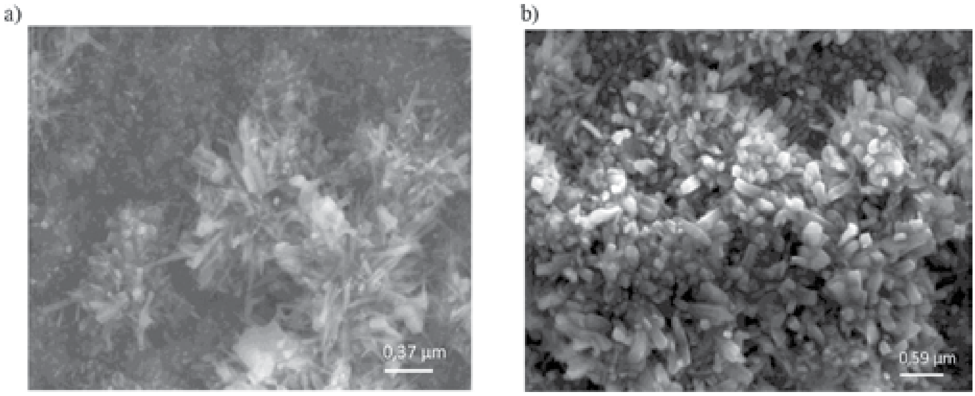

Figure 21. The surface Ti-25Al-12.5Nb-6.01Mo-0.48V after 100 (a) and 500 (b) hours of isothermal oxidation in 9% O_2+ 0.2% HCl + 0.08% SO + N_2 atmosphere at 800°C.

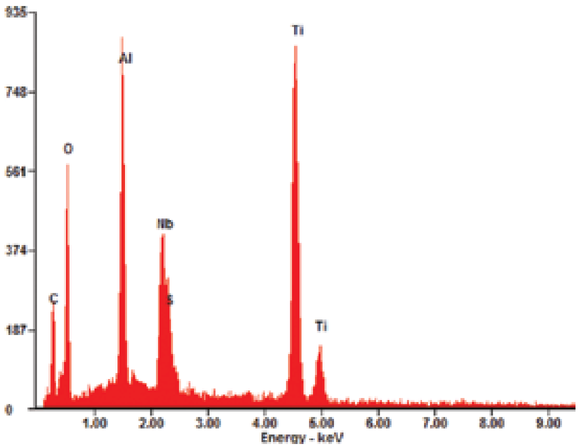

Figure 22. EDX analysis results in place according to **Figure 21**.

Based on the chemical composition analysis of the layers, it was determined that similar to oxidation in air, directly under the outer layer (I) containing mainly Ti and Al, a sublayer is formed with a dominance of Al (II), and another mixed sublayer rich in titanium oxides, aluminum, and alloying elements (III) with a dominance of Ti. The detailed chemical composition of respective layers is presented in **Tables 4** and **5**. It is noteworthy that the layer of corrosion products formed in the atmosphere of 9% O_2+ 0.2% HCl + 0.08% SO_2+ N_2 already at 700°C is characterized by porous structure (**Figure 23**). Therefore, it does not provide sufficient protection against the destructive impact of corrosive environment. Lower cohesion of the scale facilitates bidirectional transport of metal ions and oxidants (O and N), causing the product to grow faster on both phase interfaces, i.e. product-substrate interface and product-oxidant interface.

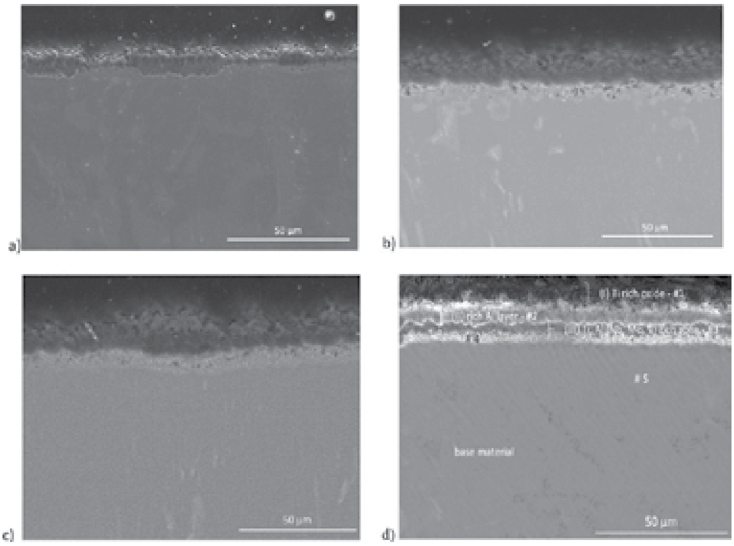

Figure 23. Cross section of the scale formed on Ti-25Al-12.5Nb-6.01Mo-0.48V after 50 (a); 100 (b); 300 (c) and 500 (d) hours of isothermal oxidation in 9% O_2+ 0.2% HCl + 0.08% SO_2+ N_2 atmosphere at 700°C.

	N	O	S	Al	Nb	Ti	Mo	V
#1	0.00	49.99	3.21	14.31	5.78	26.71	0.00	0.00
#2	0.00	55.74	0.00	36.17	0.97	6.29	0.71	0.12
#3	0.00	44.61	7.91	18.92	1.93	24.76	1.02	0.85
#4	18.21	19.54	0.00	17.65	9.65	32.15	2.15	0.65
#5	3.81	10.24	0.00	25.93	13.12	43.30	3.31	0.29

Table 4. WDS-analysis (at.%) of locations labeled in **Figure 23d**.

	N	O	S	Al	Nb	Ti	Mo	V
#1	0.00	56.01	4.57	10.07	4.21	25.14	0.00	0.00
#2	0.00	54.35	0.00	37.86	1.19	5.64	0.51	0.45
#3	0.00	43.47	6.27	21.53	2.04	25.37	0.72	0.60
#4	13.74	20.78	0.00	21.22	8.73	33.17	1.85	0.51
#5	2.37	8.56	0.00	27.47	10.95	47.22	2.84	0.59

Table 5. WDS-analysis (at.%) of locations labeled in **Figure 24d**.

SEM observations showed that the scale has a compact, homogeneous structure, with numerous small discontinuities (**Figures 23** and **24**). During oxidation in air, the scale composed of characteristic eruptions forms on the surface, and the scale which is formed during the oxidation in the model atmosphere is characterized by the presence of needle-shaped oxides growing on its surface and expanding as the oxidation time increases. During the oxidation in air, it was observed that the layer closest to the substrate is characterized by irregular structure, with pits inside material and extensive discontinuity propagating between the layers. On the other hand, a thicker layer formed during the oxidation in an aggressive atmosphere has visible and noticeable pores. In this layer, relatively large amount of sulfur and chlorine is also noticeable from the viewpoint of corrosion (**Tables 4** and **5**).

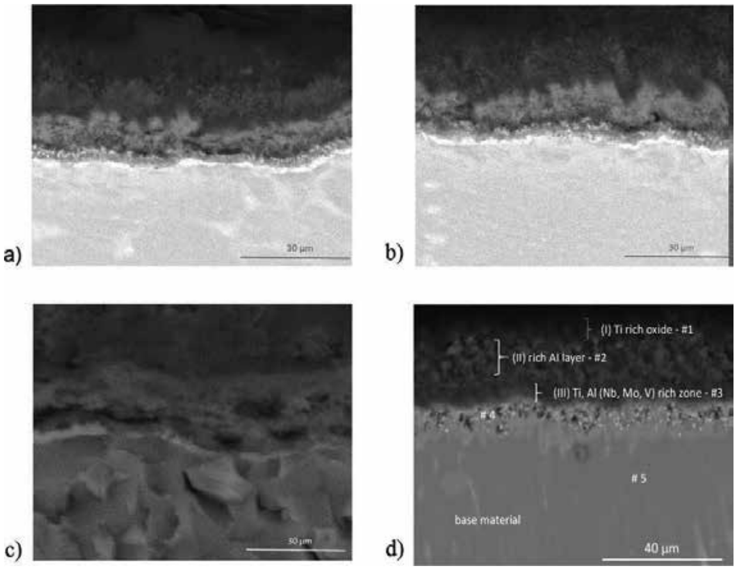

Figure 24. Cross section of the scale formed on Ti-25Al-12.5Nb-6.01Mo-0.48V after 50 (a); 100 (b); 300 (c) and 500 (d) hours of isothermal oxidation in 9% O_2+ 0.2% HCl + 0.08% SO_2+ N_2 atmosphere at 800°C.

Most likely, such course of reaction is caused by reactivity of sulfur vapors which belong to the most aggressive ones as regards corrosion due to the fact that sulfur reacts with almost all metallic elements. The similarity of morphological structure between sulfide scale and oxide scale results from the corresponding mechanism of its growth (outward diffusion of alloying elements). The difference lies in better developed porous outer layer and larger sizes of grains forming the outer compact layer. Despite the similarities, the mechanism of sulfide scale growth is more complicated than oxide scale growth. It follows from a larger number of thermodynamically stable metal sulfides as compared to oxides, and also the fact that the structure of defects in sulfides is more complicated and yet to be sufficiently explained. Despite the fact that the mechanism of sulfur corrosion has been well researched, the difficulties posed in these experiments cause that analysis of heterogeneous reaction occurring at high temperatures in atmospheres with sulfur compounds leave many unexplained correlations. Other factors complicating the sulfidation of metals and alloys are the changes occurring in metal sulfides. Sulfides of common metals are less stable thermodynamically, have lower melting points, and display significant deviation from stoichiometry as compared to corresponding oxides. The course of corrosion of T Ti-25Al-12.5Nb-6.01Mo-0.48V alloy in the atmosphere of 9%O_2+0.2%HCl+0.08% SO_2+N_2 may be compared to corrosion occurring in air. However, in the environment containing even such small amounts of sulfur, metallic materials resistant to high-temperature oxygen corrosion may undergo degradation, which can lead to breakaway corrosion.

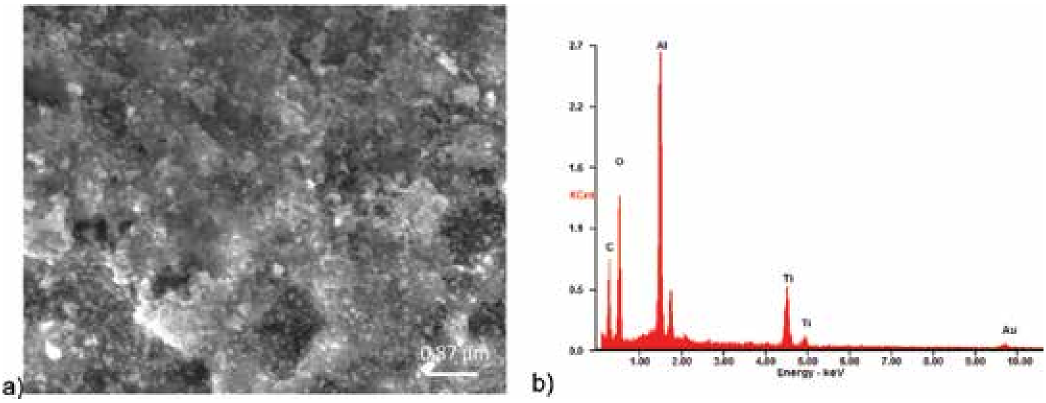

Figure 25. The surface Ti-25Al-12.5Nb-6.01Mo-0.48V coated Al_2O_3 after isothermal oxidation in air (a); EDX analysis results in place according to **Figures 25a** (b).

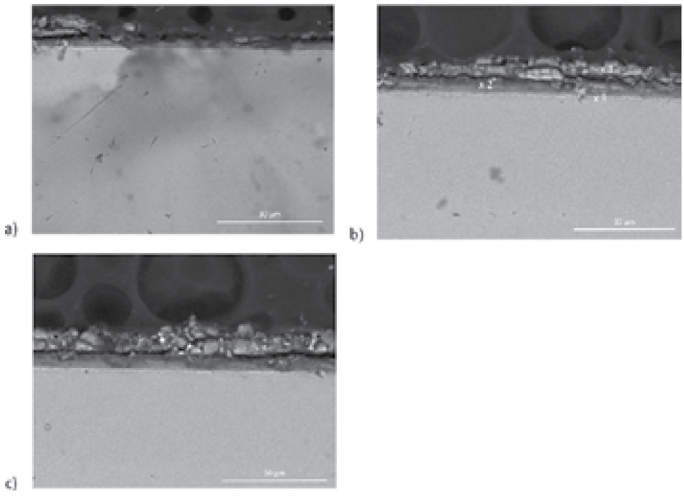

Figure 26. Cross-section of the scale formed on Ti-25Al-12.5Nb-6.01Mo-0.48V coated Al_2O_3 after 100 (a); 300 (b) and 500 (c) hours of isothermal oxidation in air at 700°C.

The morphological structure of the scale formed upon the oxidation of the alloy coated with Al_2O_3 (**Figures 26 – 28**) shows a difference in the outer surface construction. A characteristic feature of the surface is that it is characterized by the finest construction. The outer layer is therefore made of quite a porous scale that is visible over the entire surface of the oxidized alloy independent of the temperature and oxidation time. It can be concluded that the pellets observed on the surface consist mainly of Al_2O_3 and to a lesser extent, TiO (**Figure 26**). Due to diffusion processes occurring at high temperature, the coating of Al_2O_3 undergoes transformation; compact and dense initial Al_2O_3 coating is dissolved, and its place is taken by a porous scale. Analysis of the chemical composition shows mainly the occurrence of small amounts of Ti (**Figure 25**), which diffuses directly from the substrate due to the impact of high temperature. Elongation of the oxidation time causes that under the porous outer layer other sublayers are formed characterized by the presence of regions of high heterogeneity, discontinuity and buckling (**Figures 26** and **28**). The scale formed is multi-layered; in particular regions, detailed analysis of the composition was performed (the results are presented in **Tables 6** and **7**). Interfaces between the individual layers are clearly visible, as well as the resulting discontinuities along the scale, that grow as the oxidation time increases.

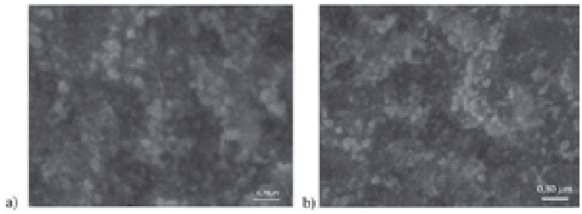

Figure 27. The surface Ti-25Al-12.5Nb-6.01Mo-0.48V coated Al_2O_3 after 100 (a) and 500 (b) hours of isothermal oxidation in air at 800°C.

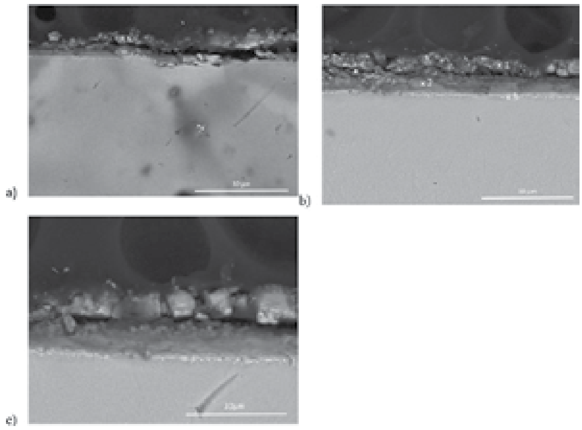

Figure 28. Cross section of the scale formed on Ti-25Al-12.5Nb-6.01Mo-0.48V coated Al_2O_3 after 100 (a); 300 (b) and 500 (c) hours of isothermal oxidation in air at 800°C.

During the oxidation of the alloy, the dissociation of the Al_2O_3 coating occurs, and the oxygen diffusing to the substrate from the coating reacts with Ti and forms TiO compounds during the oxidation process. Cross-sectional metallographic specimens show that the thickness of the scale is homogeneous, but it increases with the rise of the oxidation temperature. After partial wear and dissociation of the original Al_2O_3 coating, the in-core diffusion of oxygen and ex-core diffusion of Ti accelerates scale growth.

	N	O	Al	Nb	Ti	Mo	V
#1	–	48.12	44.61	–	7.27	–	–
#2	–	25.92	38.21	2.13	33.74	–	–
#3	–	23.11	26.94	17.32	29.98	2.31	0.34

Table 6. WDS-analysis (at.%) of locations labeled in **Figure 27b**.

	N	O	Al	Nb	Ti	Mo	V
#1	–	46.91	45.14	–	7.95	–	–
#2	–	28.11	41.06	1.97	28,86	–	–
#3	–	22.97	27.03	16.53	29.86	2.97	0.64

Table 7. WDS-analysis (at.%) of locations labeled in **Figure 28b**.

During the oxidation of the alloy with the coating, probably the dissociation of Al_2O_3 coating occurs, and the oxygen diffusing to the substrate from the coating reacts with Ti and forms TiO compounds during the oxidation process. Probably, niobium originating from the substrate of the alloy does not react with Al_2O_3 layer, which is confirmed by tests carried out by Mader and Rühler [21] who established that no reaction layer is formed between the Nb and Al_2O_3 in the high-temperature oxidation. Al_2O_3 compound reacts with Ti because of the high solubility of oxygen in titanium and occurring diffusion of oxygen to the metallic substrate. During the oxidation of this alloy, it is noted that in this case also a light layer is formed (interface between the oxide scale and the metallic substrate), which was identified as the region rich in Nb. Due to the inter-diffusion that occurs between the coating layer and the substrate of Ti-25Al-12.5Nb-6.01Mo-0.48V alloy, it is the original Al_2O_3 layer that was transformed. A small amount of Ti was found that diffused from the alloy O-Ti_2AlNb due to the impact of high temperature. In this case, the ongoing isothermal oxidation resulted in the formation of oxide lumps on the surface of the sample. It can be concluded that the lumps consist essentially of Al_2O_3 and TiO_2 to a lesser extent. The source of these recognizable peaks is the oxidized O-Ti_2AlNb alloy. So the oxidation of the metallic substrate of alloy-Ti_2AlNb

occurred under a layer of Al_2O_3 coating. The compact and dense initial Al_2O_3coating dissolved and its place was taken by a porous scale. From the cross-cut metallographic specimens, it can be seen that the thickness of the oxide scale is uniform. Lumps in the outer layer consist primarily of Al_2O_3. After partial wear and dissociation of the original Al_2O_3 coating, the in-core diffusion of oxygen and ex-core diffusion of Ti accelerates scale growth.

During the oxidation of tested alloy coated Al_2O_3 in an atmosphere containing 9% O_2+ 0.2% HCl + 0.08% SO_2+ N_2, a pronounced impact of the oxidizing environment on the intensity of high-temperature corrosion was observed.

Both during the oxidation of the alloy coated with Al_2O_3 in the air and in the model atmosphere of 9% O_2+ 0.2% HCl + 0.08% SO_2+ N_2, the outer layer is made of quite a porous scale that is visible over the entire surface of the oxidized alloy independent of the temperature and oxidation time. However, due to the diffusion processes in the aggressive atmosphere, well developed oxide lumps are formed on the surface of the sample (**Figures 29** and **32**), whose size increases as the oxidation time increases. The surface is characterized by the presence of regions of high heterogeneity, discontinuity, and buckling. There is occurrence of chlorine and sulphur compounds on the outer surface of the scale (**Figure 30**). In general, the scale formed during oxidation in air has a similar structure, but it is much thinner. Tests carried out on transverse sections (metallographic specimens) show that the oxidation products exhibit a multilayered structure with discontinuities of high porosity. Three specific areas can be distinguished: internal, external and central (**Figures 31** and **33**), while chlorine and sulphur decreases inwardly from the outer layer, and in the layer directly adjacent to the material (Item 3, **Tables 8** and **9**) compounds of S and Cl were not found. Oxidation in the model atmosphere causes buckling and separation of scale from the substrate, which leads to the conclusion that the applied coating in this case was not a sufficient protection against the exposure to oxidizing environment.

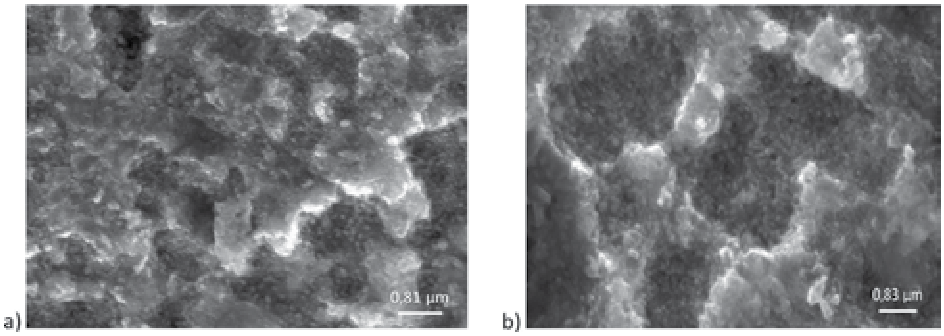

Figure 29. The surface Ti-25Al-12.5Nb-6.01Mo-0.48V coated Al_2O_3 after 100 (a) and 500 (b) hours of isothermal oxidation in 9% O_2+ 0.2% HCl + 0.08% SO_2+ N_2 atmosphere at 700°C.

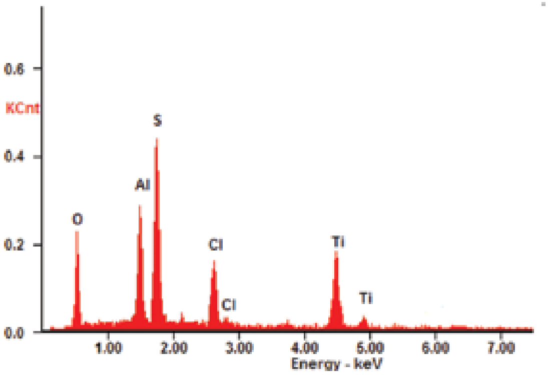

Figure 30. EDX analysis results in place according to **Figure 29**.

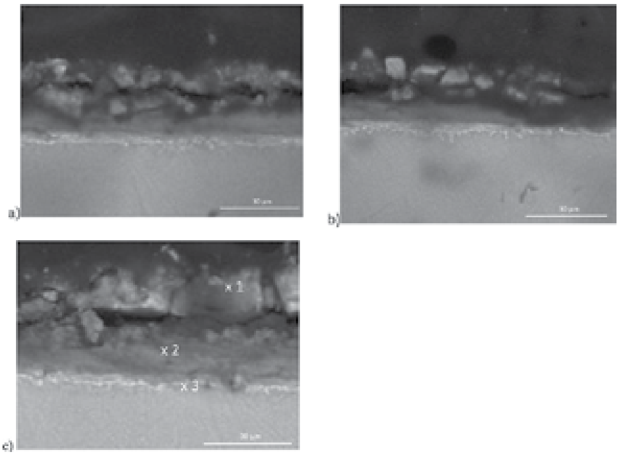

Figure 31. Cross section of the scale formed on Ti-25Al-12.5Nb-6.01Mo-0.48V coated Al_2O_3 after 100 (a); 300 (b) and 500 (c) hours of isothermal oxidation in 9% O_2+ 0.2% HCl + 0.08% SO_2+ N_2 atmosphere at 700°C.

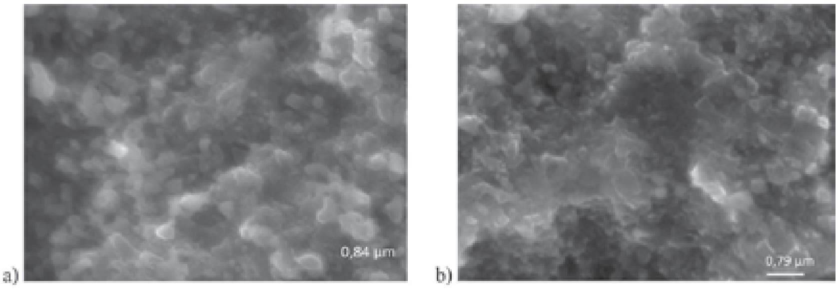

Figure 32. The surface Ti-25Al-12.5Nb-6.01Mo-0.48V coated Al_2O_3 after 100 (a) and 500 (b) hours of isothermal oxidation in 9% O_2+ 0.2% HCl + 0.08% SO_2+ N_2 atmosphere at 750°C.

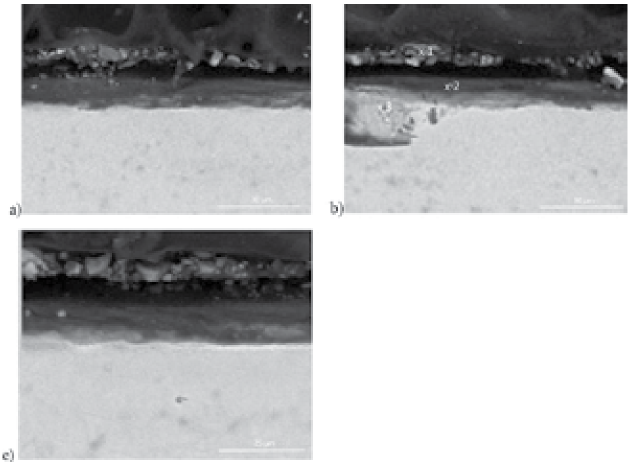

Figure 33. Cross-section of the scale formed on Ti-25Al-12.5Nb-6.01Mo-0.48V coated Al_2O_3 after 100 (a); 300 (b) and 500 (c) hours of isothermal oxidation in 9% O_2+ 0.2% HCl + 0.08% SO_2+ N_2 atmosphere at 750°C.

	O	Al	Nb	Ti	Mo	V	S	Cl
#1	37.55	43.68	–	12.78	–	–	1.67	4.32
#2	28.04	36.21	3.53	30.96	–	–	0.06	1.20
#3	21.36	27.76	17.32	30.27	3.01	0.28	–	–

Table 8. WDS-analysis (at.%) of locations labeled in **Figure 31c**.

	O	Al	Nb	Ti	Mo	V	S	Cl
#1	37.69	41.21	–	14.12	–	–	2.03	4.95
#2	34.65	38.74	5.27	19.99	–	–	0.57	0.78
#3	19.54	28.27	15.97	32.20	3.49	0.53	–	–

Table 9. WDS-analysis (at.%) of locations labeled in **Figure 33b**.

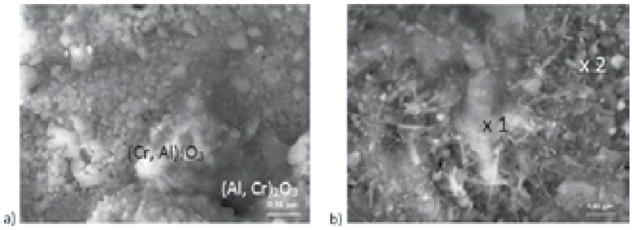

Figure 34. The surface Ti-25Al-12.5Nb-6.01Mo-0.48V coated AlCrN after 100 (a) and 500 (b) hours of isothermal oxidation in air at 700°C.

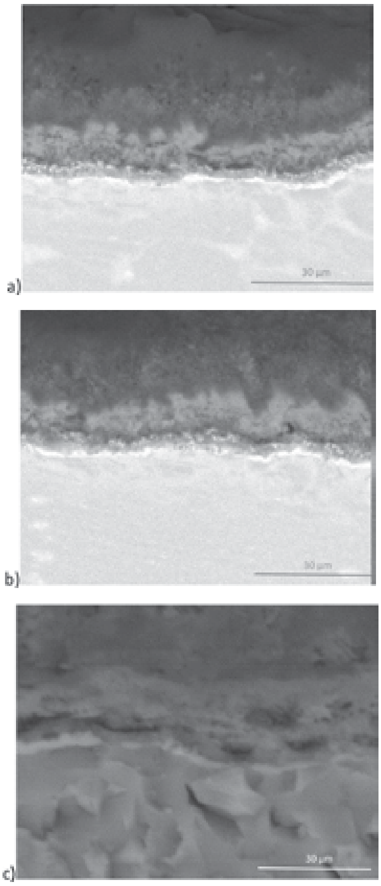

Figure 35. Cross section of the scale formed on Ti-25Al-12.5Nb-6.01Mo-0.48V coated AlCrN after 100 (a); 300 (b) and 500 (c) hours of isothermal oxidation in air at 700°C.

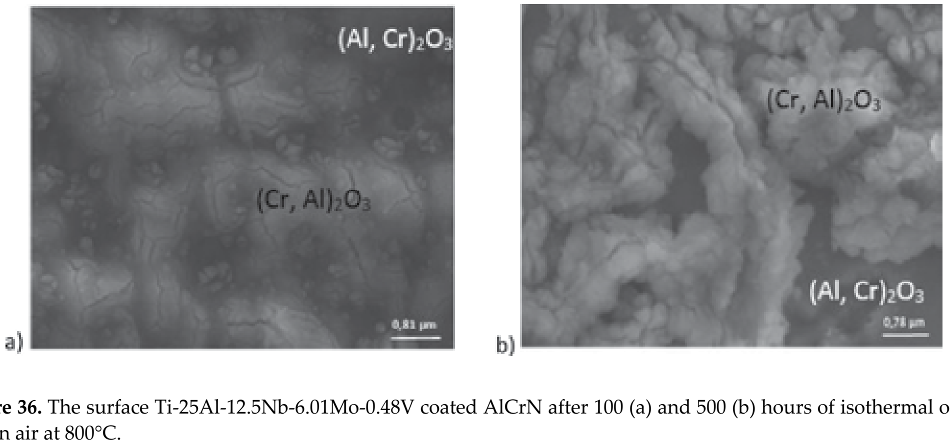

Figure 36. The surface Ti-25Al-12.5Nb-6.01Mo-0.48V coated AlCrN after 100 (a) and 500 (b) hours of isothermal oxidation in air at 800°C.

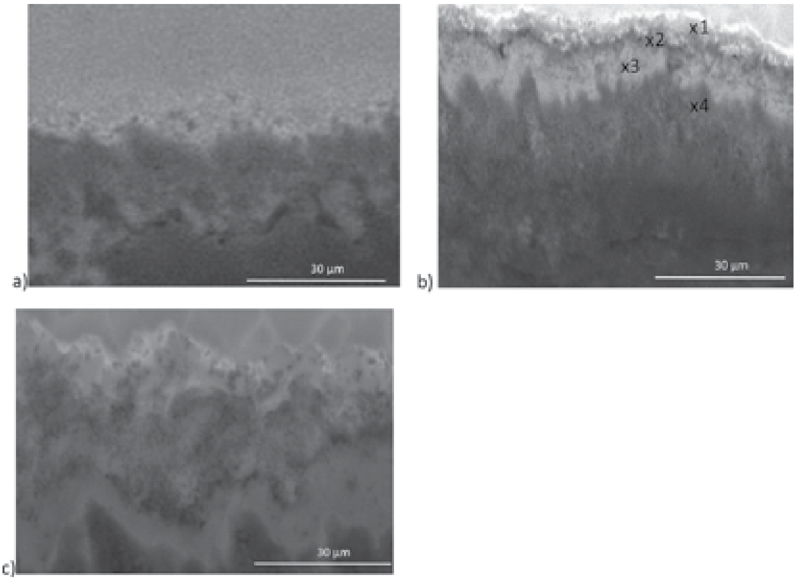

Figure 37. Cross section of the scale formed on Ti-25Al-12.5Nb-6.01Mo-0.48V coated AlCrN after 100 (a); 300 (b) and 500 (c) hours of isothermal oxidation in air at 800°C.

	Al	Ti	Cr	O
×1	20.98	0.96	31.25	46.81
×2	29.21	0.56	21.24	48.99

Table 10. WDS-analysis (at.%) of locations labeled in **Figure 34b**.

	O	Al	Nb	Ti	Cr	N
#1	46.93	20.21	–	1.41	31.45	–
#2	61.57	28.95	–	0.27	9.21	–
#3	–	1.03	1,72	46.47	–	50.78
#4	–	66.21	–	5.78	–	28.01

Table 11. WDS-analysis (at.%) of locations labeled in **Figure 37b**.

As a result of high temperature exposition regardless of the oxidizing environment, the alloy coated with AlCrN forms a scale characterized by lighter and darker contrasting areas (**Figures 34** and **35**). A thin layer rich in chromium-oxide was formed on the surface of the outer layer, while images of cross-section through the formed scale show that the layer of

AlCrN formed during oxidation dissociates, and a two-phase high-porosity oxide mixture takes its place (**Figures 35** and **37**). The chemical composition of specific regions of the scale formed during air oxidation is shown in **Table 10** and on its basis, it may be concluded that darker spots are composed mainly of aluminum oxide with a low quantity of chromium (Item 2), while lighter spots are high-chromium content phase with a lower content of aluminum (Item 1). Observations carried out on cross-section of the scale showed similar chemical compositions (**Table 11**), whereas directly at the interface between the scale and the substrate Ti- and N-rich area is revealed (Item 3) which promotes the formation of titanium nitrides, which depletes the resources of titanium from the metallic substrate at the same time. As a result of the occurring processes, precipitating of Al-rich phase takes place (Item 4). In the case of oxidation at a lower temperature (700°C), similar results were obtained and the dissociation and oxidation of the protective coating was also observed.

Similar results were obtained for the oxidation in the atmosphere containing 9% O_2+ 0.2% HCl + 0.08% SO_2+ N_2. SEM observations showed a scale of homogeneous structure with numerous small discontinuities. During the oxidation in air, the scale composed of the characteristic eruptions forms on the surface, and the scale which is formed during the oxidation in the 9% O_2 + 0.2% HCl + 0.08% SO_2 + N_2 atmosphere is characterized by the presence of needle-shaped oxides growing on its surface and expanding as the oxidation time increases (**Figures 38** and **40**). Compared to the oxidized samples coated with Al_2O_3, the scale is characterized by a compact structure. The cross section of the scale formed in an atmosphere 9% O_2 + 0.2% HCl + 0.08% SO_2 + N_2 shows, similar to the oxidation in the air, the characteristic multi-layered structure with distinct interfaces between the sub-layers (**Figures 39** and **41**). During the oxidation in air, it was observed that the layer closest to the substrate is characterized by irregular structure, with pits inside material and extensive discontinuity propagating between the layers. On the other hand, a thicker layer formed during the oxidation in an aggressive atmosphere has visible and noticeable pores. In this layer, relatively large amount of sulfur and chlorine is also noticeable from the viewpoint of corrosion (**Table 12**).

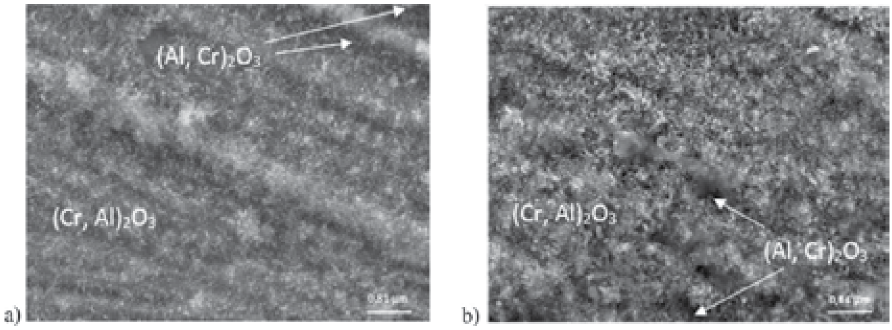

Figure 38. The surface Ti-25Al-12.5Nb-6.01Mo-0.48V coated AlCrN after 100 (a) and 500 (b) hours of isothermal oxidation in 9% O_2+ 0.2% HCl + 0.08% SO_2+ N_2 atmosphere at 700°C.

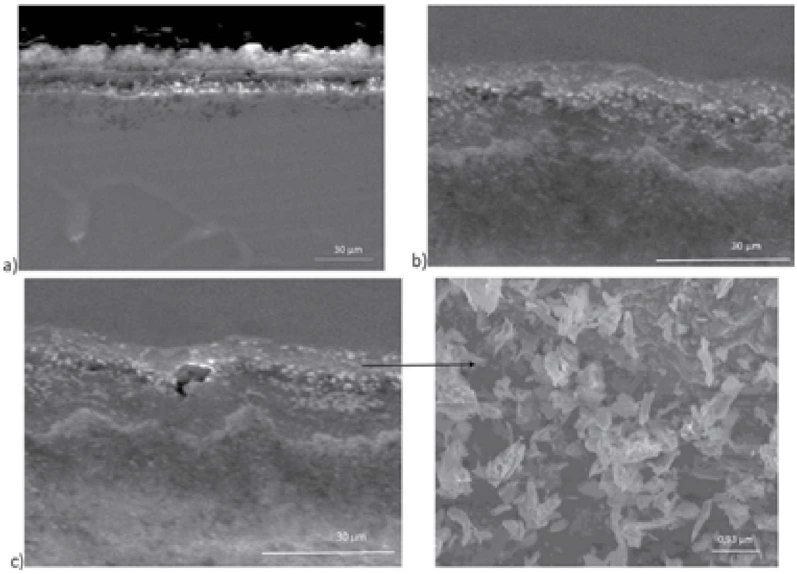

Figure 39. Cross section of the scale formed on Ti-25Al-12.5Nb-6.01Mo-0.48V coated AlCrN after 100 (a); 300 (b) and 500 (c) hours of isothermal oxidation in 9% O_2+ 0.2% HCl + 0.08% SO_2+ N_2 atmosphere at 700°C.

During high-temperature oxidation, AlCrN coating deposited on the test alloy Ti-25Al-12.5Nb-6Mo-0.48V caused the formation of a mixed scale rich in chromium and alumina on the surface, which posed an effective barrier against the diffusion of oxygen. The oxidation of the coated substrate occurs here as a result of in-core diffusion of oxygen and out-core diffusion of coating elements. However, fast out-core diffusion of chromium caused the formation of regions rich in Cr_2O_3 in the outer layer of the scale as well as aluminum rich regions. Despite the fact that due to the impact of high temperature, the AlCrN coating dissociates, and no oxidation of titanium nitride formed under the scale is observed. A completely different process is observed for uncoated specimens where this layer is oxidized to TiO_2 due to the increase of partial pressure and does not provide a sufficient protection.

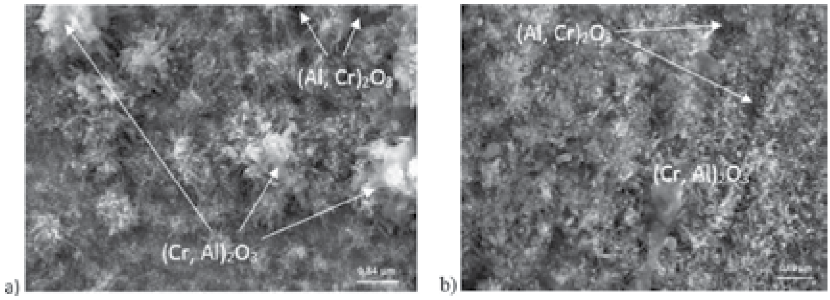

Figure 40. The surface Ti-25Al-12.5Nb-6.01Mo-0.48V coated Al_2O_3 after 100 (a) and 500 (b) hours of isothermal oxidation in 9% O_2+ 0.2% HCl + 0.08% SO_2+ N_2 atmosphere at 750°C.

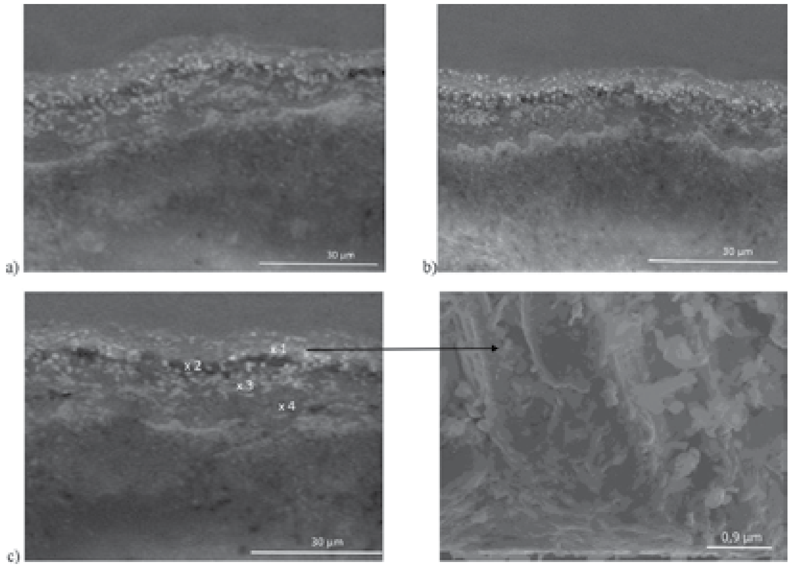

Figure 41. Cross section of the scale formed on Ti-25Al-12.5Nb-6.01Mo-0.48V coated AlCrN after 100 (a); 300 (b) and 500 (c) hours of isothermal oxidation in 9% O_2+ 0.2% HCl + 0.08% SO_2+ N_2 atmosphere at 750°C.

	O	Al	Nb	Ti	Cr	N	S	Cl
#1	44.65	19.97	–	2.17	32.21	–	0.03	0.97
#2	58.88	27.37	–	0.58	10.03	–	0.93	2.21
#3	–	096	2.14	44.87	–	52.03	–	–
#4	–	62.69	–	9.17	–	28.14	–	–

Table 12. WDS-analysis (at.%) of locations labelled in **Figure 41c**.

4. Conclusion

1. During the oxidation of the alloy Ti-25Al-12.5Nb-6.01Mo-0.48V in the initial state in the atmosphere of air a multiphase scale forms, consisting of three layers: an outer layer comprising a mixture of TiO_2 and lower quantity of Al_2O_3, heterogeneous middle layer predominantly composed of Al_2O_3 with small amounts of TiO_2 and an inner layer of comparable quantities of TiO_2 and Al_2O_3.

2. In the case of Ti-25Al-12.5Nb-6.01Mo-0.48V coated with Al_2O_3, during the exposure to high temperature on the surface of the coating layer, reaction products are formed, because a diffusion exchange takes place between the components of the alloy and the protective layer which leads to significant changes in the composition of material and protective layer near the interface coating-substrate. Multiple layered nature of the scale

was proven with delamination and cracks: the scale consists of a thin layer cracked at the material and due to the influence of aggressive atmosphere, its detachment from the substrate material follows. In this case the oxidation of the metallic substrate of O-Ti_2AlN alloy occurred under the coating of Al_2O_3; compact and dense initial Al_2O_3 coating dissolved, and in its place was taken by a porous scale. After partial wear and dissociation of the original Al_2O_3 coating, the in-core diffusion of oxygen and ex-core diffusion of Ti accelerates the scale growth.

3. The surface of the scale formed on the alloy with the coating AlCrN has a definitely different character. The oxidation in the case results in the formation of an oxide scale consisting of a mixture of the two phases of different composition, namely the base phase $(Al, Cr)_2O_3$ and a thin surface layer rich in chromium oxide $(Cr, Al)_2O_3$. Underneath the AlCrN coating, which is subject to partial dissociation, a TiN area is formed along with precipitations of niobium- and aluminum-rich phase.

4. The corrosive process of the alloy Ti-25Al-12.5Nb-6.01Mo-0.48V in the environment of 9% O_2+ 0.2% HCl + 0.08% SO_2+ N_2 is comparable to corrosion occurring in the air; however, in an environment containing even such small quantities of sulfur the material rapidly degrades, which in turn may cause breakaway corrosion. The chemical composition of the scales presented in this paper is similar and its analysis reveals the presence of sulfides and chlorine compounds in the outer layer of the scale, and their share in respective layers is dependent on the temperature and their exposure time.

5. The growth of the multilayered sulfide scales occurs by out-core diffusion of metal cations (Ti, Al, Nb) in the crystallographic lattice structure and in-core diffusion of sulfur and chlorine compounds through discontinuities in the layer surface. The sequence of sublayers and their morphology basically do not differ from the products obtained during oxidation in air because there is practically no difference in the sequence of their formation. A massive difference is, however, the occurrence of distinctive "pits" in respective sublayers, and a specific feature of the scale formed in the aggressive atmosphere is its porous morphology and voids in each sublayer, which definitely promotes the diffusive processes. It can be said that respective sublayers are not compact (as in the case of oxidation in air separated from each other in a characteristic way), which facilitates the transportation of sulfur and chlorine into the material through its discontinuity, and the region closest to the material contains (white band enriched with Nb) oxides limiting the dissolution of sulfur and chlorine.

6. From the very beginning of the test, the role of chlorine in this case is small while the active processes are linked to oxidation and sulfuration. The presence of sulfur at the beginning and the end of the test is the result of discontinuities in the scale, through which occurs the intake of the corrosive atmosphere to naked parts of the material and the resumption of corrosive processes including sulfur. The spallation of the corrosion products does not promote in this case the formation of the oxide layer and initiates the corrosive processes in the naked spots. In consequence, the scale formed in these conditions may reduce the diffusion of chlorine and sulfur, not allowing to form chlorides and sulfides.

Acknowledgements

The research study was financed from the funds for science in 2013–2015 as research project no. IP 2012 055772.

Author details

Joanna Małecka

Address all correspondence to: j.malecka@po.opole.pl

Faculty of Mechanical Engineering, Opole University of Technology, Opole, Poland

References

[1] APPEL F., PAUL J. D. H., OEHRING M.: Gamma titanium aluminide alloys, Wiley-VCH Verlag GmbH (2011).

[2] LORIA A.: Gamma titanium aluminides as prospective structural materials, Intermetallics 8 (2000) 1339–1345.

[3] SZKLINIARZ W.: Metallic materials with the participation of intermetallic phases (in Polish). Z. Bojar and W. Przetakiewicz (Eds.), Technical Military Academy, Warsaw (2006).

[4] KUMPFERT J., LEYENS C.: Titanium and titanium alloys, fundamentals and applications. C. Leyens and M. Peters (Eds.), Wiley-VCH Verlag GmbH & Co. KGaA, Weinheim (2003).

[5] BANERJEE D., GOGIA A. K., NANDY T. K., JOSHI V. A.: A new ordered orthorhombic phase in a Ti_3Al_2Nb alloy, Acta Metallurgica A36 (1988) 871–882.

[6] KUMPFERT J.: Intermetallic alloys based on orthorhombic titanium aluminide, Advanced Engineering Materials 3 (2001) 851–864.

[7] MOZER B., BENDERSKY L. A., BOETTINGER W. J.: Neutron powder diffraction study of the orthorhombic Ti_2AlNb phase, Scripta Metallurgica et Materialia 24 (1990) 2363–2368.

[8] MURALEEDHARAN K., GOGIA A. K., NANDY T. K., BANERJEE D., LELE S.: Transformations in a Ti-24Al-15Nb alloy: part I. Phase equilibria and microstructure, Metallurgical and Materials Transaction A 23A (1992) 401–415.

[9] ROWE R.G., BANERJEE D., MURALEEDHARAN K., LARSEN M., HALL E. L., KONITZER D. G, WOODFIELD A. P.: in Titanium ’92 Science and Technology. F. H. Froes and I. Caplan (Eds.) TMS, Warrendale, PA (1993) 1259–1266.

[10] CHAN K. S.: Developing hydrogen-tolerant microstructures for an alpha-2 titanium aluminide alloy, Metallurgical and Materials Transactions 23A (1992) 497–507.

[11] JIQIANG WANG, LINGYAN KONG, TIEFAN LI, TIANYING XIONG: Oxidation behavior of thermal barrier coatings with a $TiAl_3$ bond coat on γ-TiAl alloy, Journal of Thermal Spray Technology 24/3 (2015) 467–475.

[12] KAKARE S.A., TONEY J. B. ASWATH P. B.: Oxidation of ductile particle reinforced Ti-48Al composite, Metallurgical and Materials Transactions 26A (1995) 1835–1845.

[13] TAKASAKI A., FURUYA Y., TANEDA Y.: Hydrogen uptake in titanium aluminides covered with oxide layers, Metallurgical and Materials 29A (1998) 307–314.

[14] YOUNG-WON KIM, WILFRIED SMARSLY, JUNPIN LIN, DENNIS DIMIDUK, FRITZ APPEL (Eds): Gamma Titanium Aluminide Alloys: A collection of research on innovation and commercialization of gamma alloy technology, The Minerals, Metals & Materials Society. Wiley TMS (2014), United States of America.

[15] MROWEC S., WERBER T.: Gas Corrosion of Metals, Publishing House “Silesia” Katowice (1975) (in Polish)

[16] HENCH L., OREFICE R.: Sol–gel technology. Kirk-Othmer Encyclopedia of chemical technology, John Wiley & Sons, Inc. (2000)

[17] BRINKER C. J., SCHERER G. W. (Eds.).: Sol–gel science. The physics and chemistry of sol-gel processing, Gulf Professional Publishing (1990), United States of America

[18] BURAKOWSKI T, WIERZCHOń W.: Surface engineering, WNT, Warszawa 1995 (in Polish).

[19] BACZMARSKI A., BRAHAM C., SEILER W., SHIRAKI N.: Multi-reflecion method and grazing incidence geometry used for stress measurement by X-ray diffraction, Surface and Coatings Technology 182 (2004) 43–54.

[20] KUMPFERT J., ASSLER H., MIRACLE D.B., SPOWART J. E.: Transverse Properties of Titanium Matrix Composites, Proc. of Materials Week 2000, Symposium: Biomimetic Processing of Structural Material, (2000) Munich.

[21] MADER W., RUHLER M.: Electron microscopy studies of defects at diffusion-bonded Nb/Al_2O_3 interface, Acta Mater. 37, 1989, p. 853–866

Chapter 5

Electrochemical Studies of Corrosion in Liquid Electrolytes for Energy Conversion Applications at Elevated Temperatures

Aleksey V. Nikiforov, Irina M. Petrushina and
Niels J. Bjerrum

Additional information is available at the end of the chapter

http://dx.doi.org/10.5772/64003

Abstract

Stainless steels (AISI 316, 321 and 347), high-nickel alloys (Hasteloy®C-276 and Inconel®625), tantalum, nickel, titanium, tungsten, molybdenum, niobium, platinum, and gold were tested for corrosion resistance in molten KH_2PO_4 (or KH_2PO_4-$K_2H_2P_2O_7$) as a promising electrolyte for the intermediate-temperature (200–400°C) water electrolysis. Pt, Ta, Nb, Ti, Inconel®625, and Ni demonstrated high corrosion resistance. Au and the rest of the tested materials were not corrosion resistant. It means that Ni, Ti and Inconel®625 may be used as relatively cheap construction materials for the intermediate-temperature water electrolyzer.

Keywords: Intermediate-temperature electrolysis, bipolar plates, nickel stability, corrosion, oxygen evolution, molten salts

1. Introduction

Use of the renewable energy is often combined with storage of excess energy. Water electrolysis is one of the most effective ways of energy storage. Produced hydrogen can be used in the hydrogen refueling stations for fuel cell cars or used as a reactant with CO_2 in the Sabatier synthesis producing methane.

There are two types of the available commercial electrolyzers with different electrolyte: (1) alkaline water electrolyzer (AWE) (2) proton exchange membrane (PEM) water electrolyzer.

INTECH
open science | open minds

The latter has much higher voltage efficiency than the former system. However, in alkaline electrolyzers, non-noble Ni-based catalysts are used, but in the PEM water electrolyzers, the noble Pt and IrO_2 catalysts are used. The use of noble metal catalysts could become a problem for mass production.

Intermediate temperature water electrolysis has a potential to combine high efficiency with cheap catalysts. The molten KH_2PO_4 is a promising candidate for a proton-conducting electrolyte. Moreover, it has been shown that WC is a better catalyst than Pt for the hydrogen evolution reaction in this electrolyte at 260°C [1].

In this paper, corrosion resistance of stainless steels (AISI 316, 321 and 347), high-nickel alloys (Hasteloy®C-276, Inconel®625), tantalum, nickel, titanium, tungsten, molybdenum, niobium, platinum, and gold was studied in the molten KH_2PO_4-$K_2H_2P_2O_7$ system.

Earlier, we have studied corrosion behavior of the same materials at 150°C in concentrated phosphoric acid as model system for the polybenzimidazol/phosphoric acid electrolyte [2–4]. This polymeric electrolyte was studied as a high-temperature (up to 200°C) alternative to the Nafion® electrolyte in PEM water electrolyzers. Unfortunately, the only material which was corrosion stable under these conditions was tantalum. It would be logic to expect similar results at 200°C in KH_2PO_4.

Electrochemical behavior of Pt and Au was already studied in the potassium dihydrogen sulfate melt in argon atmosphere at 265°C. It was found that the electrochemical stability window for the Pt electrode was 1.05 V with the hydrogen evolution reaction as the cathodic limit and the oxygen evolution reaction as the anodic limit. It has been also shown that gold is corrosion unstable at positive polarization.

Recently, we have studied the thermal behavior of molten potassium dihydrogen phosphate using differential scanning calorimetry and Raman spectroscopy [5].

It has been shown if the vessel is not pressurized at temperatures higher than ~100°C water tends to evaporate. KH_2PO_4 salts have various applications [6] and recently also the application of the melt as an electrolyte for high temperature water electrolysis was suggested [7]. Upon the melting process, water molecules are considered to participate in the formation of eutectic mixtures among phosphates and other salts, due to reactions such as [8, 9]:

$$2KH_2PO_4 \leftrightarrow K_2H_2P_2O_7 + H_2O \leftrightarrow 2/n\left(KPO_3\right)_n + 2H_2O \, \text{for} \, (n = 1,2,3,\ldots) \quad (1)$$

where the melt loses water by evaporation, starting at ~180°C [10].

Further heating of the system under open atmosphere will inevitably decompose it to the metaphosphate salt $(KPO_3)_n$ and water vapor. The KH_2PO_4 melt binds water via hydrogen bonds [6] and is a proton-conducting electrolyte [4, 6]. In the present work, we therefore tried applying it for water electrolysis since preliminary studies in this connection have shown promising results for the conductivity of several molten KH_2PO_4 salt mixtures containing more or less water and under their own water vapor pressure at 240–320°C temperature range in the [6]. It was shown that the KH_2PO_4 melts have conductivities in the order of ~0.30 S cm^{-1} at ~300°C and thus constitute promising electrolytes for pressurized water electrolysis at elevated temperatures. The melting point of the KH_2PO_4 electrolyte under its own vapor pressure was determined to be 272°C [6], although lower melting point values around ~253°C often have been reported in the literature [4, 11].

There is evidently no true melting point at atmospheric pressure, as fusion is simultaneously accompanied by decomposition due to loss of water, as shown by evolution of gas (water vapor) from the crystals [12].

Transfer from KH_2PO_4 to $(KPO_3)_n$ leads to solidification of the molten salt and therefore makes the electrochemical measurements impossible. Because of the temperature of our experiment and the atmospheric pressure, it is natural to assume that in the present study the electrolyte was molten mixture of KH_2PO_4 and $K_2H_2P_2O_7$.

2. Experimental

2.1. Materials

The chemicals KH_2PO_4, $KHSO_4$ (Sigma-Aldrich, p.a.), and Ag_2SO_4 (Heraeus, 99.9% pure) were used as received.

2.2. Electrode preparation

The gold and platinum wires sealed in Pyrex tubes served as working electrodes (the diameter of the wires was 0.2 and 0.4 mm, respectively). The other metal wires were sealed in alumina tubes with outer and inner diameter 4 and 2 mm, respectively. CC180W coating paste was used for sealing the wires inside the tubes and was provided by CeProTec (Germany). CVD tantalum-coated stainless steel AISI 316L (diameter 1.0 mm) was provided by Tantaline A/S (Denmark). Nickel and niobium wires (diameter 1.0 mm) were provided by Good Fellow Cambridge Limited (England). Both the nickel wire with a purity of 99.98% and hard tempered the niobium wire with a purity of 99.9% were annealed. W, Mo, Ti, and Ta wires with diameter 1 mm were provided by ChemPur GmbH, Germany. The rest of the metal wires were provided by Sigma Aerospace Metals LLC. Depending on the composition of the wires, the diameter varied from 0.5 to 0.7 mm. The working electrode area among all tested materials varied from 0.08 to 0.72 cm^2. A platinum wire spiral served as a counter electrode. The reference electrode was a silver wire placed in a Pyrex cylindrical chamber with a Pyrex grade "3" frit bottom. A melt of $KHSO_4$ saturated with Ag_2SO_4 was used as an electrolyte for the reference electrode. This electrode proved to be reliable during our previous studies [12, 13]. The potential difference between the Ag/Ag_2SO_4 and the normal hydrogen electrode (NHE) is approximately 0.7 V at room temperature [14]. Typical chemical compositions of stainless steels and nickel-based alloys investigated in this work are given in **Table 1**.

Alloy type	Ni	Co	Cr	Mo	W	Fe	Si	Mn	C	Al	Ti	Other	Nb + Ta
AISI 347	9.0–13.0	–	17–19	–	–	Bal.	1.0	2.0	0.08	–	–	–	0.8
AISI 321	9.0–12.0	–	17–19	–	–	Bal.	1.0	2.0	0.08	–	0.4–0.7	–	–
AISI 316L	10.0–13.0	–	16.5–18.5	2.0–2.5	–	Bal.	1.0	2.0	0.03	–	–	N less 0.11	–
Hastelloy®C-276	57	2.5	15.5	16.0	3.75	5.5	0.08	1.0	0.02	–	–	V 0.35	–
Inconel®625	62	1.0	21.5	9.0	–	5.0	0.5	0.5	0.1	0.4	0.4	–	3.5

Table 1. Alloy chemical composition.

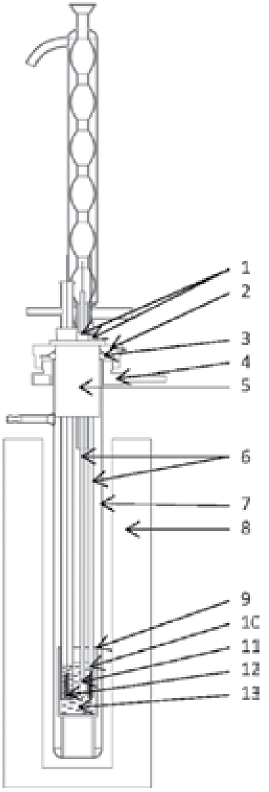

Figure 1. The electrochemical cell: (1) silicon rubber stoppers; (2) stainless steel cover; (3) viton ring; (4) stainless steel lid; (5) teflon lid; (6) ceramic tubes; (7) quartz tube; (8) oven; (9) pyrex glass; (10) counter electrode; (11) working electrode; (12) reference electrode; and (13) electrolyte.

Voltammetric measurements were performed in a three-electrode quartz cell shown in **Figure 1**. The cell was placed in a vertical aluminum-bronze alloy block furnace with temperature regulation within ±1°C. The temperature inside the cell was measured by a chromel-alumel thermocouple in a stainless steel cover. The thermocouple was placed between the walls of the Pyrex glass (position 9 in **Figure 1**) and the quartz tube (position 7 in **Figure 1**).

A condenser was placed above the electrochemical cell so that the escaping water from the melt could be condensed and run back into the melt. Because the amount of water which still escapes from heated KH_2PO_4 is not known, the composition of the melt is given as KH_2PO_4/$K_2H_2P_2O_7$.

All steady-state voltammetric tests were performed at 260°C in air using potentiostat model VersaSTAT 3 and VersaStudio software by Princeton Applied research. For each experiment, polarization was initiated at −1 V vs. Ag/Ag_2SO_4 reference electrode, followed to 1.4 V and then the polarization direction was reversed to the negative direction back to −1 V. The exchange current densities obtained during the backward scan were used to evaluate corrosion current densities. The scan rate was 1 mV/s in All the experiments.

3. Results and discussion

Steady-state voltammetric curves obtained at the Pt electrode are presented in **Figures 2** and **3**. It can be seen that the cathodic limiting reaction (hydrogen evolution reaction) takes place at −0.6 V vs. the Ag/Ag^+ reference electrode and the anodic limiting reaction (oxygen evolution reaction) proceeds at approximately 0.6 V vs. the Ag/Ag^+ reference electrode (**Figure 3**). It can be seen from **Figure 3** that the electrochemical stability window on Pt in the molten $KH_2PO_4/K_2H_2P_2O_7$ at 260°C is approximately 1.67 V.

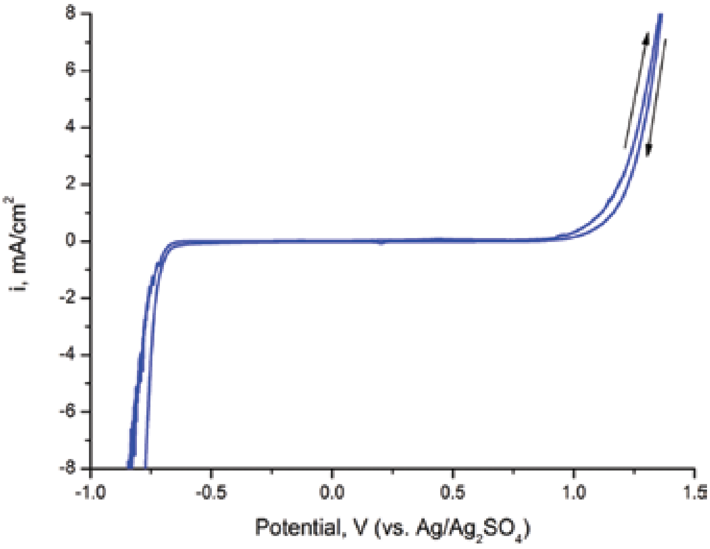

Figure 2. Polarization curve for Pt wire in molten $KH_2PO_4/K_2H_2P_2O_7$ at 260°C. Scan rate 1 mV/s.

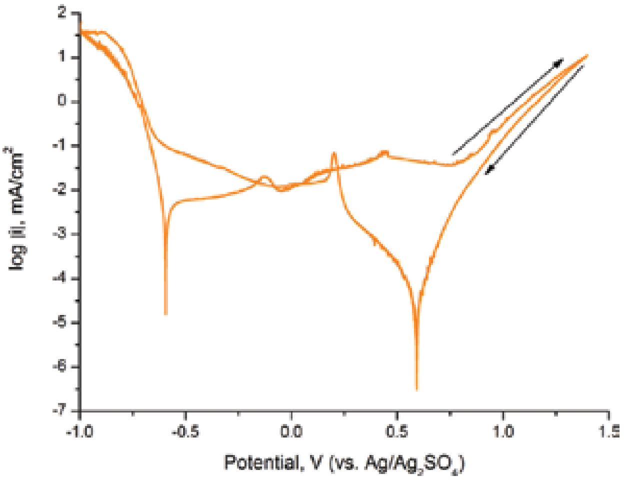

Figure 3. Tafel plot for Pt wire in molten $KH_2PO_4/K_2H_2P_2O_7$ at 260°C. Scan rate 1 mV/s.

It is safe to assume the following limiting reactions:

$$\text{Anode}: 2H_2O \rightarrow O_2 + 4H^+ + 4e^- \tag{2}$$

$$\text{Cathode}: 2H^+ + 2e^- \rightarrow H_2 \tag{3}$$

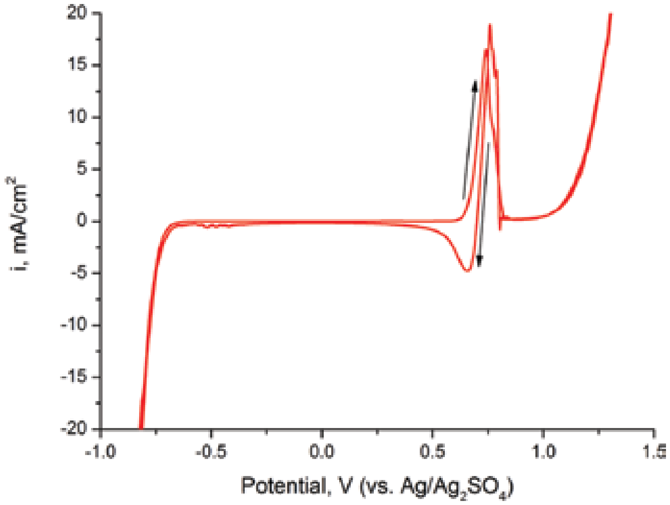

Figure 4. Polarization curve for Au wire in molten $KH_2PO_4/K_2H_2P_2O_7$ at 260°C. Scan rate 1 mV/s.

Moreover, in our recent study [5], electrolysis was performed by passing current through closed ampoules (vacuum sealed quartz glass electrolysis cells with platinum electrodes). The formation of mixtures of hydrogen and oxygen gases as well as water vapor was detected by Raman spectroscopy. In this way, it was demonstrated that water presents in this new type of electrolyte can be electrolyzed at temperatures ~275 to 325°C via the reaction:

$$2H_2O \rightarrow 2H_2 + O_2 \tag{4}$$

The steady-state voltammetric curve obtained at the Au electrode is presented in **Figure 4**. It can be seen that the hydrogen evolution reaction takes place almost at the same potential as at the Pt electrode.

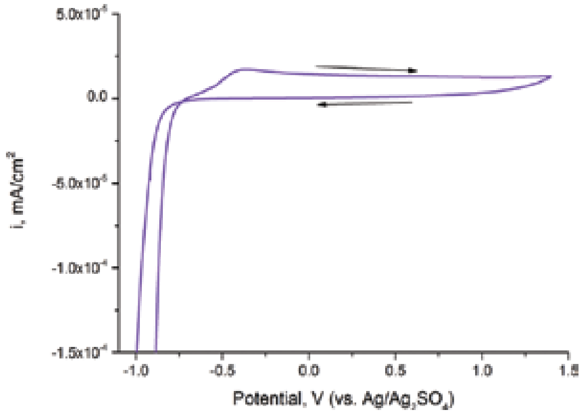

Figure 5. Polarization curve for Ta-CVD coating on AISI 316L wire in molten $KH_2PO_4/K_2H_2P_2O_7$ at 260°C. Scan rate 1 mV/s.

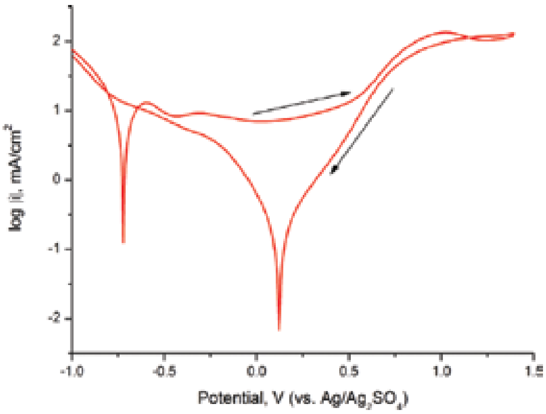

Figure 6. Polarization curve for stainless steel AISI 316L wire in molten $KH_2PO_4/K_2H_2P_2O_7$ at 260°C. Scan rate 1 mV/s.

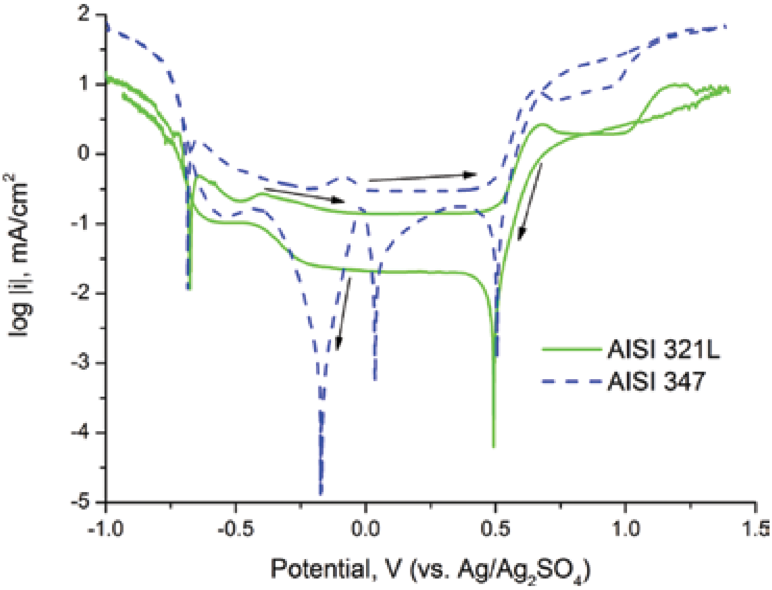

Figure 7. Polarization curves for AISI 321L and AISI 347 wires in molten $KH_2PO_4/K_2H_2P_2O_7$ at 260°C. Scan rate 1 mV/s.

However, like in the molten $KHSO_4$, gold demonstrated corrosion instability at positive polarization [12]. There is a reduction-oxidation reaction at around 0.6 V, which can be assumed to be Au electrochemical oxidation and the Au complex reduction, that is, corrosion of gold in molten $KH_2PO_4/K_2H_2P_2O_7$.

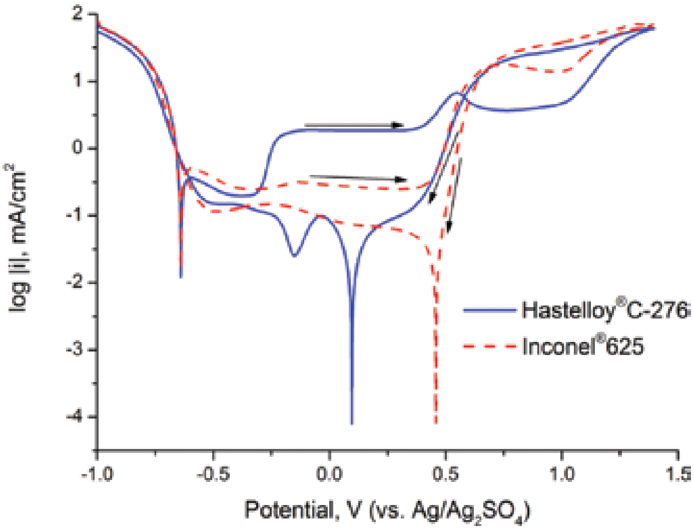

Figure 8. Polarization curves for Hastelloy®C-276 and Inconel®625 wires in molten $KH_2PO_4/K_2H_2P_2O_7$ at 260°C. Scan rate 1 mV/s.

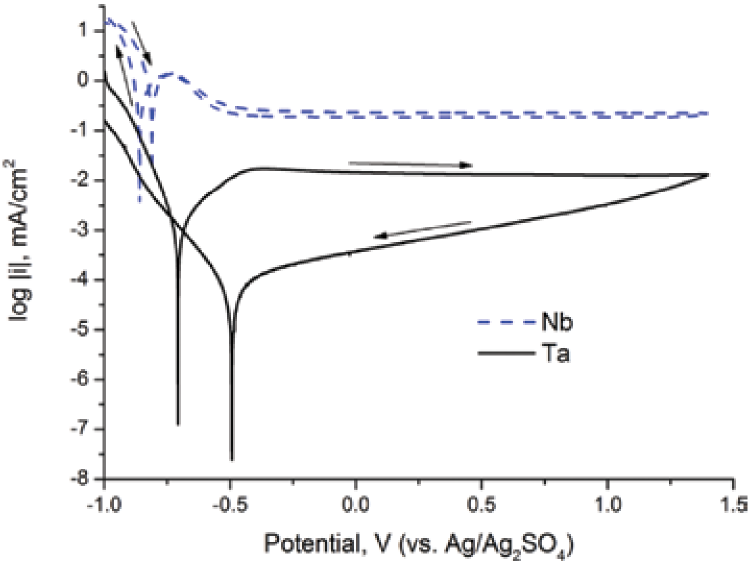

Figure 9. Polarization curves for Nb and Ta wires in molten $KH_2PO_4/K_2H_2P_2O_7$ at 260°C. Scan rate 1 mV/s.

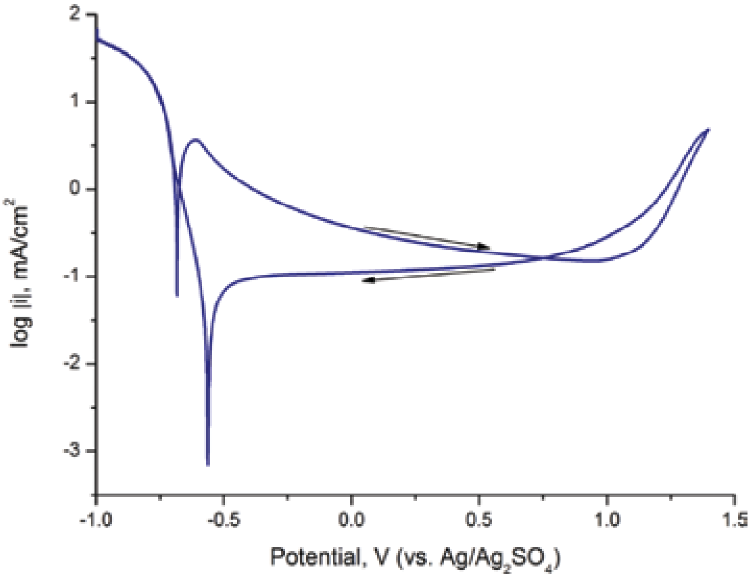

Figure 10. Polarization curve for Ni wire in molten $KH_2PO_4/K_2H_2P_2O_7$ at 260°C. Scan rate 1 mV/s.

The voltammetric data obtained for the stainless steels and the high-nickel alloys are presented in **Figures 5–11** and **Tables 2** and **3**. It can be seen that stainless steels AISI 316 and AISI 347 are corrosion unstable in the studied media (**Figures 6** and **7**), with the AISI 316 undergoing corrosion dissolution at around 0.122 V and the AISI 347 anodically dissolving at −0.04 and

−0.20 V. It is obvious from **Figure 8** that Inconel®625 is more corrosion stable than Hastelloy®C-276. Among the alloys, the behavior is explained by the presence of Ti in the materials. Nb and Ta doping were not effective in preventing corrosion in the alloys. In this study, we did not concentrate on studying particular mechanisms of corrosion in different alloys rather the purpose of this study was to make a review and a selection of materials, which have the potential to be used in this electrolyte.

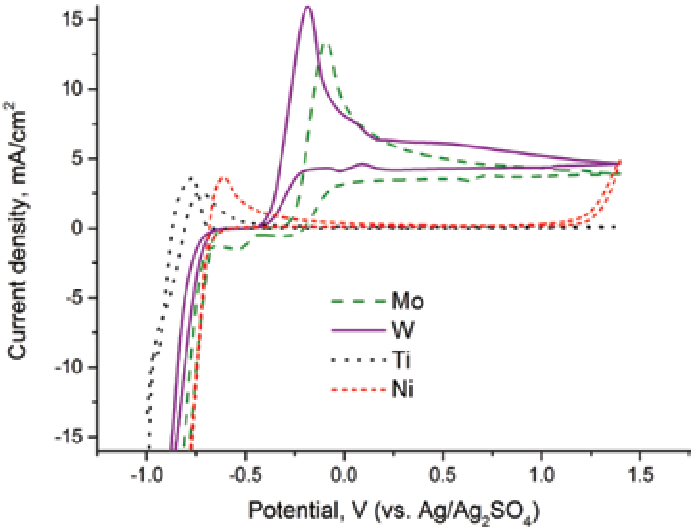

Figure 11. Polarization curves for Ni, W, Ti, and Ni wires in molten $KH_2PO_4/K_2H_2P_2O_7$ at 260°C. Scan rate 1 mV/s.

	Potential vs. Ag/Ag_2SO_4 [mV]	
Sample	**HER (at forward scan)**	**OER (at backward scan)**
SS AISI 316L	−720	–
SS AISI 321	−675	493
SS AISI 347	−685	505
Hastelloy®C-276	−640	–
Inconel®625	−640	457
Pt	−594	594
Au	−597	699
Tantalum	−705	–
Niobium	−810	–
Nickel	−683	–

Table 2. Reversible potentials, calculated from Tafel curves.

It is also clear from **Figure 9** that at the Ta electrode, the hydrogen evolution reaction (HER) takes place at less negative potentials than at the Nb electrode. However, the HER exchange current is much higher at the niobium electrode. Both metals are electrochemically inactive at positive polarization and have high enough corrosion stability.

Sample	E_{corr} **[mV]**	i_{corr} **[mA/cm² (CR, mm/year)]**
SS AISI 316L	122	1.2×10^{-1} (1.4)
SS AISI 347	36	5.0×10^{-2} (0.6)
Hastelloy®C-276	96	3.0×10^{-2} (0.4)

Table 3. Calculated corrosion currents and corrosion rates (from the backward polarization slope).

Both Ta (**Figure 9**) and Ni (**Figure 10**) demonstrate an obvious passivation at positive polarization (hysteresis between scans in the cathodic and anodic directions).

Comparison between the electrochemical behaviors is shown in **Figure 11**. As it has already been mentioned, Ti and Ni demonstrate high corrosion resistance. This fact is in contrast to earlier results which demonstrated poor stability of titanium in hot phosphoric acid [6]. This can be explained by different acidities of two electrolytes: H_3PO_4 and $KH_2PO_4/K_2H_2P_2O_7$. In contrast to Ti and Ni, there is obvious anodic dissolution with passivation in case of Mo and W between −0.5 and 0.0 V. It should be also mentioned that at Mo, W, and Ni HER takes place at a potential close to the HER potential for Pt. Only at the Ti electrode HER proceeds at more negative potentials.

4. Conclusions

Among the studied materials Pt, Ni, Ta, Ti, AISI 321, and Inconel®625 were the most corrosion stable in the molten $KH_2PO_4/K_2H_2P_2O_7$ at 260°. If we compare the corrosion resistance of the stainless steels and their composition (**Table 1**), we can conclude that Ti as an additive, and not Nb or Ta, increase corrosion resistance of the stainless steels in the studied media. Corrosion resistance of the high-nickel alloys shows that the higher the nickel content and the lower the Mo content the higher is the corrosion resistance.

Author details

Aleksey V. Nikiforov*, Irina M. Petrushina and Niels J. Bjerrum

*Address all correspondence to: nava@dtu.dk

DTU Energy, Technical University of Denmark, Kemitorvet, Denmark

References

[1] S. Meyer, A. Nikiforov, I. Petrushina, K. Köhler, E. Christensen, J. Jensen, N. Bjerrum, International Journal of Hydrogen Energy, 40 (7), 2905 (2015).

[2] A.V. Nikiforov, I.M. Petrushina, E. Christensen, A.L. Tomas-Garcia, N.J. Bjerrum, International Journal of Hydrogen Energy, 36, 111 (2011).

[3] A.V. Nikiforov, A.L. Tomas Garcia, I.M. Petrushina, E. Christensen, N.J. Bjerrum, International Journal of Hydrogen Energy, 36, 5797 (2011).

[4] J. Polonsky, I.M. Petrushina, E. Christensen, K. Bouzek, C.B. Prag, J.E.T. Andersen, N.J. Bjerrum, International Journal of Hydrogen Energy, 37, 2173 (2012).

[5] R. Berg, A. Nikiforov, I. Petrushina, N. Bjerrum, Applied Energy, 2016, submitted.

[6] O. Ulleberg, T. Nakken, A. Ete, International Journal of Hydrogen Energy, 35, 1841 (2010).

[7] P. Millet, N. Mbemba, S.A. Grigoriev, V.N. Fateev, A. Aukauloo, C. Etiévant, International Journal of Hydrogen Energy, 36, 4134 (2011).

[8] A. Hermann, T. Chaudhuri, P. Spagnol, International Journal of Hydrogen Energy, 30, 1297 (2005).

[9] D. Labou, E. Slavcheva, U. Schnakenberg, S. Neophytides, Journal of Power Sources, 185, 1073 (2008).

[10] Q. Li, J.O. Jensen, R.F. Savinell, N.J. Bjerrum, Progress in Polymer Science, 34, 449–477 (2009).

[11] T. Uda, S.M. Haile, Electrochemical and Solid-State Letters, 8, A245 (2005).

[12] I.M. Petrushina, N.J. Bjerrum, R.W. Berg, F. Cappeln, Journal of the Electrochemical Society, 144, 532 (1997).

[13] N.J. Bjerrum, I.M. Petrushina, R.W. Berg, Journal of the Electrochemical Society, 142, 1806 (1995).

[14] L Meites, ed., Handbook of Analytical Chemistry, McGraw Hill, NY (1963). Section 5.

High-Temperature Oxidation of Metals

Sneha Samal

Additional information is available at the end of the chapter

http://dx.doi.org/10.5772/63000

Abstract

This chapter explains the brief understanding of the high-temperature oxidation of pure metals such as iron, copper and zinc. Effect of crystal structure from fcc to bcc and hcp on the role of high-temperature oxidation is described briefly. Simultaneously, the effect of grain size of these metals and grain boundary displacement during oxidation process are described very clearly. The combined effect of crystal structure and grain size on the formation of oxide scale is studied in depth understanding with support from the literature search. The aim of this chapter is to explain the mechanism and experimental evidence for the high-temperature oxidation of pure metals.

Keywords: oxidation, pure metal, high temperature, crystal structure, grain size

1. Introduction

Generally, most of the metals used in common application technologies undergo deterioration on exposure to weather condition with time. Consequently, most of the metals are subject to corrosion either at room temperature or at high-temperature ranges [1]. High-temperature corrosion issues deal with energy conversion by turbines, nuclear power, solid oxide fuel cells and high-temperature thermoelectric system [2]. In conventional coal-fired power plants, combustion process is used to heat water to produce steam and that powers turbine to generate electricity. The fireside and steam side of chromia-forming ferritic steels used for the heater tubes face problems of high-corrosion system [3]. The increased temperature and high-steam contents will result in rapid material degradation, and there is a need for high-temperature alloys. The gas-fired turbines at high temperature are limited due to rapid diffusion and oxidation rates. The investigation is carried out for high-temperature materials to increase efficiencies and lower emissions. Similarly, nuclear power plants use fossil for generation of thermal energy that is used in heat-pressurized water [4]. The use of high-temperature materials and its behavior towards corrosion process are subject of interest. The metallic materials used in nuclear metallic materials face the corrosion such as stress corrosion cracking (SCC), irradiation-assisted cracking corrosion (IASCC), environmentally assisted cracking (EAC) and intergranular cracking (IGA) [5]. The rate of corrosion varies widely from slower to faster degree depending on the type of material. The examples of such type are iron rusts at room temperature and deteriorate faster than nickel and chromium that are attacked slowly with time. The surface layer that results due to oxidation determines nature of corrosion rate on the metal and has a strong effect on the material [6].

The high-temperature oxidation of metals always attracts attention from the readers and researchers community as the enthusiastic subject of investigation. This area covers both theoretical predication and satisfactory subject of investigation based on the various combined areas such as metallurgical, chemical and physical discipline with thermodynamic predication [7]. Recently, a set of mechanics data available on mass transport through oxide scales during oxidation, evaporation of oxide species, the role of mechanical stress on oxide scales and the important relationships between metal elements, microstructure and oxidation. Accordingly, such information is obtained virtually prior to oxidation to obtain the physical and chemical reaction of metal species at high temperature [8].

The understanding of the oxidation phenomena and the mechanism behind the reaction species for the formation of oxide scales and its role for the formation of various layers of oxide scale on the metal were discussed. The role of crystal structure of pure metals plays the viable role in the formation of oxide scale [9]. Effect of grain boundary determines the formation of oxide scale and rate of oxidation during high-temperature oxidation scale [10]. The main purpose of the chapter is an introduction to fundamental as well as experimental investigation of interaction of reactive species such as oxygen as the component usually metals such as high temperature. The rate of corrosion depends on the nature of reaction products. The rate of reaction is controlled by reactants through the solid layers. The rate of formation of oxide layers on metals is accordingly [11]

$$M + O_2 = MO_2 \tag{1}$$

The extent of reaction determines the amount of metal consumed, the amount of oxygen used and the amount of product formed during oxidation process. There are several rate laws that apply to determine the oxidation rates such as linear, parabolic and logarithmic rates. The linear law is based on the surface reaction step towards the reactive gases of the environment. It is independent of the time of the reaction. However, the parabolic law depends on inversely proportional to square root of time and is obeyed when diffusion through scale is rate determining steps [12]. The logarithmic law is applicable to the very thin oxide films in the range of 2–4 nm [13].

Discontinuous method is the way to measure the weight of the sample within an interval of the time on exposure to high temperature. Every interval of certain time samples needs to be removed from the high-temperature reactive zone removed the oxide scales from the surface and weighed effectively [14]. Assessment of the extent of reaction is carried out in a simple way either by observing the mass gain of the oxidized samples that is the mass of oxygen taken into scale or by observing the mass loss of the base sample which is equivalent to the mass gain by the oxide scale. The change in specimen dimension is also observed during high-temperature oxidation. The disadvantage of this method is the many specimens are needed to study the reaction kinetics and progress of the reaction is not continuous [12]. On the other hand, this method was very simple and the apparatus required is very simple. Also at each individual point, metallographic examination of each data point is evaluated.

There are various ways to examine and analyze the surface of oxidized samples from the scale towards the base of the material. The methods are classified into two broad categories: (i) from the basic sample mounting to preparation and (ii) then examination using various techniques towards the final stage. Generally, the samples were mounted on the epoxy resin, and then polished using diamond grinding to observe the samples' microstructures and scale thickness and ion transportation from scale towards base of the pure metal. As the epoxy method is very easy, simple and convenient way to examine the scale and the base of the sample. The polished specimens may be examined using conventional optical microscopy for the microstructures, and the elements analyzed can be carried out using scanning electron microscope. Etching is followed on samples after metallographic preparations. Optical microscope is the simplest technique available to look the optical images of the metals before and after oxidation. To know better in microstructure and element of oxides present in oxidized scale and also migration of ions towards base, scanning electron microscopy with energy dispersive X-ray is the best way to know all the experimental parameters that control the oxidation rate of the material [13]. The specific band energy and band states also can be determined on oxidized scales and base of the materials. X-ray diffraction techniques also can be used to determine the corresponding phases of oxide group on the oxidized scale of the pure metal [14]. A depth understanding of high-temperature corrosion of pre metals is quiet necessary as the alloys in multicomponent form makes the reaction process more complex in nature. The sample like pure metal is the beginning stage and simplest way of understanding the reaction kinetics and nature of reaction during high temperature in gaseous phase. The role of temperature and duration of oxidation play the crucial role in formation of oxide layers on the surface of pure metals.

2. Mechanism of oxidation

Transport mechanism of ions and electrons during the oxidation of pure metals is well explained by Wagner's theory of oxidation [15]. According to Wagner's theory, oxidation rate is controlled by partial ionic and electronic conductivities of oxides and their dependence on the chemical potential of the metal or oxygen in the oxide. According to Kofstad [16], the defect structure of oxides plays the important role in oxidation rate of metal. The consideration of the reaction is

$$M(s) + \frac{1}{2}O_2(g) = MO(s) \tag{2}$$

It is obvious that the solid reaction product MO will separate the two reactants as shown in **Scheme 1**.

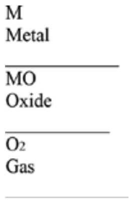

Scheme 1. Metal (M) and reaction phase (O_2) through oxide layer (MO).

In order to proceed the further reaction, one of the reactants either metal or gas (O_2) must penetrate through the oxide scale interface to reach either site of the reactant species. This mechanism of penetration of reactants through oxide layer plays the important role in formation of sublayers in high-temperature oxidation process. Since all metal oxides are ionic in nature, the possibility of transport of neutral metal through the interface is not feasible. Transport of ions through ionic solid is well explained by several mechanisms that belong to the stoichiometric crystal structure or nonstoichiometric crystal one. There are two types of defects that predominate the mobility of ions such as Schottky and Frenkel defects concept [17]. In Schottky defects, ionic vacancies are transported by both the concentration of anionic and cationic sublattices. However, in Frenkel defects, ionic vacancies are transported mainly by cation vacancies. The cations are free to migrate any direction of cations or interstitial sites (**Figure 1**).

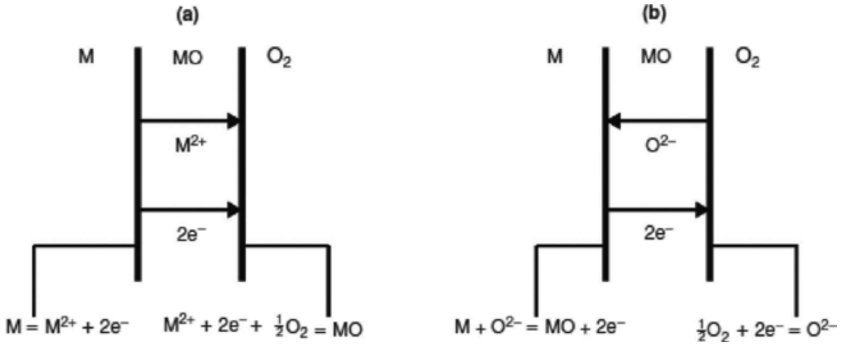

Figure 1. The ions are free movement of oxygen on lattice sites. Interfacial reactions and transport processes for high-temperature oxidation mechanisms (a, cation mobile; and b, anion mobile).

However, both of the reactions could not able to explain the transport mechanism during oxidation state because neither any of the defect structure provides the mechanism for transport of electrons through the interface. In order to explain both migration of electrons and ions it has to be assumed that oxides that are formed during oxidation are nonstoichiometric compounds [18] (**Figure 2**).

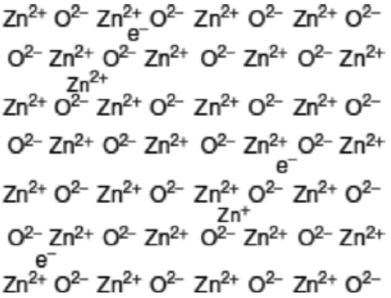

Figure 2. Interstitial cations and excess electrons in ZnO an n-type of metal excess semiconductor.

Nonstoichiometric ionic compounds are classified as semiconductors that may show some positive or negative behaviour. Zinc oxide is the best example of this type of structure. The electric charge is carried out by negative carriers either by metal deficit or metal excess [19].

2.1. Metal excess

The chemical formula for metal excess is $M_{1+\delta}O$, and the best example of it is ZnO. In order to allow extra metal in this compound it is necessary to create existence of interstitial cations with equivalent number of electrons in conduction band [20] (**Figure 3**).

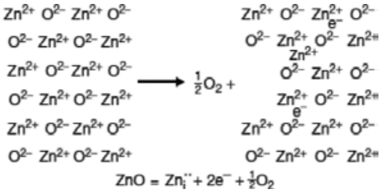

Figure 3. Formation of metal-excess ZnO with excess electrons and interstitial Zn ions from perfect ZnO.

In the above image, both Zn^{+} and Zn^{+2} can create possible space for interstitial sites. Cation conduction can occur over interstitial sites and electric conductions can occur by excess electrons excited into conduction site named as quasi-free electrons. The formation of defect in the ZnO crystal is represented as below [21]

$$ZnO = Z\ddot{n}_i + 2\acute{e} + \frac{1}{2}O_2 \tag{3}$$

The formation of $Z\ddot{n}_i$ is doubly charged Zn interstitial ions and can be written as

$$ZnO = Z\dot{n}_i + 2\acute{e} + \frac{1}{2}O_2 \tag{4}$$

For the formation of $Zn_i^{\circledR}$, singly charged Zn interstitial ions enter the interstitial sites. The final equilibrium constant can be determined as follows

$$C_{Zn_i} = C_{\acute{e}}\alpha \ \mathrm{PO}_2^{\frac{-1}{4}} \tag{5}$$

This explains that defect structure has no role in the mechanism and shows that both the single- and double-charged interstitial cations have a significant role in the mechanism.

More recently, it has been reviewed that significant interstitial solution of zinc occurs in ZnO. Some other researcher also predicts the mechanism by neutral zinc atoms or single-charged interstitial ions. On the basis of oxygen diffusion, the vacancies can occur above by 1000°C. So still there is ambiguity about the mechanism and interpretation of ZnO [22]. Inconsistencies in different mechanisms may arise due to defect structures that are resulted from impurities of the samples especially. So the analysis of pure metal towards high-temperature investigation is a very essential step in concern.

Nonmetal deficit occurs on evaporation of oxygen ions from the species and the electrons enter the conduction band as a result it created vacancy as anion lattice (**Figure 4**). The process is represented as follows [23]

$$O_o = \ddot{V}_o + 2e^- + \frac{1}{2}O_2 \tag{6}$$

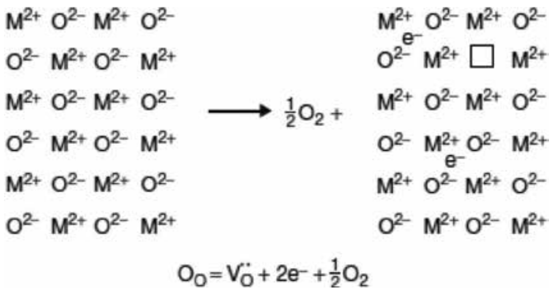

Figure 4. Formation of oxygen deficit MO with oxygen vacancies and excess electrons from perfect MO.

The vacant oxygen site is surrounded by the positive ions represent a site for high positive charge to which free electrons can be attracted. So there is possibility the following reaction takes place as follows

$$\ddot{V}_O + e^- = \dot{V}_O \tag{7}$$

$$\dot{V}_O + e^- = V_O \tag{8}$$

Therefore we have possibilities of single- and double-charged vacancies as well as neutral vacancies.

2.2. Intrinsic semiconductor

The oxide of CuO behaves in this way at 1000°C. This is quiet deviation from the general category. This material is the subject of interest for the study of high-temperature oxidation of metal. Also the lattice structure of Cu belongs to BCC type, which is one of the interesting points on considering various crystal structures into high-temperature oxides and evaluating its role of packing fraction in lattice structure towards the high-temperature oxidation of pure metals (**Figure 5**).

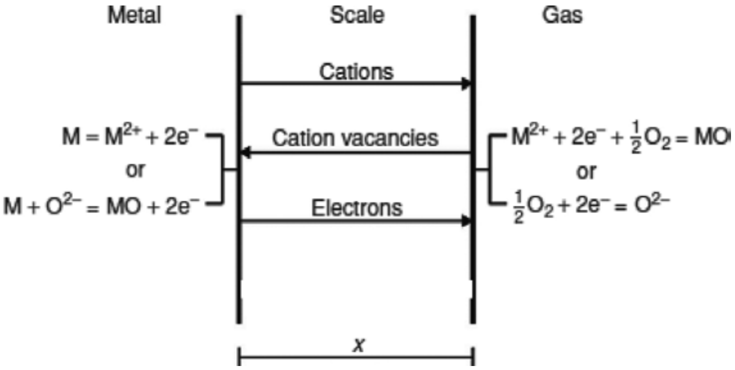

Figure 5. Simplified model for diffusion-controlled oxidation.

Rate of oxidation depends on how the oxidation process proceeds under those conditions where two reactants such as metal and oxygen are separated by an oxidized product. Ionic and electronic transport processes through oxide scale are accompanied by phase boundary reactions, and formation of new oxide species depends on whether cations or anions are transported through oxide layer. Thus the transport mechanisms of oxidation process are varied with oxygen pressure and temperature. Highest oxidation rate is observed in the metal sample where highest defect concentration is possible.

2.3. Point defect model

Point defect model refers to the movement of point defects in an associated electric field. Expansion behaviour of a passive film on a metal surface and breakdown of passive films in terms of mass and charge flux via purpose defects across the semiconductive and defective barrier layers of the passive film. Point defect model has allowed to formulae a set of principles for designing new alloys and has led to the development of a determine for predicting localized corrosion damage functions [24]. Passive film is the defective compound layer that results ion vacancies and chemical element vacancies that were generated and exterminated at the metal–film and film–solution interfaces. However, the bilayer structure of the film compromising a defective or binary compound barrier layer adjacent to the metal and an outer layer that forms by precipitation from reaction of cation species with surroundings introduced metal interstities to the defects in the barrier layer dissolution with passive current reside within the barrier.

2.4. Linear rate law

Under certain conditions, the oxidation of a metal proceeds at a constant rate and is said to obey the 'linear rate law'.

$$x = klt \tag{9}$$

where x is the scale thickness and kl is the linear rate constant.

3. Oxidation of pure metals

3.1. Types of metals and crystal structure

Metals that have useful properties including strength, ductility, thermal and electrical conductivity are used in structural and electrical application. Understanding the structure of the metals can help us understand their properties. Metals are composed of atoms, and atoms are held by strong and delocalized bonds. These bonds are formed by a cloud of valence electrons that are shared by positive metal ions (cations) in a crystal lattice. An actual piece of metal consists of many tiny crystals called grains that join at the grain boundaries. The properties of the metals are influenced by the crystal structures, e.g., the face-centered cubic (fcc) structures. The atomic packing fraction in hcp ($c/a = 1.633$) and fcc structure is 0.74 whereas the bcc crystal structure is less densely packed having atomic packing fraction of 0.68. Exposure of metals to high temperatures in air leads to oxidation of metals and to the formation of oxide scales. Oxidation of pure Fe having bcc is well documented and has led to the classical three layer scale characterization. At high temperatures above 570°C, the innermost layer with the lowest oxygen content is wustite (FeO), with an intermediate magnetite (Fe_3O_4) layer and the most oxygen-rich oxide hematite (Fe_2O_3) next to the gas phase. At temperature of 570°C diffusion transports phenomena occurs as a result, the wustite phase does not form and only the magnetite and hematite layers are seen in scale and the rate of scaling is correspondingly low in the absence of wustite.

However the oxide scales formed in the case of copper (fcc) consist of an outer copper oxide layer and inner porous layer. The copper oxide may be single-phase CuO or a two-phase (CuO + Cu_2O). At the lower part of the temperature range the oxidation kinetics and oxide morphology depend strongly upon the formation of CuO. The CuO layer is nonprotective and further oxidation Cu_2O is converted to CuO. The formation of CuO changes the oxidation behavior from being approximately parabolic growth to having a break way like oxidation behavior. At ambient partial pressure of CuO, the oxide scale consists solely of Cu_2O, while at higher oxygen pressures the scale consist of Cu_2O (99%) + CuO and the rate constant is independent of oxygen pressure.

Zinc (hcp) forms ZnO and therefore a single phase, single-layered scale is expected when pure zinc is oxidized.

Also with addition to crystal structure, grain shape, size, and grain boundary diffusion on high temperature play the influential role on oxidation of pure metals. In this section we consider pure Cu, Fe and Zn at the subject of interest from the range of pure metals because of different crystal structures and the general application in industrial point of interest.

4. Experimental conditions and reaction temperature

Three commercially pure metals such as iron, copper and zinc having different crystal structures were taken into consideration [27]. The specimens are cut in rectangular dimension of $50 \times 25 \times 6$ mm^3. The specimens are ground and polished up to 1 μm and subsequently etched to reveal the microstructure. The prepared specimens were examined using optical microscope for the microstructures of the preoxidized specimen. The specimens are further ground, polished and subsequently cleaned in acetone for oxidation species. The polished and cleaned specimens are placed in the central zone of the furnace for oxidation at dry air. In order to study the effect of crystal structures of metals, the samples are oxidized 2/3 of the melting point of metals. The oxidation tests are carried out for the period of 10 hours at temperatures of 1023°C, 723°C and 279°C for iron (bcc), copper (fcc) and zinc (hcp) metal, respectively [27]. The weight gain of the oxidized specimens was measured by means of an electronic microbalance with an accuracy of ±0.01 mg, and corrosion rates were calculated. The external scales of oxidized specimens were characterized by scanning electron microscope and energy dispersive spectroscopy.

5. Results

The optical microstructure images of the preoxidized specimens of zinc, copper and iron are shown in **Figure 6**. The microstructure of zinc consists of coarse grains along with mechanical

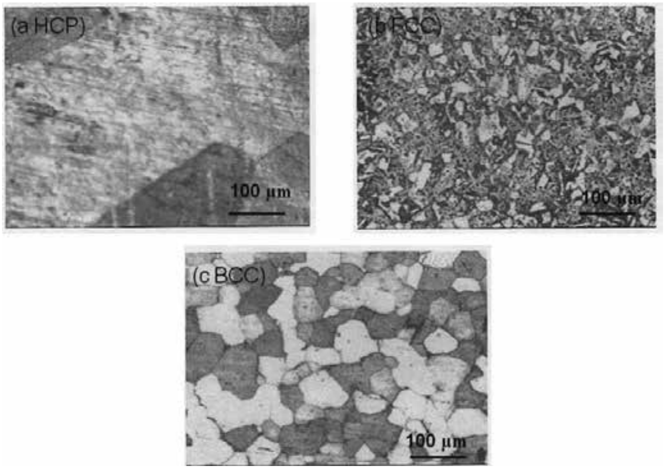

Figure 6. Optical micrographs of pure (a) Zn, (b) Cu and (c) Fe.

twins, whereas the microstructure of copper shows polyhedral grains with annealing twins. The microstructure of pure iron shows polyhedral grains of ferrite with very distinct and sharp boundaries. The oxidation rate of pure iron having bcc crystal structure is found to be 13.37 × 10^{-3} g cm^{-2} h^{-1}. However, the oxidation rates of copper and zinc are found to be 0.69 × 10^{-3} g cm^{-2} h^{-1} and 0.05 × 10^{-3} g cm^{-2} h^{-1}, respectively (**Figure 7**). The change in oxidation rate from bcc metal to fcc and hcp metals can be attributed to the increase in atomic packing fraction of different crystal structures and also the progressive decrease in the free energy of formation of iron, copper and zinc oxidation, respectively. The trend of oxidation rate from zinc towards iron may be both a combination of cations as well as anionic mobility. A marginal difference in thickness and structural changes in grain size and shape has been observed in the Cu_2O inner layer compared with CuO outer layer (**Figures 8** and **9**).

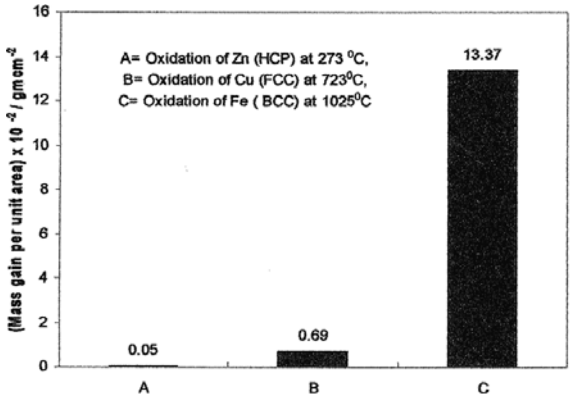

Figure 7. Oxidation behavior of Zn, Cu and Fe at high temperature (T=2/3 m.p.) in=21.27 kPa for 10 hours.

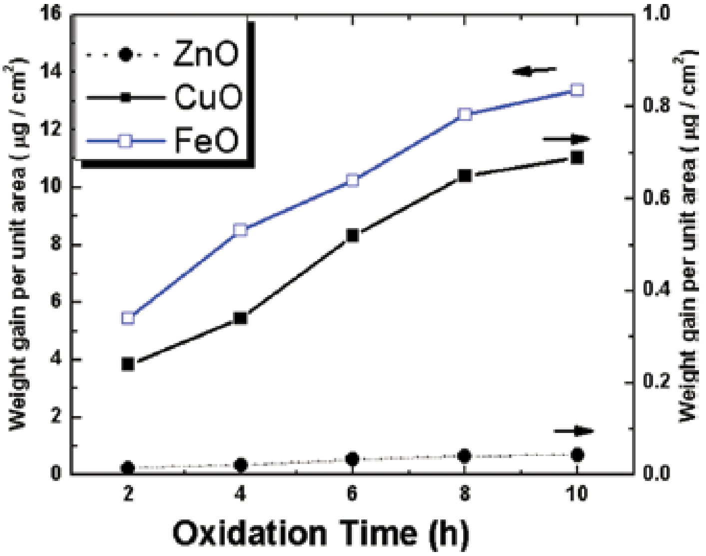

Figure 8. Oxidation kinetics of Fe, Cu and Zn layers under 21.27 kPa O_2 at 1023 K, 723 K and 279 K.

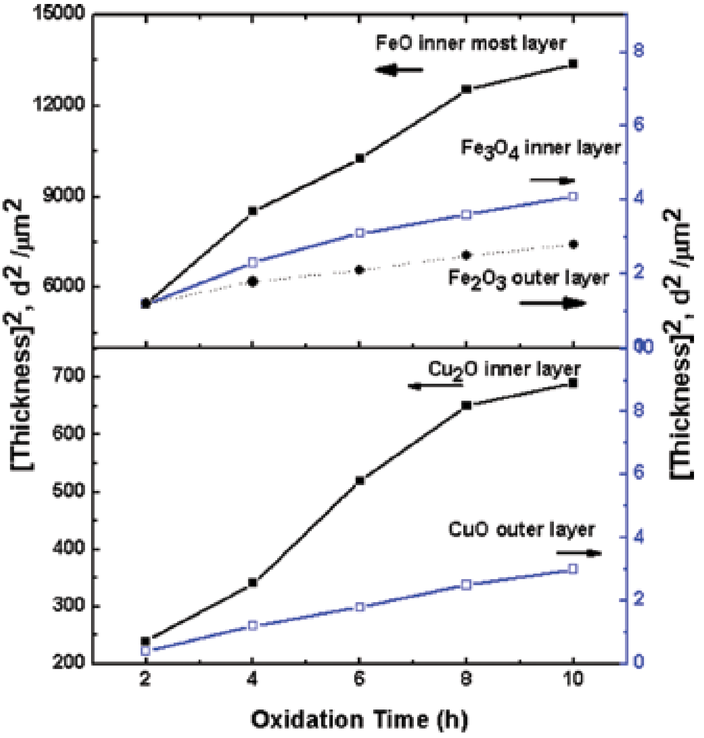

Figure 9. Scale of the oxidation layer of Fe and Cu layers under 21.27 kPa O_2 at 1023 K and 723 K for 10 h.

The external scales of all the three samples are examined using SEM and EDS. The SEM micrograph of top oxide scale of pure iron and the corresponding EDX are shown in **Figure 10**. The top oxide scale on cooling to room temperature is found to be ballooned and separated from the metal substrate without any appearance of cracks. The observed ballooning of the scale can be attributed to the compressive stress generated within the scale as a result of higher volume of iron oxide compared to that of iron. The lower scale of the pure iron after unbounding from the base metal shows the creation of the holes and elongated cracks on the surface with irregular thickness of the surface morphology. Oxidized scale shows the rough microstructure with valleys around grain boundary. This indicates that the transport of cations along grain boundaries is still the dominant mechanism for outer scale growth. According to elemental composition, the outer layer consists of maximum oxygen than the inner layers with minimum amount at base (O_2) content (upper surface area > lower surface area > base of the substrate). A common cause of such stress is the difference in thermal expansion coefficient of the oxide and metal. Oxide layer has low thermal expansion coefficient than the metal base component. If the corrosion rate is sufficiently low, then the oxide layer is always less than the critical thickness.

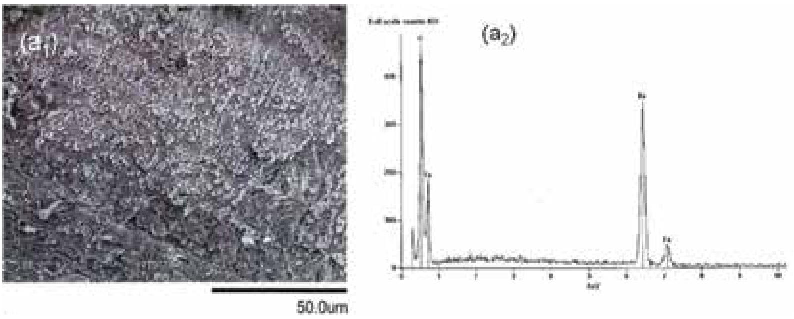

Figure 10. (a1) SEM micrograph of oxide scale on the substrate of pure iron after removal of top scale and (a2) corresponding EDX.

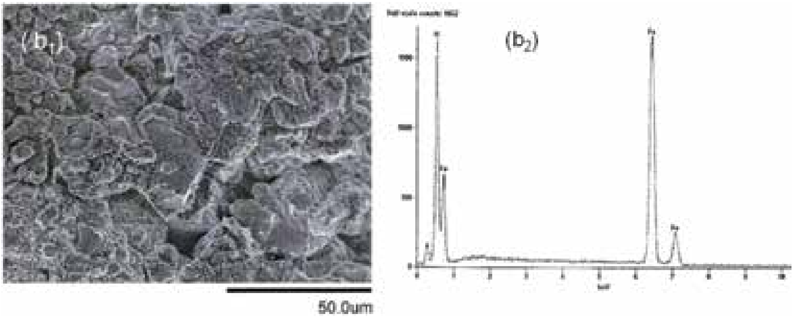

Figure 11. (b1) SEM micrographs of lower surface of the top scale of pure iron after detached from the base metal and (b2) corresponding EDX.

In the case of zinc the oxide layer is very thin and strongly adheres to the base metal with thickness less than 1 μm (**Figure 11**). In the case of pure copper the scale does not spall but exhibits needle shape grains having different orientation on the top surface of the oxide scale. The pores are observed in the medium layer of the copper scale due to nonuniform thickness of layers that obey the parabolic rate law (**Figure 12**).

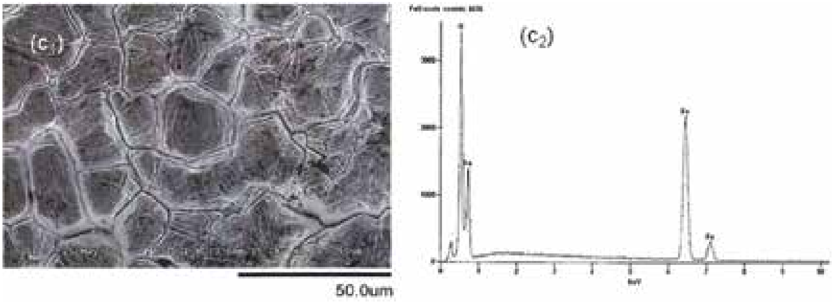

Figure 12. (c1) SEM micrograph of top oxide scale formed over pure iron (c2) and corresponding EDX.

6. Discussion on the mechanism of high-temperature oxidation

The degree of oxidation inhibited by voids depends on their continuity and location of oxide and their effective elimination by plastic deformation (**Figure 13**).

Oxidation rate decreases with decrease in grain size for pure iron and copper. As a result the stress caused by the conversion of Fe_3O_4 to Fe_2O_3 could create inner crystalline microcracks that simulate plastic behavior under differential contraction as well as diffusion paths during grain boundary diffusion areas (**Figure 13**). Grain shape and size highly influence the oxidation rate of pure metals at high temperature. Oxidation rate decreases with decrease in grain size up to a certain extent. Reaction and diffusion of metals in air influence the reaction kinetics of the oxidized layer of the metal (**Figure 14**). Kinetics of oxidation depends on both the metal and oxygen transport inward as well as outward diffusion in scale (**Figure 15**). The mechanism of compressive behavior of oxide scales on the metal surface that develop due to stresses and inner displacement that develops during oxidation process of metal (**Figure 16**). The oxidized grain size for Cu in comparison to grain boundary to bulk is shown in **Figure 17**. Interfacial reaction and transport mechanism of high-temperature oxidation through the oxide interface are shown in **Figure 18**. **Figure 19** displays the oxidized grain size of copper metal as a function of distance on oxide/metal interface. The illustration of grain boundary sliding and creation of cavity is shown in **Figure 20**. **Table 1** shows the summary of mechanism of surface-controlled oxidation mechanism. Finally, **Figure 21** explains graphical schematic presentation of oxidized scale on the pure metals such as Fe, Cu and Zn on high-temperature oxidation. The basic understanding on the influence of grain size and shape on the oxidation will derive knowledge for alloys' oxidation.

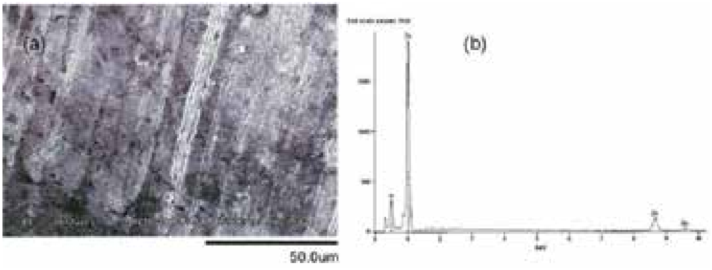

Figure 13. SEM micrograph of the top surface of the oxide scale of pure zinc (b) and corresponding EDX.

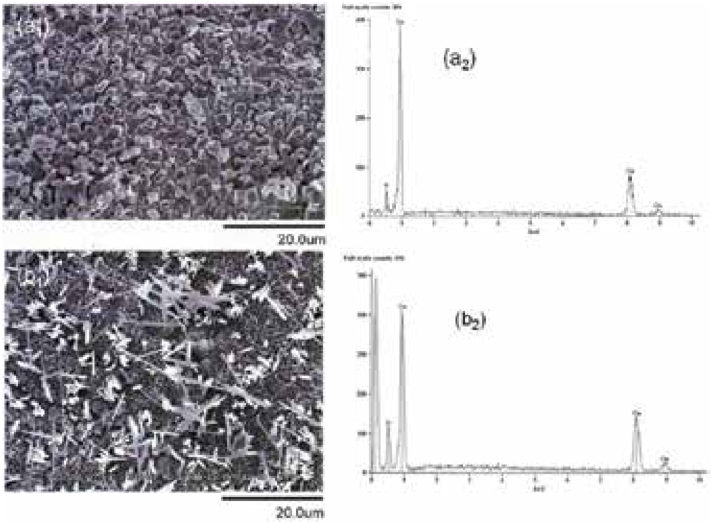

Figure 14. (a1) SEM micrograph of the top surface of the oxide scale of pure copper (a2) corresponding EDX. (b1) SEM micrograph of the inner oxide scale of copper (b2) corresponding EDX.

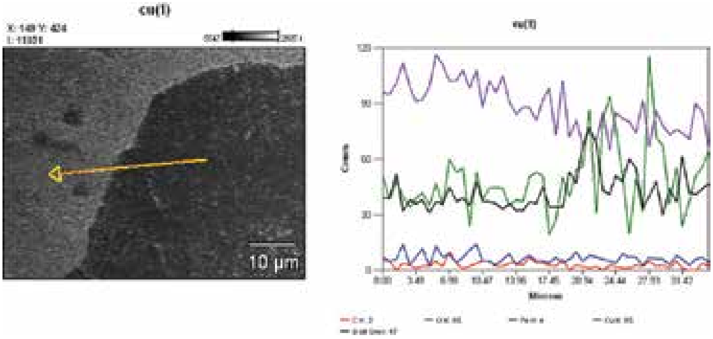

Figure 15. Line analysis of the oxide scale towards the base of the copper metal.

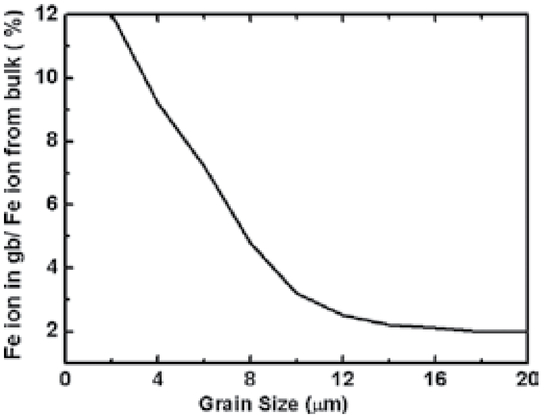

Figure 16. Oxidized grain size as a function of Fe ion in gb/Fe ion from bulk (pct).

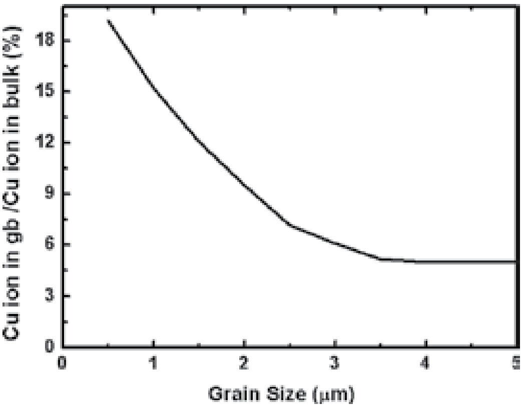

Figure 17. Oxidized grain size as a function of Cu ion in gb/Cu ion from bulk (pct).

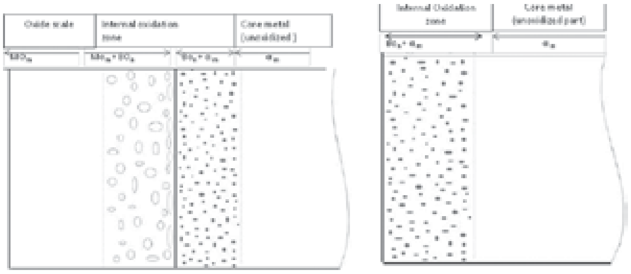

Schematic diagram of the oxidation morphology of pure metal Iron

Schematic diagram of the oxidation morphology of pure metal copper

Figure 18. Interfacial reaction and transport processes for high-temperature oxidation mechanism.

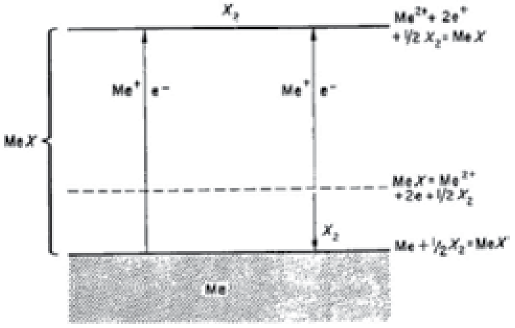

Schematic process occurs during formation of double layer mono phase scale on a metal (Mrowec 1967).

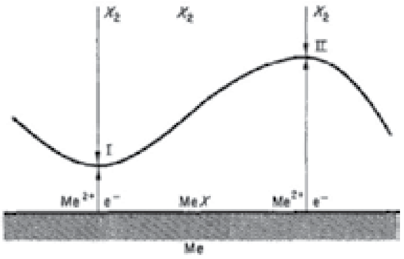

Mechanism of formation of the intial layer of the reaction product on metal surface (sinusodial curve).

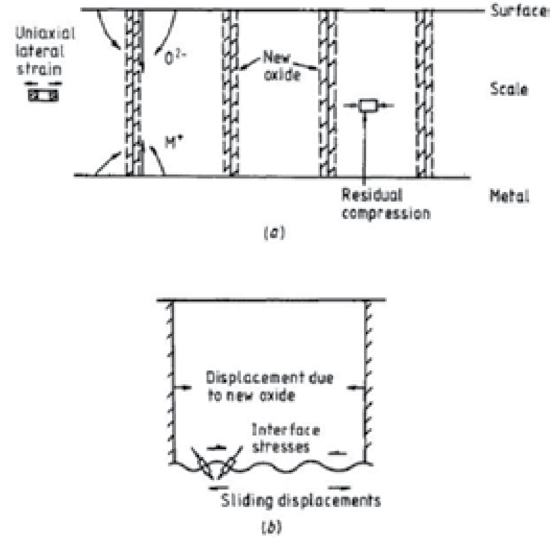

Figure 19. (a1) Compressive constraints on new oxide displacement at grain boundaries within the bulk scale. (b) The interface sliding displacement associated with oxide formation within the bulk scale (Evan et al.).

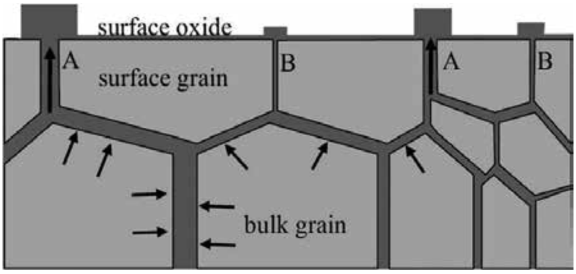

(c) Thickness of the grain boundary and grain size induces the mass transfer for the formation of oxide scale.

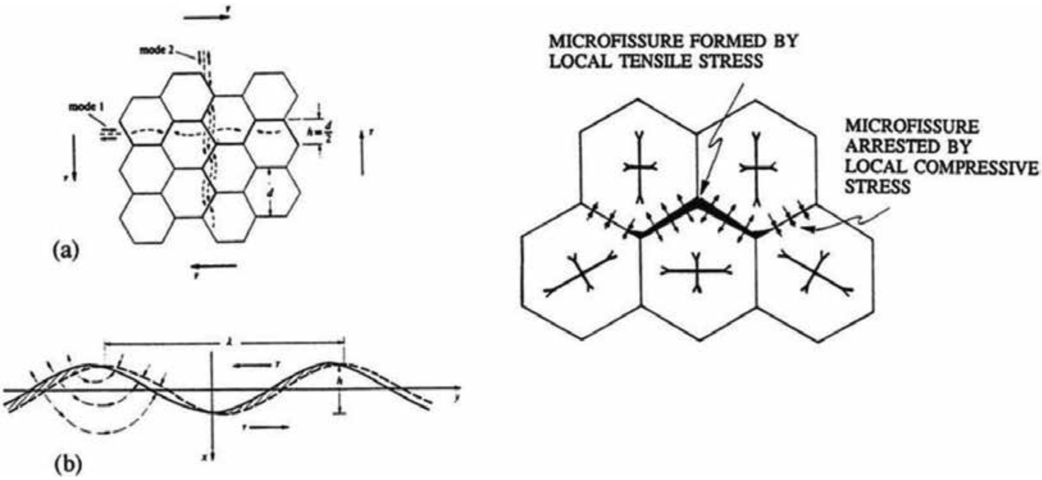

Figure 20. (a) Illustration of the grain boundary sliding, (b) the formation of cavity.

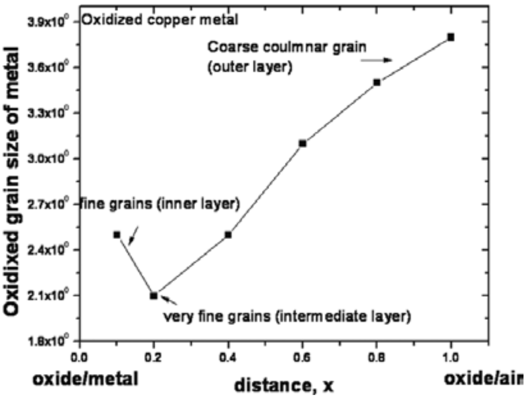

Figure 20. Oxidized grain size of the copper metal as a function of distance from the oxide/metal interface.

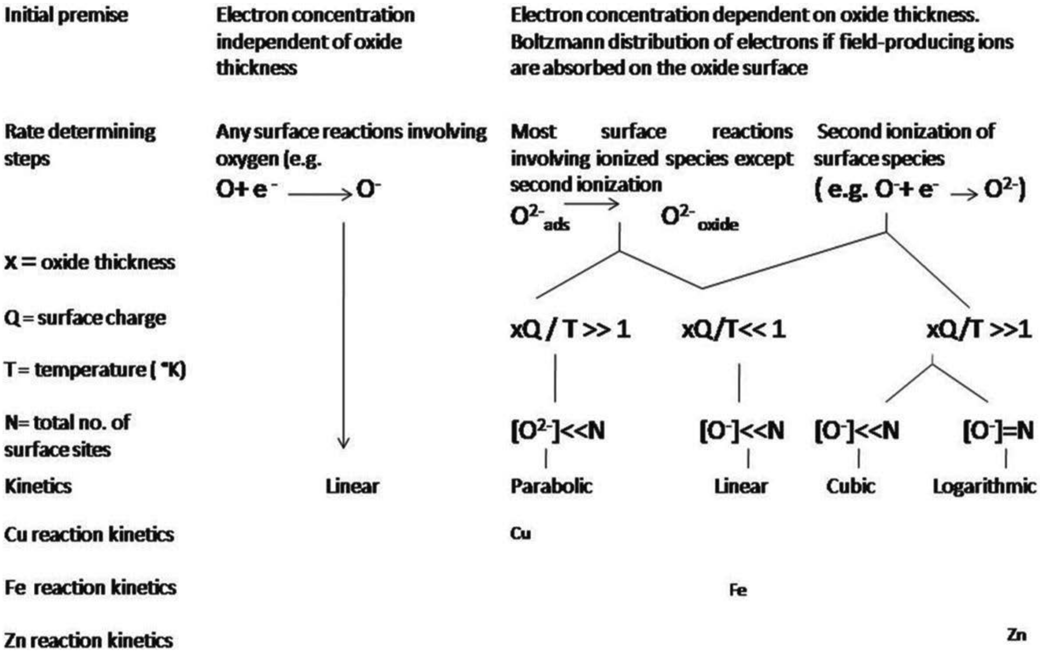

Initial premise: Electron concentration independent of oxide thickness | Electron concentration dependent on oxide thickness. Boltzmann distribution of electrons if field-producing ions are absorbed on the oxide surface

Rate determining steps: Any surface reactions involving oxygen (e.g. $O + e^- \longrightarrow O^-$ | Most surface reactions involving ionized species except second ionization $O^{2-}_{ads} \xrightarrow{} O^{2-}_{oxide}$ | Second ionization of surface species (e.g. $O^- + e^- \rightarrow O^{2-}$)

x = oxide thickness

Q = surface charge: $xQ/T >> 1$ | $xQ/T << 1$ | $xQ/T >> 1$

T = temperature (°K)

N = total no. of surface sites: $[O^{2-}] << N$ | $[O^-] << N$ | $[O^-] << N$ | $[O^-] = N$

Kinetics: Linear | Parabolic | Linear | Cubic | Logarithmic

Cu reaction kinetics: Cu (Parabolic)

Fe reaction kinetics: Fe (Linear)

Zn reaction kinetics: Zn (Logarithmic)

Table 1. Summary of the description of surface-controlled oxidation.

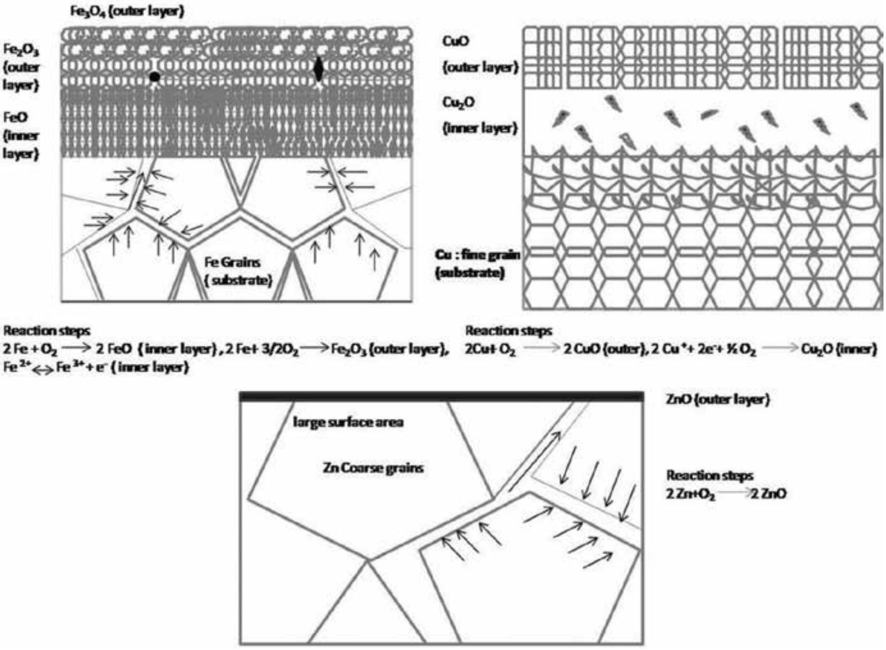

Figure 21. Schematic presentation of various oxide layers' formation on three pure metals.

http://dx.doi.org/10.5772/63000

7. Application of nanotechnology for the resistance of high-temperature corrosion in metals

Nanotechnology coating is emerged as the resistance to high-temperature corrosion in various metals from the last decade. Novel active anticorrosive pigments that consist of metal particles coated with a very thin layer of semiconducting titanium dioxide to protect the surface of metal at high-temperature operation. Nano TiO_2 is contributed towards the development of high corrosive resistance for materials with hydrophobic characteristics. Some polymer coatings such as polypyrrole nanocomposites with iron oxide Fe_3O_4 are used in the corrosion protection of iron metal [25]. Also self-assembled nano phase coating is used for resistance of corrosion activity and promotes adhesion of inter surface bonding between metal and coating process [26]. Nano TiO_2 coating is used because it performs multifunctional activities such as anti UV radiation and anti-bacterial self-cleaning paints on the materials.

8. Conclusion

High-temperature oxidation of metals were studied based on the parameters such as specific crystal structure of metal, grain size and grain morphology of three different metals such as Cu, Fe and Zn. Fe and Cu show the formation of multilayers that obey the parabolic law however Zn metal deviates from the law. Scale morphology depends upon the initial crystal structure of the pure metals that leads towards the packing fraction of the material in lattice stage. Oxidation kinetics is also highly influenced by the structure of metals. The rate of oxidation decreased to a greater extent with change in the crystal structure from bcc → fcc → hcp. Change in crystal structure not only improved the oxidation resistance but also the scale adherence from bcc to hcp.

Acknowledgements

Authors would like to thank Mr Sanjeeb Kumar Samal for his contribution regarding literature search for preparation of this article. Author is presently the assistant professor at Technical University of Liberec also with collaboration of this work with VUTs a.s. (research center) in Czech Republic.

Author details

Sneha Samal

Address all correspondence to: sneha.manjaree.samal@tul.cz

The Centre for the Development of Engineering Research VÚTS, a.s., Liberec, Czech Republic

References

[1] R. E. Hummel. Understanding materials science. Springer-Verlag New York, Inc., USA, 2004, p. 36.

[2] E. Opila. High temperature materials corrosion challenges for energy conversion technologies. The electrochemical Society Interface, Winter 2013, pp. 69–73.

[3] S.C.Kung, Formation of a chromium-carbide conversion coating on silicon carbide , Oxid. Met. 1999, 5,516, pp. 191–203.

[4] F. Cattant, D. Crusset, D. Feron. Corrosion issues in nuclear industry today. Mater. Today 2008, 11, 10.

[5] D. Freon, D. D. Macdonald. Prediction of long term corrosion behavior in nuclear waste system, EFC series 36. Maney/Woodhead, London, 2003.

[6] J. M. Boursier et al. A review of PWSCC, weldability, and thermal ageing of nickel weld metals in PWR primary water. Presented at EPRI International conference on PWSCC of alloy 600, Santa Anna Pubelo, USA, March 2005.

[7] B. Riou et al. Issues in reactor pressure vessel materials. 2nd International Topical Meeting on High Temperature Reactor Technology, 2004.

[8] A.Zahs, M.Spiegel, H.Grabhe, Chloridation and oxidation of iron, chromium, nickel and their alloys in chloridizing and oxidizing atmospheres at 400-700 °C, Corr. Sc. 2000, 42, 6, pp.1093–1122.

[9] G. S. Was. Fundamentals of Radiation Materials Science: Metals and alloys. Springer Verlag, 2007, The materials information society. ASM international, Materials Park, OH 44073-0002, ISBN: 978-3-540-49471-3.

[10] M. Rühle, U. Salzberger and E.Schumann. High resolution transmission microscopy of metal/metal oxide interfaces. In microscopy of oxidation 2. Eds. S.B.Newcomb and M.J. Bennett, London, Uh, The institute of Materials, 1993, p.2.

[11] D. R. Gaskell. Introduction the thermodynamics of materials, 3rd edn, Taylor and Francis, Washington, DC, 1995.

[12] M. Hillert. The uses of Gibbs free energy–composition diagrams. In Lectures on the Theory of Phase Transformations, 2nd edn., H. I. Aaronson (Ed.), The Minerals, Metals and Materials Society, Warrendale, PA, 1999.

[13] D. M. Smyth. The defect chemistry of metal oxides. Oxford University Press, Oxford, 2000.

[14] R.J.Hussey and M.J.Graham, The influence of reactive-element coatings on the high-temperature oxidation of pure Cr and high Cr content alloys, Oxid. Met. 1996, 46, 3/4, pp. 349–374.

[15] A.S.Khanna. Introduction to high temperature oxidation and corrosion. ASM International.] S.C.Kung, Formation of a chromium-carbide conversion coating on silicon carbide , Oxid. Met. 1999, 5,516, pp. 191-203.ISBN:0-87170-762-4. The materials information society.

[16] C.M.Cotell, G.J.Yurek, R.J.Hussey, D.F.Mitchell, M.J.Graham. The influence of grain boundary segregration of Y in Cr2O3 on the oxidation of metals. 1990, 34,3pp.173–200.

[17] R. A. Perkins, G. H. Meier. Acoustic emission studies of high temperature oxidation. In High Temperature Materials Chemistry, Z. A. Munir, D. Cubicciotti (Eds.), Electrochemical Society, New York, NY, 1983, p. 176.

[18] N.Birks, G.Meier and F.Petit. Introduction to the high temperature oxidation of metals, 2nd eds, The Cambridge university press.

[19] R Mishra, R. Balasubramaniam. Effect of nanocrystalline grain size on the electrochemical and corrosion behaviour of nickel. Corros. Sci., 2004, 46, 3019–3029.

[20] M. Kending, M. Hon, L. Warren. Smart corrosion inhibiting coating. Progr. Org. Coat. 2003, 47, 183–189.

[21] P. Kofstad. High Temperature Corrosion. Elsevier Applied Science Publishers, Ltd, New York, 1988.

[22] H. E. Evans. In Cyclic oxidation of high temperature materials. M. Schutze, W. J. Quadakkers (Eds.), IOM communications, London, 1999, p. 437.

[23] Pin Lu, Engelhardt George R., B. Kursten, D. D. Macdonald. The kinetics of nucleation of metastable pits on metal surfaces: The point defect model and its optimization on data obtained on stainless steel, carbon steel, iron, aluminium, alloy 22. J. Electrochem. Soc.. 2016 163 (5) C156-C163.

[24] V. S. Saji, Joice Thomas. Nanomaterials for corrosion control. Curr. Sci. 2007, 92, 1.

[25] H. S. Nalwa (Ed.). Handbook of nanostructured materials and nanotechnology, Vol. 1, Academic Press, San Diego, 2000.

[26] A. G. Evans, J. W. Hutchinson, and Y. Wei, Interface adhesion: effects of plasticity and segregation, Acta mater. Vol. 47, Nos 15, pp. 4093–4113, 1999.

[27] S Samal and S K Mitra. Influence of grain shape, size , grain boundary diffusion on high-temperature oxidation of pure metal Fe, Cu and Zn. Metall. Mat. Transc. A 2015, 46A, pp. 3324–3332.

Chapter 7

Mechanism of Corrosion and Erosion Resistance of Plasma-Sprayed Nanostructured Coatings

Zaki Ahmad, Asad Ullah Khan, Robina Farooq,
Tahir Saif and Naila Riaz Mastoi

Additional information is available at the end of the chapter

http://dx.doi.org/10.5772/64316

Abstract

There has been a dramatic increase in recent years in a demand for tough, wear-resistant, abrasion, erosion, and corrosion-resistant coatings for petroleum, chemical, aerospace industry, and processes encountering harsh environments such as paper and pulp equipment (the ball valve for high-pressure leaching). Whereas sufficient information on mechanical properties, such as abrasion, wear, and fatigue, has been gathered over the years, work on the resistance of these coatings to erosion and corrosion is seriously lacking. In the work reported, it has been shown that nanostructured TiO_2 coatings offer superior physical and mechanical properties compared to conventional TiO_2 coatings. Three different types of plasma-sprayed titanium dioxide coated samples on mild steel substrate were employed for investigation. The feedstocks used were Sulzer Metco nanopowders designated as AE 9340, AE 9342, and AE 9309. Powder 9340 was a precursor. The corrosion resistance of nanostructured TiO_2 coating was dictated largely by surface structure and morphology. The distribution and geometry of splat lamellae, contents of unmelted nanoparticles, and magnitude of porosity are the important factors that affect corrosion resistance. TiO_2 showed excellent resistance to corrosion in 3% NaCl. The maximum corrosion rate was observed to be 4 mils per year as shown by polarization potential and weight loss studies. The erosion-corrosion resistance of the plasma-sprayed nanostructured titanium dioxide coatings depends largely upon the characteristics of feed powder and its reconstitution. Dense, uniform, and evenly dispersed nanostructured constituents provide a high coating integrity, which offers high resistance to erosion-corrosion. A mechanism of erosion-corrosion is explained in the chapter with a schematic diagram. The findings show that the nanostructured TiO2 coatings offer superior resistance to corrosion, erosion, and environmental degradation.

Keywords: plasma air spray (PAS), nanostructured TiO_2 coating, inter-splat boundaries, fully melted particle zone, erosion corrosion

1. Introduction

Recent years have witnessed an increased demand for erosion-corrosion, wear, and abrasive resistant coatings for harsh environment in industry [1,2]. Thermal spray process of coating has brought a dramatic improvement in the quality of new generation TiO2 nanostructured coatings. A conventional thermal process is illustrated in **Figure 1**.

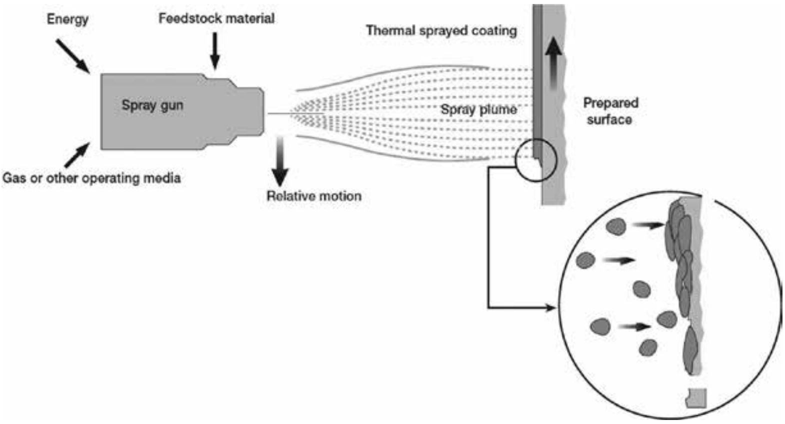

Figure 1. Thermal spray process principle. [Source: An Introduction to Thermal Spray, Issue 4 © 2013 Sulzer Metco].

TiO_2 coatings have been applied in harsh environments, gas sensors, paper and pulp industry, and electronic devices [3]. Thermal spray process has been very successfully used for application of bulk TiO_2 and nanostructured titanium dioxide coatings. A schematic diagram for thermal spray is shown in **Figure 2**. The unmelted particles, porosity, and oxide particles are shown in **Figure 2**. TiO_2 is highly stable, non-toxic, and bio-compatible. It shows a high dielectric constant and exhibits high photocatalytic activity. It is therefore used as an immobile catalyst in photocatalytic reactors [3–5]. It has been reported that nanostructured titanium dioxide coating exhibits a superior resistance to corrosion compared to conventional titanium dioxide coatings. The native oxide film of titanium dioxide (anatase) is about 2–10 nm thick which acts as a barrier for harsh environment. The thin film formed on anatase and rutile titanium dioxide is highly protective. It has been reported that nanostructured TiO_2 coatings offer superior physical and mechanical properties compared to conventional TiO_2 coatings [6]. Bansal et al. have characterized the interfacial microstructure, toughness, and failure modes in "conventional" and the "nano" Al_2O_3-13 wt% TiO_2 plasma-sprayed ceramic coatings [7]. There is evidence to show the advantages exhibited by nanostructured coatings due to their exceptional properties obtained if the crystalline character of the starting material is preserved [7]. The important consideration is to minimize coarsening of particles. Whereas a lot of work has been conducted on the physical and mechanical properties of nano-TiO2 coatings, the work on corrosion and erosion resistance is scarce. Hence, an attempt has been made to fill this gap by evaluating the erosion-corrosion and corrosion resistance of bulk and nanostructured titanium dioxide coatings by different techniques.

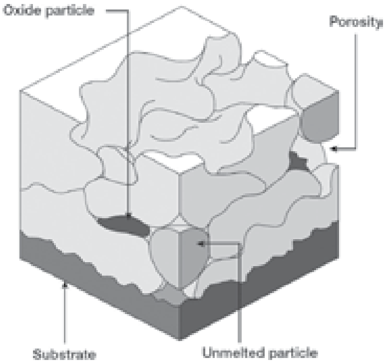

Figure 2. Thermal-sprayed coating schematic diagram. [Source: An Introduction to Thermal Spray, Issue 4 © 2013 Sulzer Metco].

2. Experimental

Investigations were conducted on three different types of titanium dioxide plasma-sprayed samples. These samples were numbered as M102, AE9342, and AE9303 for identification. Sample M102 was prepared from bulk titanium dioxide and plasma sprayed. It was used as a control sample for comparison.

2.1. Nano feedstock

Nano feedstocks obtained from Sulzer Metco are numbered as AE9340, AE9342, and AE9303 for identification. Feedstock AE9340 acted as a precursor. It was spray dried from powder AE9340 by feeding it through a plasma flame. This procedure reduced the volume and increased the density of the powder. Powder AE9303 was made by combination and spray drying technology followed by sintering. The structural features of the powder are shown in **Figures 3–5**.

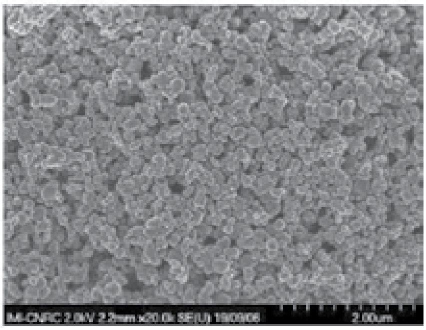

Figure 3. SEM image of spray-dried AE9340 nanopowder (METCO). [Source: Ahmad and Ahsan [8]].

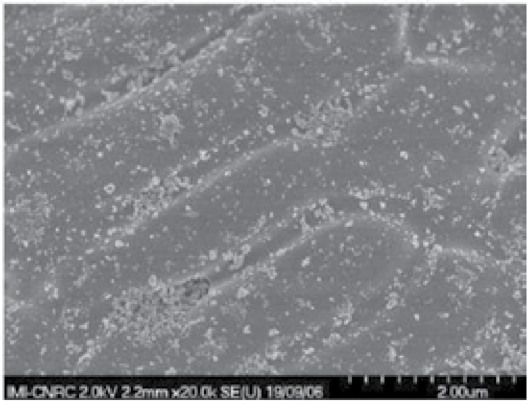

Figure 4. SEM image of spray-dried and densified nanopowder supplied by Sulzer Metco. [Source: Ahmad and Ahsan [8]].

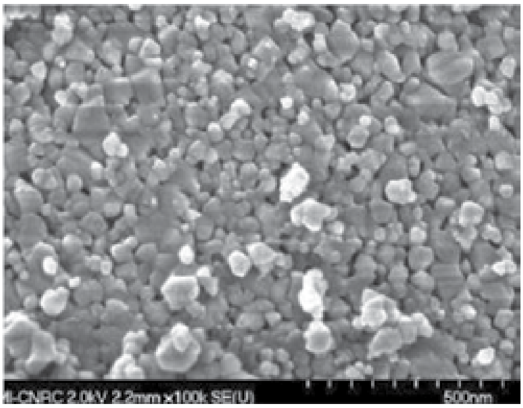

Figure 5. SEM image of nanopowder, spray dried and sintered supplied by Sulzer METCO. [Source: Ahmad and Ahsan [8]].

The interfacial thickness of the "conventional" and the "nano" Al_2O_3-13 wt% TiO_2 plasma coating in steel substrate has a significant effect on the bond distance. The Rockwell hardness of conventional and nanostructured coating was found to be 22 and 45 J/m^2 respectively. The micro structure of the conventional coating consisted of fully molten and solidified splats. The nano coating showed regions of fully molten (FM) splats, interspersed with partially molten rounded feature. One important observation was weak adhesion of partially melted/steel interface which cracked, whereas fully molten interface of splats showed no cracking and complete adhesion to the substrate. In a work by Shaw et al., it was found that the coatings produced from nano feedstock showed better resistance than the coating produced from commercial coarse grade powders [9]. Similarly, it was found that the zirconia nanostructured coatings showed better performance than their conventional counterpart. Their superiority was attributed to optimized microstructure and improved microhardness. Detailed studies were performed on microstructural properties, abrasive and sliding wear. Atmospheric plasma spraying and vacuum plasma spraying on Al_2O_3, 13 TiO_2, Cr_2O_3-5-SiO_2-3 TiO_2, and TiO_2 coatings [10].

The VPS-coated surface showed improved properties because the coatings retained a typical structure which was composed of both fully melted and partially melted particles.

In general, the physical and mechanical properties of nanostructured coatings showed improved mechanical properties, low density, improved hardness, ideal adhesion strength, strong resistance to crack growth, and strong resistance to spalling. The above-mentioned properties suggest a beneficial effect of using nanopowder for fabrication of plasma-sprayed nanostructural surface. Despite the progress made, studies on corrosion are seriously lacking in this area.

Harsh environments are encountered in service such as pulp and paper industry and similar other industries. Resistance to erosion-corrosion is crucial to the integrity of the coating. Unfortunately, information on the mechanism of erosion-corrosion and localized corrosion is very scarce. An attempt has been made for reporting corrosion behavior of nano titanium dioxide plasma-sprayed coatings in this article.

2.2. Process

A patented plasma spray coating procedure invented by Sulzer Metco was used to coat the sample. The nanopowder was fed by argon, hydrogen and helium. The slurry composed of binder, nanopowder, and solvent was fed at a rate of 25 l/min by a peristaltic pump. A 9 MB plasma gun was used in the procedure. Argon gas carried the powder at a feed rate of 14 g/L in the plasma jet generated from argon at ~40 spm and 2–3 rpm. A constant current was maintained at 400 A. The process is shown in **Figure 6**.

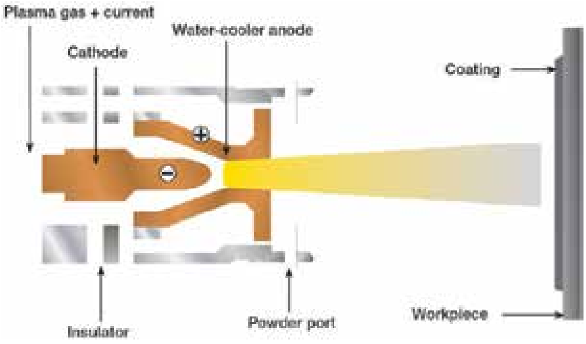

Figure 6. Illustrative diagram of plasma spray process. [Source: An Introduction to Thermal Spray, Issue 4 © 2013 Sulzer Metco].

In the high-velocity oxy-fuel process, **Figure 7**, Sulzer Metco CDS100 gun was utilized. The flame was produced by combustion of oxygen and methane. The flame temperature was lowered by nitrogen. The feed rate was 20 g/L at a flow rate of 12 spm. The spray distance was maintained at 100 mm.

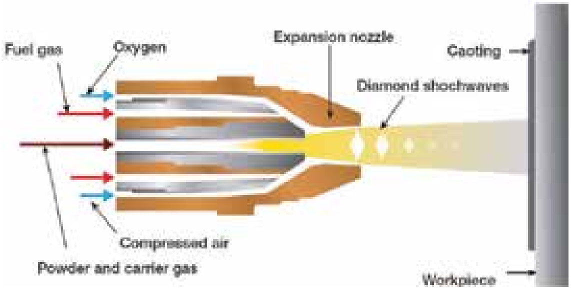

Figure 7. High-velocity oxy-fuel spray process diagram. [Source: An Introduction to Thermal Spray, Issue 4 © 2013 Sulzer Metco, with kind permission of Sulzer Metco].

2.3. Specimen preparation

The sample thickness was 0.033 mm and it was coated only on one side. A commercial bond coat was applied on both sides of the sample to protect their surface. The sides were sealed by paint. The sample was exposed to a wet grinding machine with 320 and 600 grit SiC paper. Water was used as a lubricant. The size of the samples was 70 × 100 mm, 58 × 100 mm, 48 × 100 mm, and 40 × 100 mm in dimension for fitting in holder of the loop. A schematic diagram of the loop is shown in **Figure 8**.

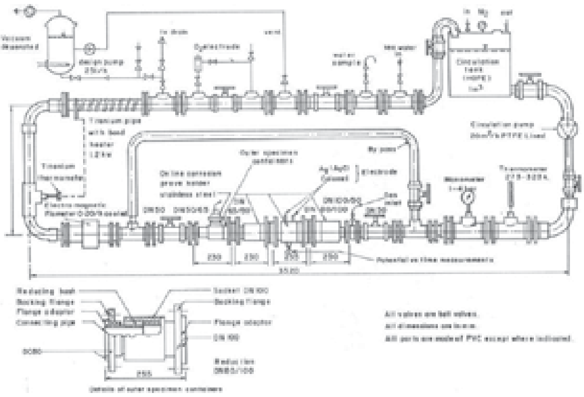

Figure 8. A custom-designed PVC loop for erosion-corrosion study. [Source: Ahmad and Aleem [11]].

2.4. Microanalytical studies

The surface morphology of the sample was examined by a low vacuum scanning electron microscope. An energy-dispersive oxford system was used for elemental analysis. Nano-R2 atomic force microscope was used for the study of surface morphology in contact and vibrational mode.

2.5. Recirculation loop

Erosion-corrosion studies were conducted by a high-density custom-designed PVC loop. The main parts of the loop consisted of entry and exit control valve, manometer, water pump, flow meters, and sample holders of different sizes. The loop comprised two columns, each column capable of holding six specimen holders and each specimen holder had a capacity to accommodate six specimens. The samples fixed on the holders were exposed to velocity ranging from 1.0 m/s to 4 m/s. The temperature in the loop was 45±2°C. The loop was run for 150 h at one time.

2.6. Immersion tests

Laboratory immersion was conducted according to ASTMG31 [12]. Before exposing the samples to 3.5 wt% NaCl, they were cleaned with acetone and rinsed with distilled water. The samples after exposure were dried and put in a desiccator. The rate of corrosion was determined by the loss in the weight of the samples after immersion.

2.7. Electrochemical studies

Electrochemical polarization resistance [13] measurements were made in accordance with recommendations of ASTM G59 after immersing them for 2 hours to obtain equilibrium and applying a controlled potential scan over a range of ± 25 mV with respect to corrosion potential (Ecorr). Software supplied by Gamry was used and the data were recorded. On processing, the following corrosion rates were achieved (**Figure 9**).

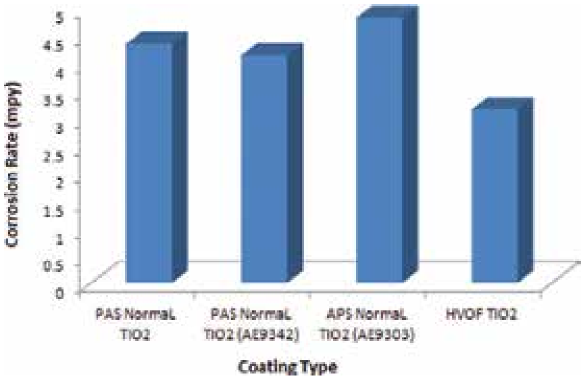

Figure 9. Corrosion rates of nanostructured and conventional titanium oxide coatings by salt spray chamber test. [Source: Ahmad and Ahsan [8]].

The polarization resistance diagrams are shown in **Figures 10–12**. It is clearly observed that the least rate of corrosion is exhibited by HVOF-coated sample followed by the AE9342 (nanostructured TiO_2 coated), the polarization resistance of the two samples being 1.404 ohms and 1.147 ohms, respectively. This is consistent with the morphology of the splats which shows a large region of fully melted particles homogeneously distributed compared to others with voids, agglomerates, large number of splat boundaries which creates conditions for the onset of corrosion. The morphology would be discussed more under the section of erosion-corrosion.

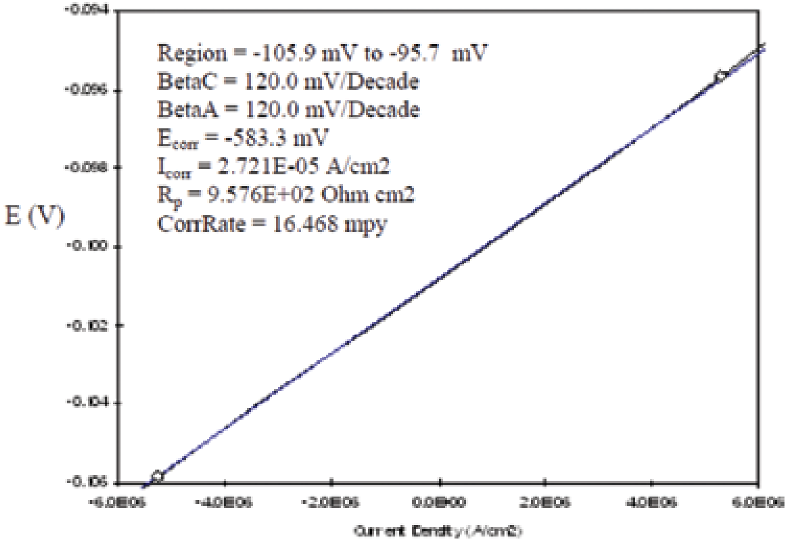

Figure 10. A polarization resistance plot of TiO2-coated specimen in 3.5% NaCl. [Source: Ahmad and Ahsan [8]].

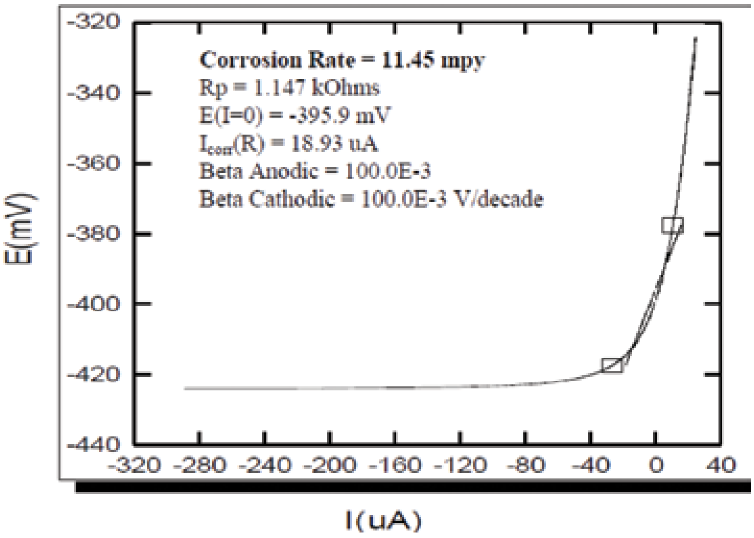

Figure 11. Polarization resistance curve for nano TiO2-coated specimen (AE9342). [Source: Ahmad and Ahsan [8]].

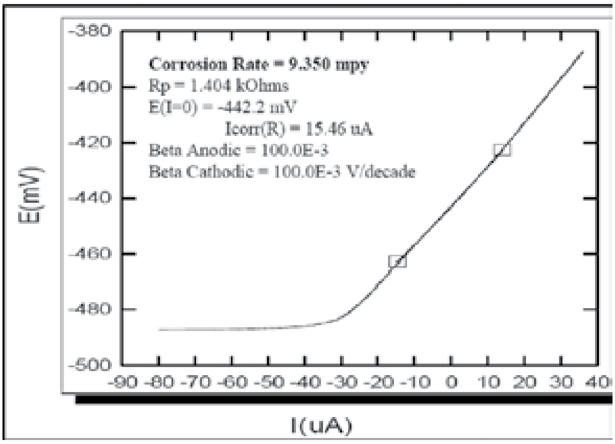

Figure 12. A polarization resistance plot of TiO_2-coated specimen by HVOF. [Source: Ahmad and Ahsan [8]].

2.8. Salt spray studies

Salt spray tests were conducted as per ASTM B117 [14]. The corrosion rate of samples exposed to salt spray for 1000 hours is shown in **Figure 13**. There is no significant difference in the rate of corrosion as the TiO_2-coated specimens are in general highly resistant to humid conditions and salt water. However, the nanostructured coating exhibits slight superiority to the normal TiO_2 (4.143739 and 4.846697 mpy) vs. 4.3519 mpy, respectively. A slightly higher resistance is shown by the HVOF-coated sample (3.157205 mpy). The difference can be attributed to morphological variations which affect the integrity of coating.

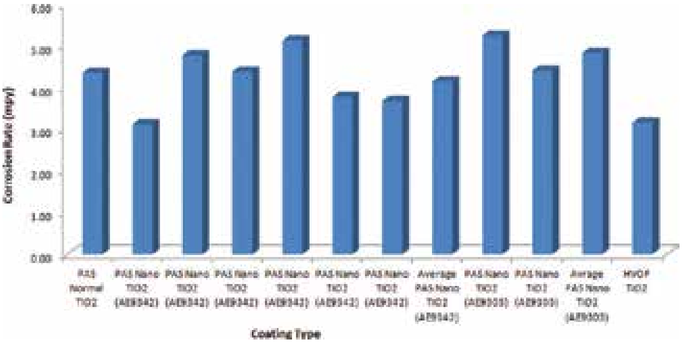

Figure 13. Corrosion rates of nanostructured and conventional titanium oxide coatings by salt spray chamber test. [Source: Ahmad and Ahsan [15]].

2.9. The erosion-corrosion studies

The erosion-corrosion resistance of the coated samples was determined in a high-density PVC recirculating loop described in the experimental section. At lower velocities (1 m/s), only a slight damage was observed on the TiO_2-coated specimens. Localized corrosion such as galvanic and crevice attack was observed. Surface etching by impact of polystyrene NaCl slurry occurs preferentially in the splat boundaries. Narrow splat boundaries permit the penetration of eroded particles in solution, whereas wider boundaries in conventional coatings are more sensitive to erosion and water penetration. The surface morphology of the coating and homogeneous distribution of fully melted particles controls the degree of penetration. If water reaches the inter-splat boundaries, it reacts with the steel substrate and dislodges the iron particles with the subsequent formation of a fibrous network mainly composed of small particles of iron due to the interaction with slurry. Some oxide inclusions formed by reduction of traces of oxides for example Cr_2O_3 may participate with the formation of network.

In the conventional titanium dioxide coating, preferred dissolution of inter-splat boundaries is observed. The figure shows mixed splat geometry of specimen AE9342. A mixed geometry showing nano agglomerates, splats, and fully melted particles is shown in **Figure 14**. The morphological defects are shown in the figure with experimental analysis.

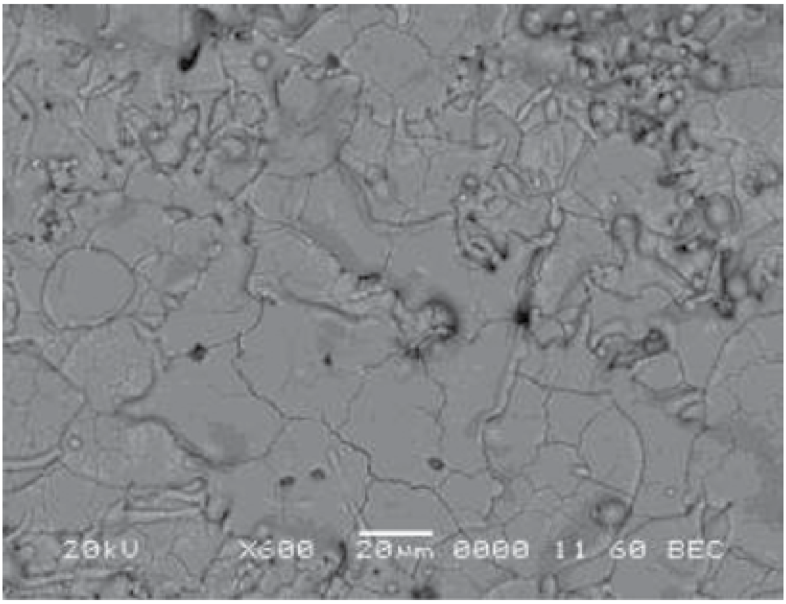

Figure 14. A homogenous surface morphology of AE9342 n-TiO2-coated specimen shows the densification of pancake-shaped splats. [Source: Ahmad and Ahsan [8]].

2.10. The fibrous network

The fibrous network may be attributed to the transpassiveness of the Fe particle from the substrate due to attack by slurry composed of polystyrene particles in 3.5 wt% NaCl solution. From experimental studies, it appears that dissolution by erosion-corrosion occurs mainly by the penetrating water in splat boundaries as shown in **Figure 15**.

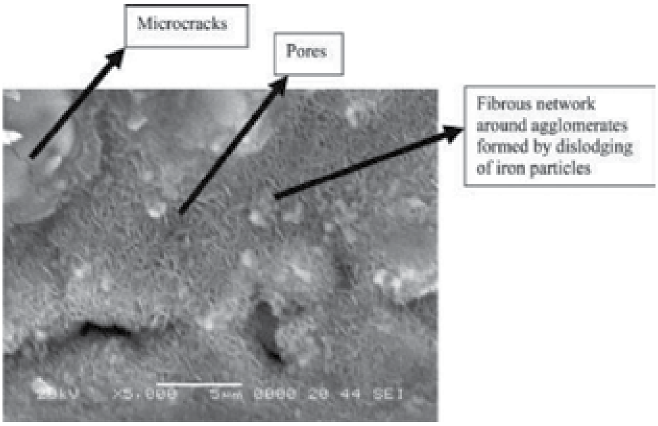

Figure 15. SEM image showing formation of fibrous network by dislodging of particles. [Source: Ahmad and Aleem [11]].

On comparing specimens AE9303 and AE9342, it is observed that the surface morphology of AE9303 is relatively nonuniform and has less number of splats. It also shows a smaller number of splat zones of fully melted particles. The above factors clearly show that the surface morphology controls the dissolution by erosion-corrosion. Specimen AE9303 offers a higher resistance.

The higher resistance of AE9342 nanostructured TiO2 PAS coated is further confirmed by the observation that the surface morphology of AE9342 reveals no corrosion attack on the splat grain boundaries, microgrooves, and spherical agglomerates. The dense, thick, and uniform morphology of AE9342 is shown in **Figure 16**.

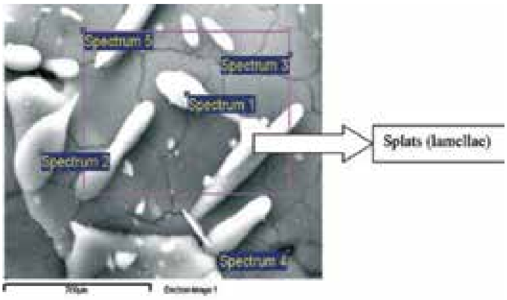

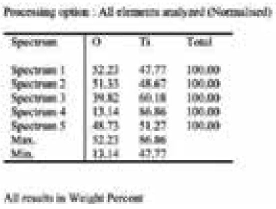
Processing option : All elements analyzed (Normalised)

Spectrum	O	Ti	Total
Spectrum 1	52.23	47.77	100.00
Spectrum 2	51.33	48.67	100.00
Spectrum 3	39.82	60.18	100.00
Spectrum 4	13.14	86.86	100.00
Spectrum 5	48.73	51.27	100.00
Max.	52.23	86.86	
Min.	13.14	47.77	

All results in Weight Percent

Figure 16. SEM image of specimen 9342 showing morphology of splats (lamellae). [Source: Ahmad and Aleem [11]].

2.11. Morphological studies

The microstructural features of nano-spray dried powders AE9340 and AE9342 (nano-spray dried and densified) followed by sintering were studied under low vacuum scanning electron microscope. The agglomerates formed from individual nanopowders are shown in **Figures 1–3**. Both powders exhibit granule shape which is mostly circular and devoid of small agglomerates glued to larger particle. The coating comprises mostly of melted nanoparticles which upon impingement on the substrate form splats. The partially melted particles can also be observed in the figure. A typical thermal monolithic coating would consist of non-homogeneous features including fine grain, splat boundaries, pores, inclusions, fully and partially melted and unmelted particles.

The morphology of coated specimens is shown in **Figures 17–21**. Specimen ME102 (control sample) exhibits unsymmetrical morphology pores, particles, nano unmelted particles, agglomerates of nano particles, and a zone of fully melted particles. For a plasma-sprayed coating to be ideal, it must show a large zone of fully melted particles. Specimen 9342 shows a zone of uniform distribution of fully melted particles compared to M102 which reveals the improved performance of TiO2 coating from nanopowder feedstock. In contrast, specimen AE9303 shows mixed splat geometry as a nonuniform distribution of splats (**Figures 22** and **23**). In HVOF-coated n-TiO2 specimens, a larger zone was observed to be covered with agglomerates of fully melted splat particles compared to plasma air-sprayed coating which offers it a slight superiority (**Figure 24**).

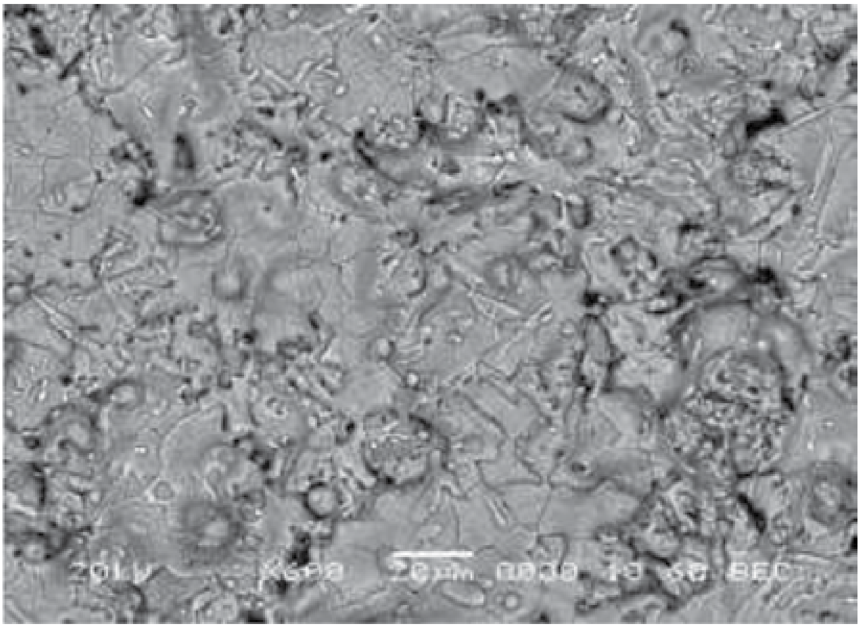

Figure 17. SEM image showing the state of splats as a dense structure in M102 (conventional TiO_2). [Source: Ahmad and Ahsan [8]].

http://dx.doi.org/10.5772/64316

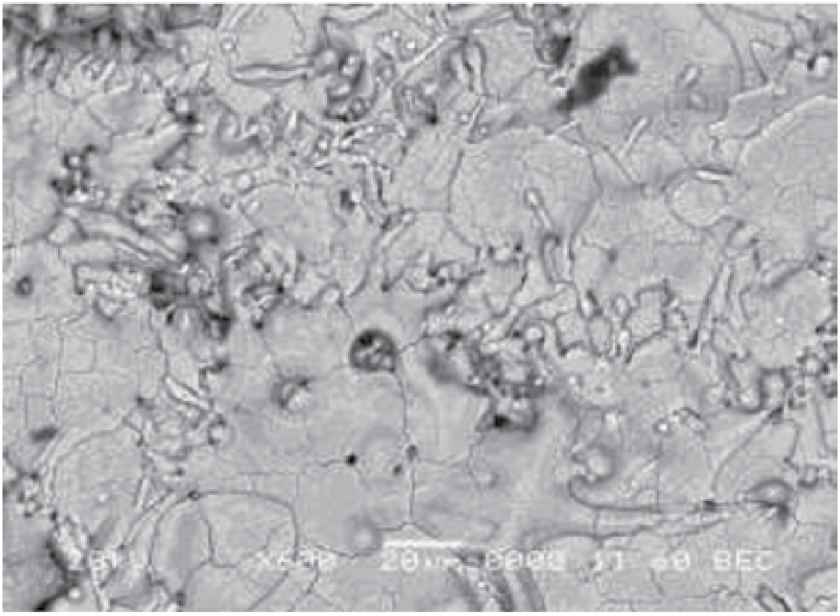

Figure 18. SEM image showing spherical pancake-shaped splats and pores in n-TiO_2 coating as observed in specimen in AE9342. [Source: Ahmad and Ahsan [8]].

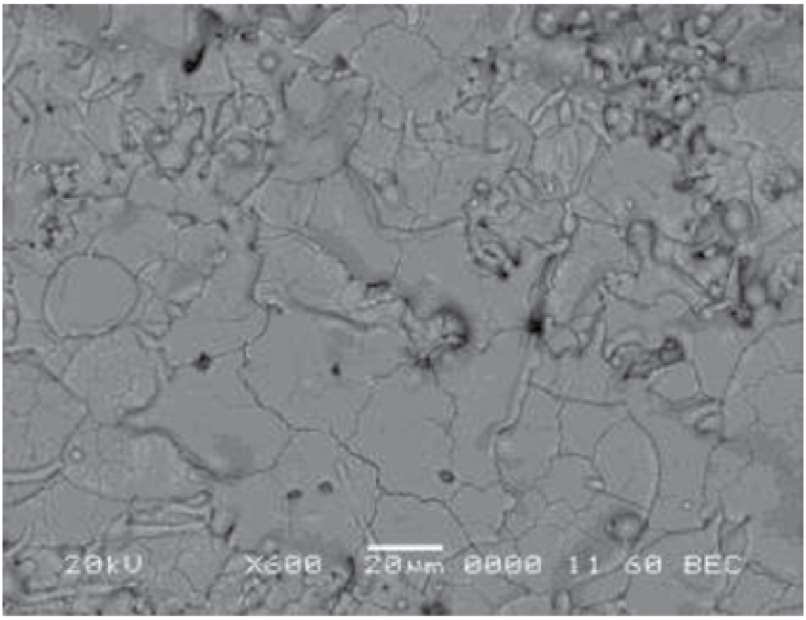

Figure 19. SEM image of n-TiO_2 coating on specimen AE9342 showing a high density of splats. [Source: Ahmad and Ahsan [8]].

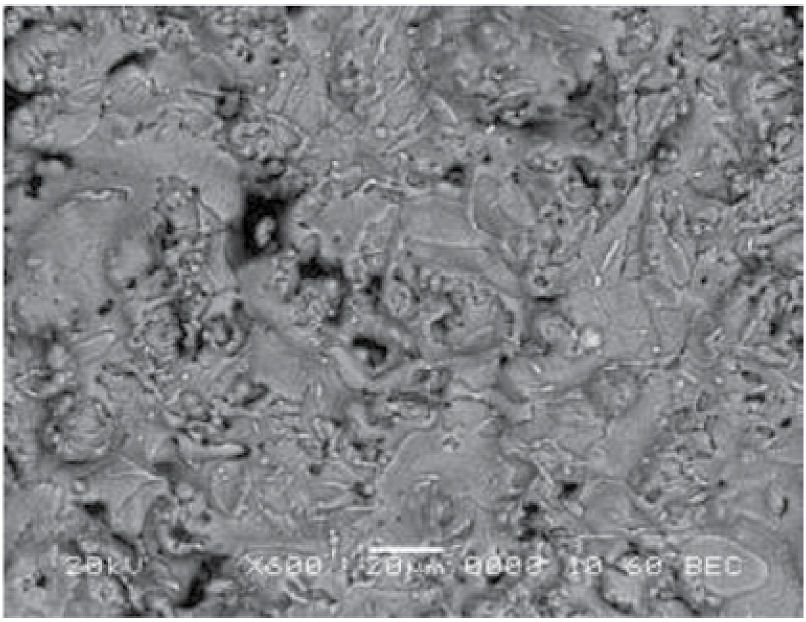

Figure 20. SEM image showing unmelted particles and pores on the surface of nano-TiO_2-coated specimen AE9342. [Source: Ahmad and Ahsan [8]].

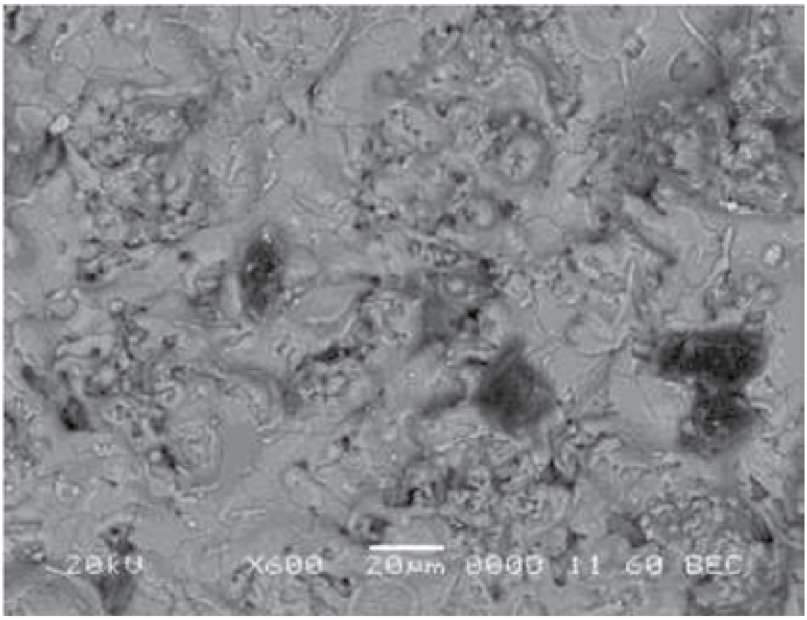

Figure 21. SEM image showing agglomeration of nanoparticles and zones of fully melted particles in AE9342. [Source: Ahmad and Ahsan [8]].

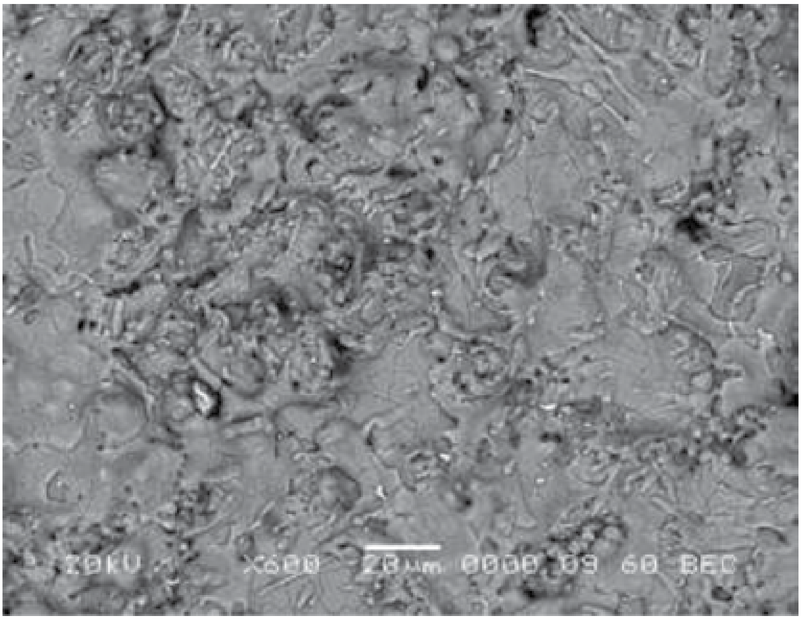

Figure 22. SEM image showing a nonuniform distribution of splats on sample AE9303. [Source: Ahmad and Ahsan [8]].

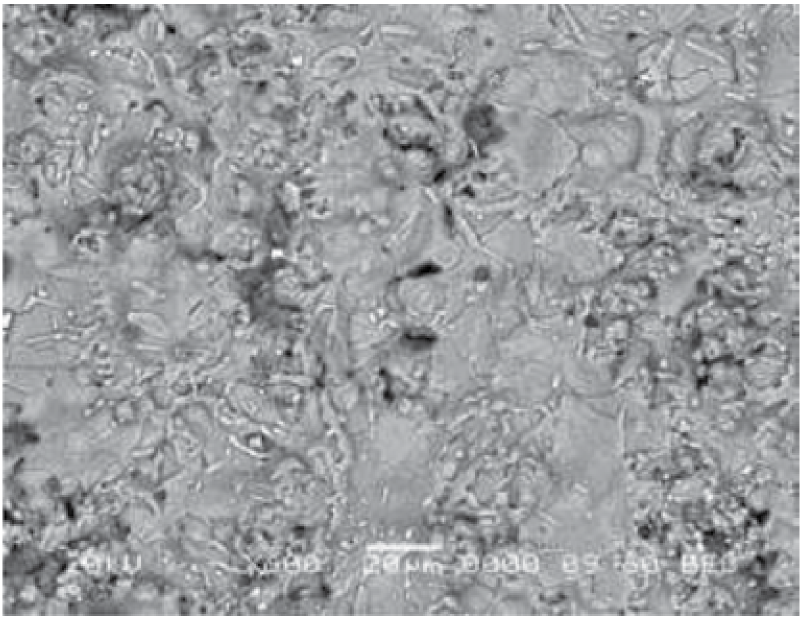

Figure 23. SEM image showing different shapes of splats, voids, and nonuniform surface on specimen AE9303. [Source: Ahmad and Ahsan [8]].

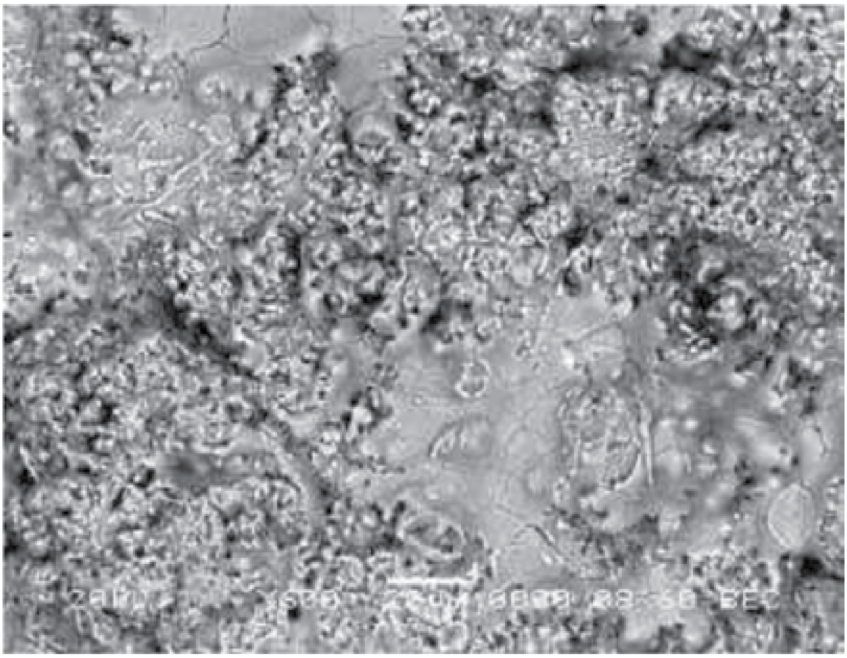

Figure 24. SEM image of HVOF-coated n-TiO_2, showing a large melted zone, uniform distribution of agglomerates, and a high density of melted particles. [Source: Ahmad and Ahsan [8]].

Different geometries of molten splats are shown in **Figure 25**. The AFM images of plasma air-sprayed coatings are shown in **Figures 26–32**. A layered structure with periodicity can be observed from smaller M102 (control sample). The horizontal shaped large voids and packing of splats can be observed in **Figures 29** and **30**. Specimen AE9342 exhibits grain boundaries, columnar grains, and a large zone of fully melted splats (**Figure 31**) and withstands erosion and corrosion. Morphological studies reveal that n-TiO_2-coated specimen possesses morphology critical to the beneficial properties of PAS TiO_2-coated substrate in steel. The magnitude of erosion-corrosion is higher in n-TiO_2 and AE9303 caused by dislodging of iron particles and an uneven nonhomogeneous-coated surface covered with a fibrous network of fragmented oxides. The dislodging of iron particles appears mainly to be responsible for the sensitivity of the substrate due to water penetration through the narrow splat boundaries to erosion-corrosion. The variation of corrosion rates with the velocity of the sample is shown in **Figure 33**. The increased corrosion rate has been attributed to the destruction of the passive layer unlike on the steel surface. The surface roughness of n-TiO_2 does not impede the development on the steel surface like in MMC (Metal Matrix Composite) where protrusion and particulate size increase the surface roughness with the range (20–30 μ) which allows ingress of slurry. This phenomenon is not conclusively understood. The impact of polystyrene NaCl slurry may cause a significant damage to MMCs because of protrusion of particles. It has been observed in the investigation that micro hardness of AE9342 has a greater homogeneity than AE9303 in the range of 36–58 nm which does not allow the ingress of slurry particles [11].

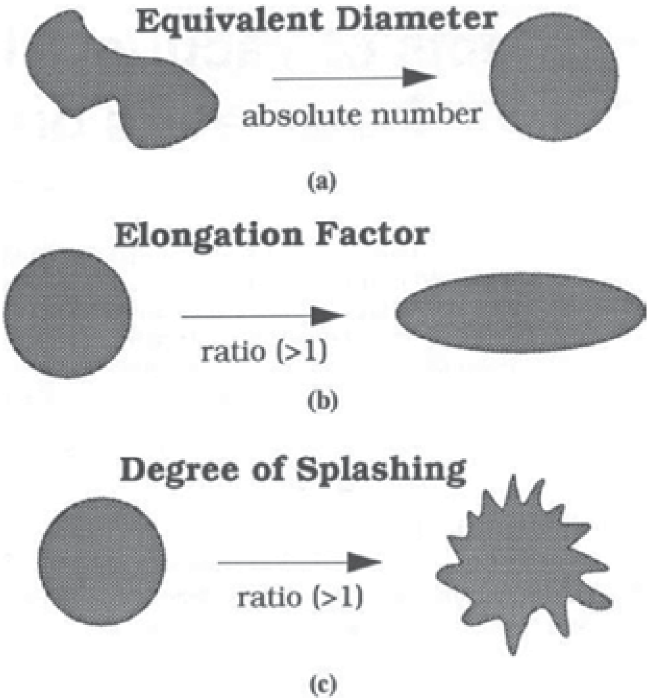

Figure 25. Figure showing the effect of absolute number, elongation, and degree of splashing on the shapes of splats. [Source: Montavon et al. [16]].

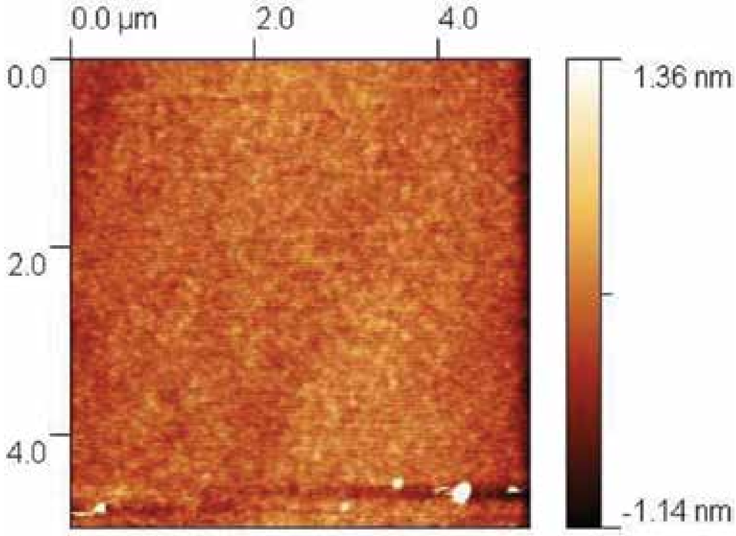

Figure 26. A layered structure imaging is observed in the AFM image of specimen M102. [Source: Ahmad and Ahsan [8]].

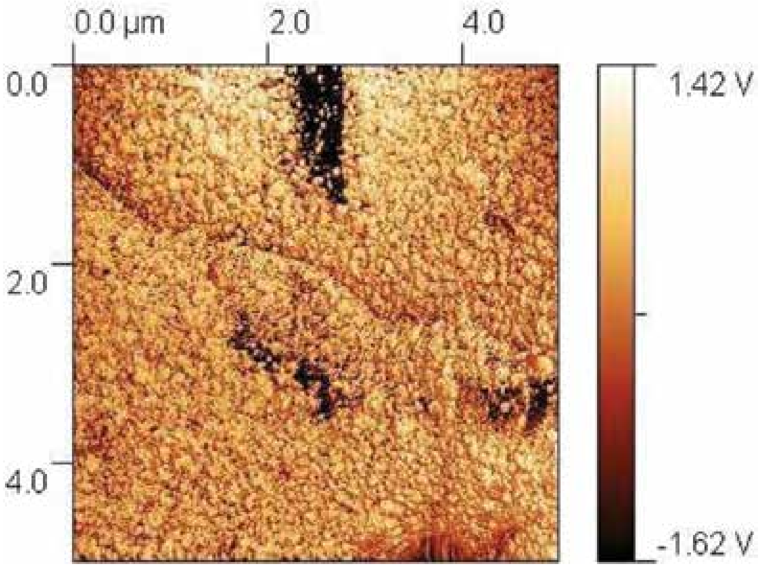

Figure 27. A dense and spherical topography is observed in the surface of specimen M102 in the vibration mode. [Source: Ahmad and Ahsan [8]].

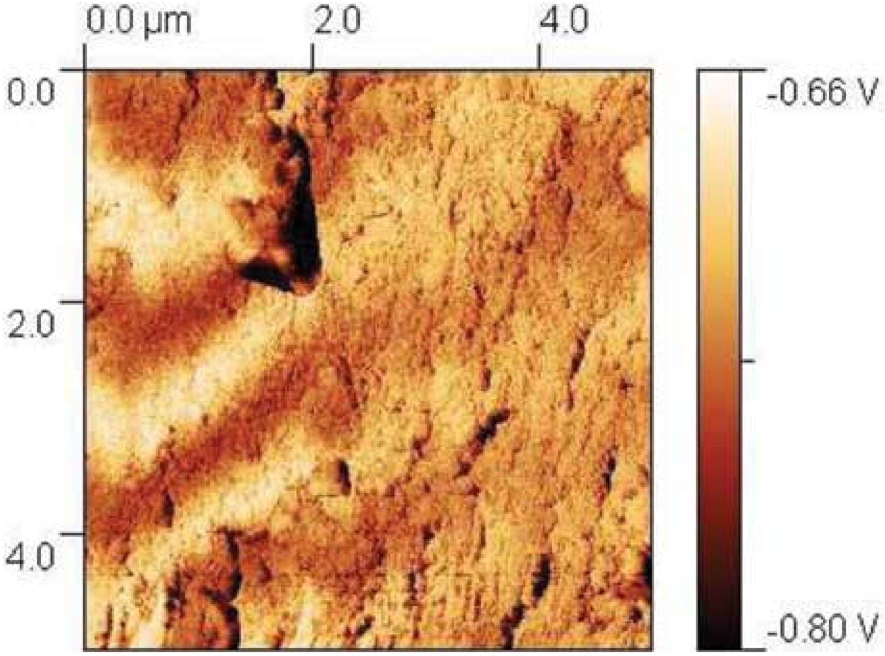

Figure 28. AFM topography of ME102 showing the repetition of fully melted and partially melted zones. [Source: Ahmad and Ahsan [8]].

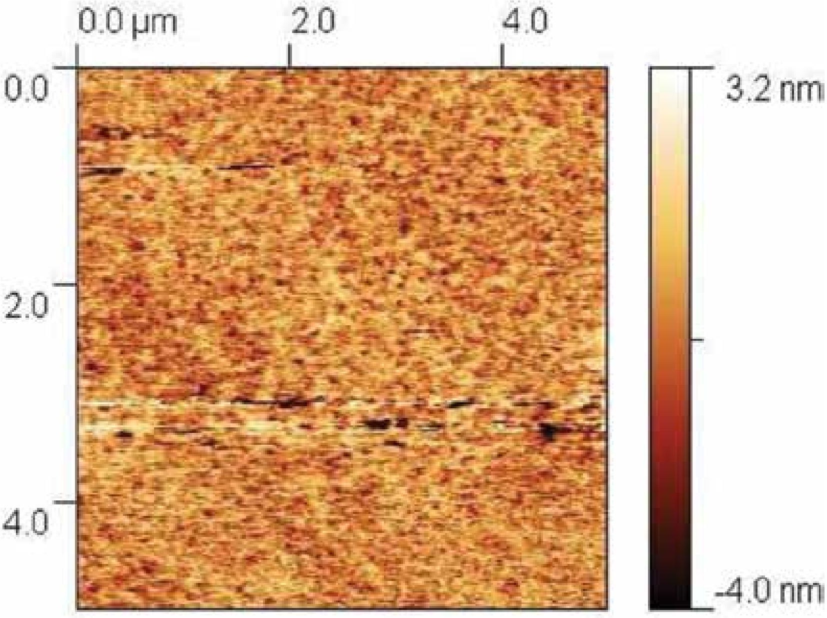

Figure 29. An AFM image showing morphology of specimen AE9303 in contact mode. [Source: Ahmad and Ahsan [8]].

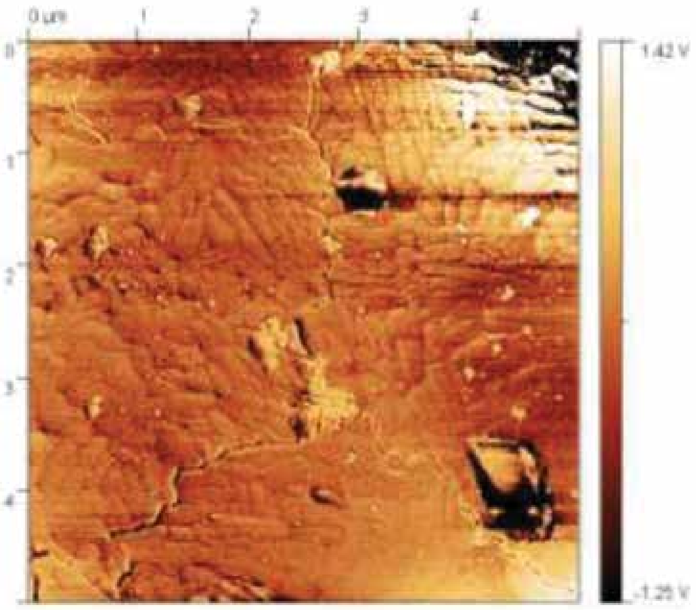

Figure 30. AFM image of AE9303 showing large voids and inter-splat zones in vibrating mode. [Source: Ahmad and Ahsan [8]].

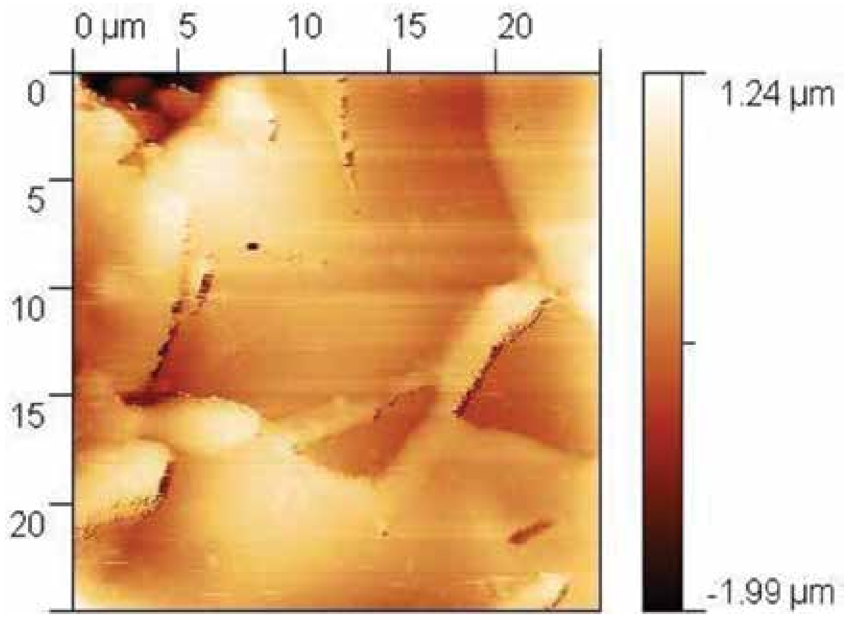

Figure 31. The grain boundaries of specimen AE9342 are clearly shown by AFM in contact mode. [Source: Ahmad and Ahsan [8]].

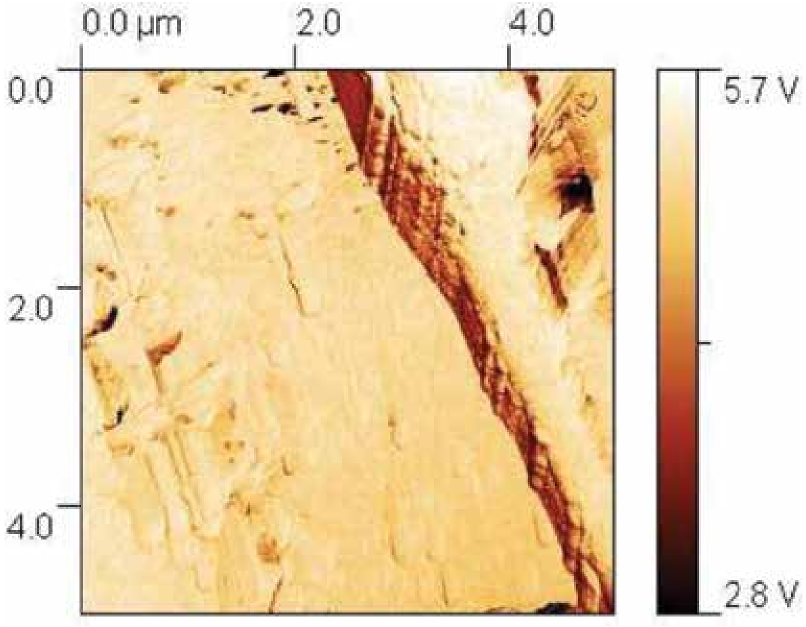

Figure 32. An AFM image of AE9342 in vibrating mode clearly showing distinct columnar grains. [Source: Ahmad and Ahsan [8]].

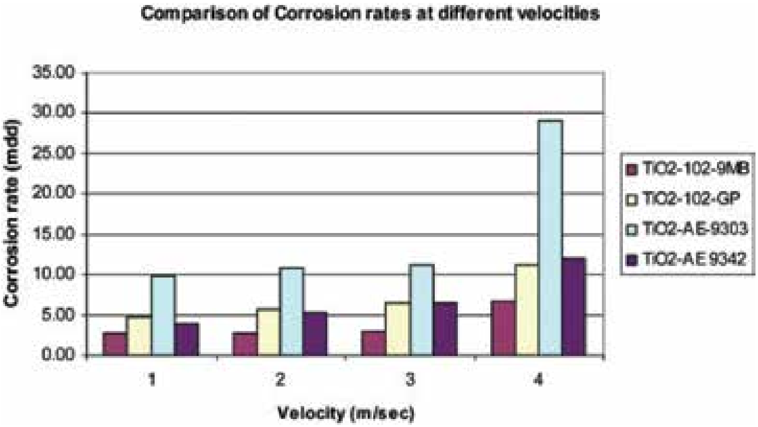

Figure 33. The effect of velocity on the corrosion rate of different alloys used in experiments showing the superior resistance of AE9342. [Source: Ahmad and Aleem [11]].

Erosion-corrosion of n-TiO_2-coated stainless steel by PAS is only confined to areas of heterogeneity. In conventional ceramic coatings, hardness of the coating has an inverse relationship with metal wastage, and resistance to erosion-corrosion is correlated with the composition and microstructure of coatings [17].

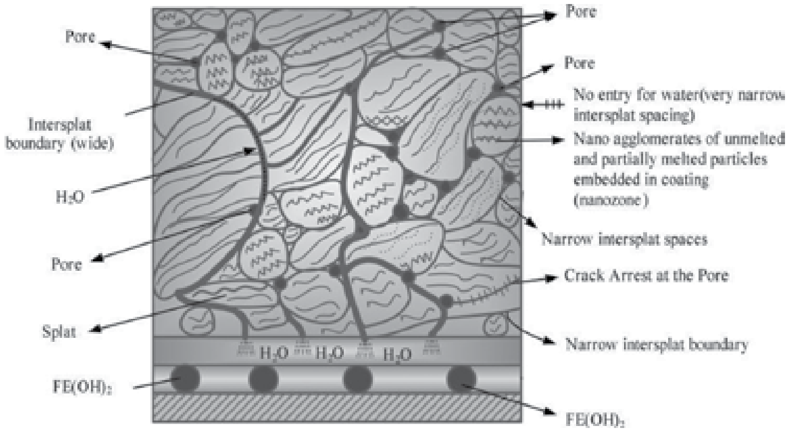

Figure 34. A schematic illustrating the mechanism of erosion-corrosion of plasma spray coated surface on nano-TiO_2. [Source: Ahmad and Aleem [11]].

In the studies conducted, the porosity of AE9342 was less than SM102, and also the bond strength of AE9342 was higher than the bond strength of SM102. Nanoparticles played a crucial role in controlling the corrosion mechanism. It has been shown by previous work on conducting surfaces (70Cu-30Ni) that nano zones are embedded in the homogeneous zones of nano melted particles in preventing the ingress of slurry and erosion-corrosion mechanism, both of which are responsible for increasing the resistance to erosion-corrosion. Microstructure holds the key which depends on the reconstitution of powders and key APS parameters used in depositing the nanocoatings. The proposed mechanism of erosion-corrosion is shown in **Figure 34**.

The figure shows splats, inter-splat boundaries, pores, nano-agglomerates, and other features. It may be observed that the water passes through the inter-splat boundaries from various directions. The wide splat boundaries allow the ingress of water to the substrate resulting mainly in the formation of $Fe(OH)_2$, largely responsible for erosion-corrosion and builds up a fibrous network which allows dissolution by liquid metal ingress. The pores are wide to assist propagation of cracks. It is known that ductile materials have lesser erosion loss and offer an impingement angle relative to substrate, whereas the opposite is true of hard surface-coated samples. Stainless steel falls in this category. The coating of n-TiO2 is harder than the conventional TiO2-coated substrate. The nanostructure coatings have shown very lesser impingement angle compared to conventional coatings. This is exemplified by ball-valve application in harsh environment [18]. Very low pressure plasma spray offers advantages over the conventional air plasma spray because a fully developed nanostructured coating can be deposited which offers superior properties. However, the work conducted so far is not conclusive [19]. The corrosion resistance of nanostructured coating is clearly related to their morphology and adhesion of the nano-coating to the substrate. The mechanism suggested above is supported by SEM and AFM observations.

3. Conclusion

The resistance of nanostructured TiO_2 coating to erosion is controlled by the homogeneity and large fully melted zones of splats, homogeneous zone of nano-agglomerate particles, narrow interfacial boundaries, absence of fibrous network of dislodged particle of substrate, spherical splats, morphology, homogeneous distribution of splats, dense splats zone, embedding of nano zones in the coating with small variations in the surface roughness, which present the onset of localized corrosion and the deleterious effects caused by erosion-corrosion. It has been shown that plasma-sprayed nanostructured TiO_2 coatings offer a higher resistance to erosion-corrosion in 3.5 wt% NaCl aerated condition. The APS (Air Plasma Spray) coatings also offer high resistance to corrosion in salt spray chambers. Electrochemical polarization data obtained is in full agreement with the immersion study. Electrochemical corrosion studies also show a high resistance of nano-TiO_2 PAS coatings compared to conventional TiO2 APS coatings. The nano-TiO2 coatings deposited by HVOF (High Velocity Oxyfuel) offer relatively higher resistance to corrosion compared to APS n-TiO_2 coatings. The processing techniques influence the microstructure and consequently increase the corrosion resistance. The success of nanostructured coating market can be judged from the projected growth of market to $9.7 billion per annum by 2025. This dramatic upward trend calls for greater cumulative efforts of global researchers to fulfill the demand and make the coatings cost-effective. Our finding clearly reveals the advantages offered by n-TiO2 air plasma coatings in harsh environment. A new mechanism of erosion-corrosion of n-TiO2-coated substrates has been suggested; however, a conclusive mechanism is yet to be worked out.

Author details

Zaki Ahmad*, Asad Ullah Khan, Robina Farooq, Tahir Saif and Naila Riaz Mastoi

*Address all correspondence to: drzakiahmad@ciitlahore.edu.pk

COMSATS Institute of Information Technology, Lahore, Pakistan

References

[1] E. Turunen, T. Varis, T.E. Gustafsson, J. Keskinen, T. Falt, S.-P. Hannula, "Parameter optimization of HVOF sprayed nanostructured alumina and alumina-nickel composite coatings", Surface Coatings and Technology, Vol. 200(16–17), 2006, 4987–4994.

[2] L. Leblanc, "Abrasion and sliding wear of nanostructured ceramic coatings", Thermal Spray 2003: Advancing the Science & Applying the Technology, C. Moreau and B. Marple (Eds.), ASM International, Materials Park, Ohio, USA, 2003, 291–299.

[3] R. Unger, "Comparison of thermal spray bond coats", Proceedings of the National Thermal Conference, ASM International, Materials Park, OH, USA, 1987, 365–376.

[4] D. Mardare, P. Hones, Optical dispersion analysis of TiO2 thin films based on variable angle spectroscopic elipsometry measurements. Materials Science and Engineering: B, Vol. 68, 1999, 42.

[5] A.R. Bally, E.N. Korobeinkova, P.E. Schmid, F. Levy, F. Bussy, Structural and Electrical properties of Fe- Doped TiO2 thin films. Journal of Applied Physics, Vol. 31, 1989, 1149.

[6] P. Bansal, N.P. Padture, A. Vasiliev, "Improved interfacial mechanical properties of Al_2O_3-13 wt% TiO_2 plasma-sprayed coatings derived from nano crystalline powders", Acta Materialia, Vol. 51, 2003, 2959–2970.

[7] V. Chawla, B.S. Sidhu, D. Puri, S. Prakash, "Performance of plasma sprayed nanostructured and conventional coatings", Journal of the Australian Ceramic Society, Vol. 44(2), 2008, 56–62.

[8] Z. Ahmad, M. Ahsan, "Corrosion studies on the plasma sprayed nanostructured titanium dioxide coating". Anti-Corrosion Methods and Materials, Vol. 56(4), 2009, 187–195.

[9] L.L. Shaw, D. Goberman, R. Ren, M. Gell, S. Jiang, Y. Wang, T.D. Xiao, P.R. Strutt, "The dependency of microstructure and properties of nano structured coatings on plasma spray conditions", Surface Coatings & Technology, Vol. 130, 2000, 1–8.

[10] P. Ctibor, K. Neufuss, P. Chraska, "Microstructure and abrasion resistance of plasma sprayed titania coatings", Journal of Thermal Spray Technology, Vol. 15(4), 2006, 689–694.

[11] Z. Ahmad, A.B.J. Aleem, Resistance of nanostructured titanium dioxide coatings to erosion corrosion, Tribology – Materials, Surfaces & Interfaces, Vol. 3(1), 2009, 41–48.

[12] ASTM Designation: NACE TM0169/G31 - 12a, Standard Guide for Laboratory Immersion Corrosion Testing of Metals, © NACE International/ASTM International, West Conshohocken, PA, USA, 2015.

[13] ASTM Designation: G59 - 97 (Reapproved 2014), Standard Test Method for Conducting Potentiodynamic Polarization Resistance Measurements, © ASTM International, West Conshohocken, PA, USA, 2014.

[14] ASTM Designation: B117 – 11, Standard Practice for Operating Salt Spray (Fog) Apparatus, © ASTM International, West Conshohocken, PA, USA, 2011.

[15] Z. Ahmad, M. Ahsan, "Environmental response of plasma sprayed nanostructured coatings". Advanced Materials Research, Vol. 32, 2008, 65–70.

[16] G. Montavon, S. Sampath, C.C. Berndt, H. Herman, C. Coddet, "Effects of vacuum plasma spray processing parameters on splat morphology", Journal of Thermal Spray Technology, Vol. 4(1), 1995, 67–74.

[17] Z. Shui, B. Wang, A. Levy, Erosion of protective coatings. Surface and Coatings Technology, Vol. 43/44, 1999, 859–874.

[18] J. Willams, G.E. Kim, J. Walker, "Ball valves with nanostructured titanium oxide coatings for high-pressure acid-leach service: development to application", Proceeding of Pressure Hydrometallurgy, 2004. Vol. 16 (1), 34-39.

[19] Y. Gao, Y. Zhao, D. Yang, J. Gao, "A novel plasma-sprayed nanostructured coating with agglomerated-unsintered feedstock", Journal of Thermal Spray Technology, 2015, DOI: 10.1007/s11666-015-0340-1. Vol 25, Issue 1-2, pp. 291-300.

Edited by Zaki Ahmad

High temperature corrosion is an extremely important area of corrosion as it causes the failure of high temperature equipment in process industry and power generation. Every engineer is required to obtain a basic knowledge of high temperature corrosion to prevent the colossal damage caused by it. This book contains chapters ranging from basic to advance topics to create an understanding of high temperature of various metals and alloys. With the emerging technologies such as nanotechnology, their role in controlling high temperature corrosion needs to be comprehended and new techniques developed to control high temperature corrosion. It is hoped that this book would fulfill these objectives and aspirations of the readers.

Note from the publisher:
It is with great sadness and regret that we inform the contributing authors and future readers of this book that the Editor, Prof. Zaki Ahmad passed away shortly after finishing the book and before having a chance to see its publication. Prof. Ahmad was InTech’s long term collaborator and edited his first book with us in 2011 (‘‘Recent Trends in Processing and Degradation of Aluminium Alloys’’). The book ‘‘High Temperature Corrosion’’ was his fourth edited volume. The fruitful collaboration continued until his final days when he was acting as a co-editor on a book ‘‘Wastewater Treatment and Resource Recovery’’. We would like to acknowledge Dr. Zaki Ahmad’s contribution to open access scientific publishing, which he made during 6 years of dedicated work on edited volumes and express our gratitude for his pleasant cooperation with us.

ISBN 978-953-51-6673-3

Photo by alexsalcedo / iStock

IntechOpen